Physics – Uspekhi **61** (12) 1175 – 1212 (2018)

REVIEWS OF TOPICAL PROBLEMS PACS numbers: **75.80.+q**, **75.85.+t**

Straintronics: a new trend in micro- and nanoelectronics and materials science

A A Bukharaev, A K Zvezdin, A P Pyatakov, Y K Fetisov

DOI: https://doi.org/10.3367/UFNe.2018.01.038279

Contents

1. **Straintronics: basic concepts** **1175**
   1.1 Introduction; 1.2 Cross effects involving the elastic subsystem; 1.3 Strain engineering; 1.4 Composite materials of magnetic straintronics; 1.5 Operating principle of magnetic straintronic devices
2. **Physical effects in magnetic micro- and nanoparticles and structures induced by mechanical stresses** **1182**
   2.1 Magnetization switching in particles; 2.2 Changes to micromagnetic structure under the action of mechanical stresses; 2.3 Stress-evoked magnetic transformations; 2.4 Thermally induced magnetoelastic effect; 2.5 Field transformation in composite structures
3. **Composite materials and devices of magnetic straintronics** **1199**
   3.1 Composition of structures and their formation methods; 3.2 Memory and logical devices switched by an electric field; 3.3 Sensors, energy converters, and microengines; 3.4 Electric field-tunable devices processing radio signals; 3.5 The spin-offs of straintronics: gyrators, transtors, and neuromorphic elements
4. **Conclusion** **1209**

References **1209**

Abstract. The term 'straintronics' refers to a new research area in condensed matter physics, in which strain engineering methods and strain-induced physical effects in solids are used to develop next-generation devices for information, sensor, and energy-saving technologies. This paper reviews the basic ideas of straintronics, examines the underlying effects, highlights its advantages over conventional electronics, and identifies the problems it faces and fundamental constraints it is subject to. Special attention is given to the straintronics of magnetic and magnetoelectric materials as the most promising area for radically reducing computational energy consumption. Specific examples are presented of how the principles of straintronics are applied practically in information and energy-saving technologies, as well as in sensor and microwave engineering.

Keywords: strain engineering, magnetoelastic interaction, magnetoelectric composites, multiferroics

A A Bukharaev Zavoisky Kazan Physical-Technical Institute, Federal Research Center "Kazan Scientific Centre" of the Russian Academy of Sciences, ul. Sibirskii trakt 10/7, 420029 Kazan, Russian Federation
E-mal: a_bukharaev@kfti.knc.ru
A K Zvezdin Prokhorov General Physics Institute of the Russian Academy of Sciences, ul. Vavilova 38, 119991 Moscow, Russian Federation; Lebedev Physical Institute of the Russian Academy of Sciences, Leninskii prosp. 53, 119991 Moscow, Russian Federation; Moscow Institute of Physics and Technology (State University), Institutskii per. 9, 141701 Dolgoprudnyi, Moscow region, Russian Federation
E-mail: zvezdin@gmail.com
A P Pyatakov Lomonosov Moscow State University, Faculty of Physics, Leninskie gory 1, str. 2, 119991 Moscow, Russian Federation
E-mail: pyatakov@physics.msu.ru
Y K Fetisov MIREA — Russian Technological University, prosp. Vernadskogo 78, 119454 Moscow, Russian Federation
E-mail: fetisov@mirea.ru

Received 17 September 2017, revised 15 January 2018
Uspekhi Fizicheskikh Nauk **188** (12) 1288 – 1330 (2018)
DOI: https://doi.org/10.3367/UFNr.2018.01.038279
Translated by Yu V Morozov; edited by A Radzig

1. Straintronics: basic concepts

1.1 Introduction

The increasingly rapid development of information technologies that has recently given rise to Big Data and blockchain requires further enhancement in the power of computing systems. The expert estimates [1] suggest that half of the energy supposed to be consumed by mankind in 2030 will be spent on computation; with the current pace of progress in information technologies and unaltered characteristics of electronic devices, the annual consumption for this purpose will exceed in absolute terms 10 PW h. This situation motivates researchers and engineers to develop new energy-saving technologies for information processing, with straintronics being intended to become one of them.

Straintronics is a new field of condensed matter physics making use of physical effects in solids related to mechanical strains developing in micro- and nanolayers or heterostructures under the influence of external controling fields and resulting in changes of the band structure, electric, magnetic, optic, and other properties of materials that create prerequisites for the implementation of the new generation of information and sensor devices and technologies.

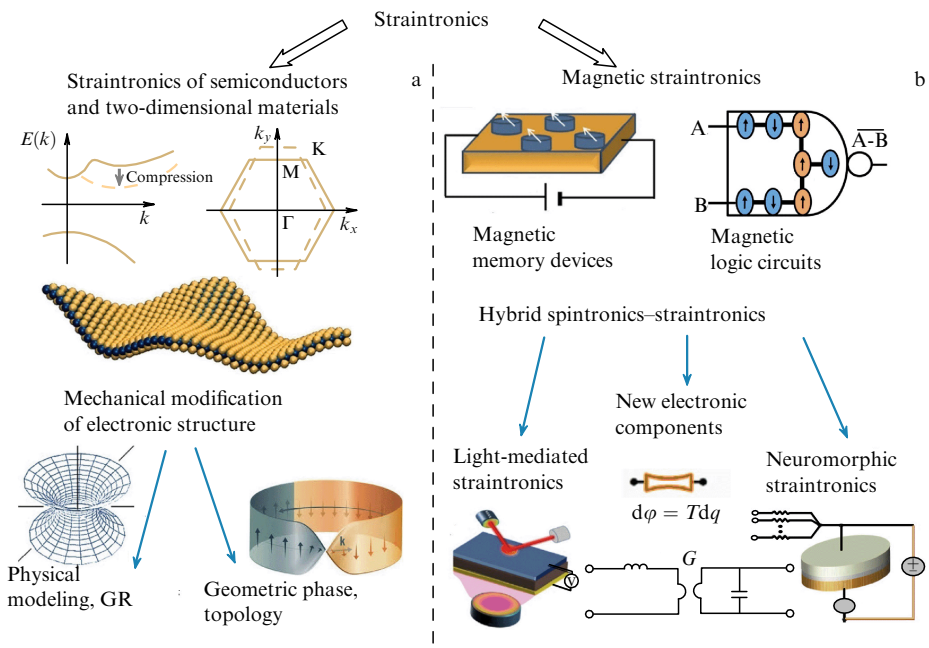

Figure 1. Two branches of straintronics. (a) Strain-mediated manipulation of the electronic structure. Mechanically induced transition from direct- to indirect-band structure in silicon nanotubes [6] and modification of the Brillouin zone in graphene [7]. (b) Main magnetic straintronic devices (magnetic memory and logic, in particular). $E(k)$ — dispersion dependence for electrons; T, G — characteristics of new electronic elements: transtor and gyrator (see Section 3 for details). Also shown are newly emerging kinds of straintronics: neuromorphic straintronics [8] and light-mediated straintronics) [9].

The history of the term straintronics provides an example of the powerful impetus given by the solution of basic physical problems to the development of numerous applied research areas. Suffice it to mention the article, "Electronic properties of corrugated graphene: the Heisenberg principle and wormhole geometry in the solid state," [2] containing a description of massless relativistic electrons in two-dimensional media taking account of the Heisenberg uncertainty principle and, at a higher level of abstraction, the integration of quantum mechanics and the General Relativity (GR). Such an approach based on the consideration of corrugated graphene sheets opened up new prospects for simulating the motion of relativistic particles in curved spacetime and the strain-mediated manipulation of electronic structures. The authors of Ref. [2] believed that devices of this sort would provide a circuitry of straintronics as a new branch of electronics.

At the same time, the linkage between mechanical stresses and magnetic or ferroelectric subsystems in crystals constitutes the central concept of the physics of multiferroics [3] and magnetoelectric composites [4]. First, changes in the crystal structure under the effect of mechanical strains can be regarded as an order parameter; second, strain itself serves as a factor that mediates the interaction between magnetic and electric phases. No wonder that the same term is simultaneously used [1] in an article devoted to problems at the interface between the physics of magnetoelectric composites and spin electronics ("Hybrid spintronics and straintronics: a magnetic technology for ultralow energy computing and signal processing") [5].

[1] Papers [2] and [5] were submitted to publication on January 12 and 11, 2011, respectively.

In this way, two branches of straintronics (Fig. 1) originated that have to date developed practically independently.

(1) The essence of one of them can be described as the influence of mechanical stresses on electronic properties. Its history dates back to the article by C S Smith [10] published in 1954 and devoted to piezoresistive properties of germanium and silicon, which were shown to undergo an abnormally large change in resistivity due to the modification of the semiconductor band structure in response to mechanical strain. Innovations in this branch are associated first and foremost with two-dimensional materials, such as graphene, hexagonal boron nitride, ZnO, ultrathin layers of transition metal chalcogenides: MoS_2 [11, 12], WSe_2, PdS_2 [11], WTe_2 [13] semiconductor monolayers, and planar heterostructures on them [14]. Mechanical stress in such structures serves as an 'elastic gauge field' interacting with fermions like an electromagnetic field [15], which begets a close analogy between quantum field theory and condensed matter physics.

(2) Developments in the other branch of straintronics proceed in the framework of magnetic electronics. Its main element is made up of the heterostructure of the magnetic layer with anisotropy produced by substrate deformation (upper part of Fig. 1b). It is supposed that magnetic straintronics permits full implementation of ultralow energy consumption inherent in the idea of controling the spin degree of freedom. According to the estimates made in Refs [5, 16], the switching energy of straintronic memory units will be below 1 aJ, i.e., not far from the limits of fundamental thermodynamic principles, such as the *Landauer limit* $k_B T \ln 2$ — the minimal energy dissipated during the erasure of a bit of information [16]. Similar ultrasmall energy losses are inherent in straintronic logic devices [17] and analog amplifiers [18]. To recall, the claimed parameters based on

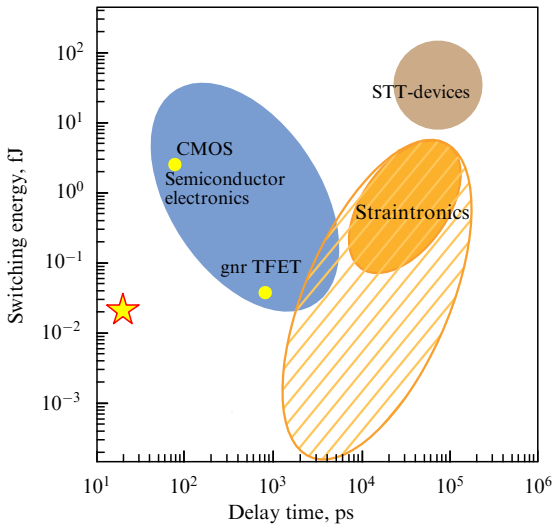

Figure 2. (Color online.) Schematic representation of characteristics of traditional semiconductor electronic, spintronic, and straintronic devices in the *dissipated energy — delay time* axes [5] (in certain reviews, e.g. [19, 20], straintronics is considered as the magnetoelectric variety of spintronics). Blue region corresponds to characteristics of semiconductor electronics: CMOS — silicon-based metal-oxide-semiconductor transistors, gnrTFET — graphene nanoribbon Tunneling Field Effect Transistors [19]. The region denoted 'STT-devices' covers characteristics of modern spintronic devices based on the spin-transfer torque (STT) effect [19]. Solid color areas correspond to characteristics of prototype straintronic devices [21–24], and the hatched region to theoretical estimates [5, 16–18]. The asterisk denotes characteristics of light-mediated spin dynamics induced by femtosecond laser pulses, which is currently the fastest magnetization switching process [25].

theoretical estimates (Fig. 2, hatched region) should be treated with caution. Consideration of additional losses[2] during the operation of straintronic device prototypes demonstrated in Refs [19, 21–24] shows that their real characteristics (the solid color region in Fig. 2) are far from limiting ones. Nevertheless, the straintronics of magnetic materials at large appears to be closer to practical realization than its 'graphene' branch and exceeds the latter 1.5–2-fold in terms of the number of publications. Moreover, an indisputable advantage is that the magnetic straintronic devices are nonvolatile, i.e., maintain the steady state in the absence of an energy supply. This allows the advantages of read-only and random-access memory elements to be combined in a single device.

The present review is focused on the second, magnetic, kind of straintronics and its fundamental aspects directly related, due to their generality, to both branches of straintronics, e.g., various effects in bulk and two-dimensional materials associated with symmetry breaking caused by bending, electric fields, and nonuniform distributions of strain and temperature. Special attention is also given to the creation of tailored materials by mechanical stresses and structure deformation, i.e., to strain engineering, an allied field of materials science.

The layout of the review is as follows. Section 1 familiarizes the reader with the main concepts of straintronics. Section 2 presents a more detailed consideration of physical phenomena associated with mechanical stresses in magnetic materials. Finally, Section 3 focuses on the practical aspects of production of magnetoelectric composites and operating principles of straintronic devices.

[2] Lower limit of energy consumption of computation observed in Refs [21–24] can be estimated at 0.1–1.0 fJ from the magnetic hysteresis loops for 10-nm thick nanodisks of ferromagnetic materials (Co, FeGa, etc.) 100 nm in diameter.

1.2 Cross effects involving the elastic subsystem

Deformation represents only one of the possible responses of a crystal to mechanical stress; in the context of straintronics, it plays the role of a 'mediator' through the agency of which it is possible to influence other crystal subsystems (electronic, magnetic, and dielectric). Interactions between the subsystems are responsible for manifesting cross effects, such as piezoresistive, magnetoelastic, piezoelectric, electrostrictive and magnetoelectric ones, etc. (Fig. 3).

Magnetoelastic effect (*Villari effect*, 1865), or alteration of the magnet magnetization caused by mechanical strain, is intrinsic to various extents in all magnetically ordered crystals. It is actually the inverse *magnetostrictive* response (D P Joule, 1842), i.e., deformation of a magnet in the magnetic field.

Either of these effects is a manifestation of the *magnetoelastic interaction* underlying the linkage between a crystal lattice and spin subsystem. This interaction is due to the dependence of exchange, dipole-dipole, or magnetic anisotropic interactions of magnetic moments of ions or atoms on the distance between them. Crystal magnetization changes the character of these interactions and thereby alters the interparticle distance; conversely, an alteration of distance between the particles changes the strength of interaction between magnetic ions and thereby causes a variation of the mean magnetic moments (magnetization), Curie temperature, magnetic anisotropy, and other parameters.

In the strain linear approximation, magnetoelastic and strictive events are represented by a contribution to the thermodynamic potential in the form

$$F_{\text{M-elast}} = b_{ijkl}\, u_{ij}\, n_k\, n_l\,, \tag{1}$$

where b_{ijkl} are the tensor components of the magnetoelastic constants, u_{ij} is the strain tensor, n_i is constituents of the unit vector of the magnetic order parameter.

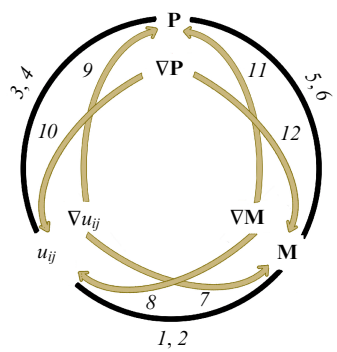

Figure 3. Cross effects coupling mechanical, magnetic, and electric systems in a crystal: *1*, *2* — piezomagnetic effect and magnetostriction; *3*, *4* — piezoelectric effect and electrostriction; *5*, *6* — magnetoelectric effects (linear and quadratic in **M**); *7* — flexomagnetic effect; *8* — converse flexomagnetic effect; *9*, *10* — direct and converse flexoelectric effects; *11*, *12* — direct and converse flexomagnetoelectric effects, respectively. **M**, **P**, u_{ij} — magnetization, electric polarization, and strain tensor components, respectively.

An analog of magnetostriction in the dielectric subsystem is *electrostriction*, where the unit polarization vector is the order parameter **n** in formula (1).

The components of the order parameter **n** occur an even number of times in expression (1), which implies invariance of tensor components of the magnetoelastic constants with respect to the time reversal procedure (T-parity). On the one hand, this accounts for the universal character of magnetostrictive effects in magnetically ordered materials, because they do not impose additional symmetry constraints. On the other hand, T-parity means the impossibility of *180-degree switching of magnetization*, i.e., reversion of its direction, in response to applying a purely mechanical load. Indeed, both components of order parameter **n** in formula (1) change signs making the two states with oppositely directed **n** energetically indistinguishable.

Mechanically driven reversal of the order parameter in the opposite direction becomes possible for a *linear* coupling between the order parameter and strain, as in direct and converse *piezoelectric* effects:

$$P_i = d_{ijk} u_{jk} \,, \tag{2a}$$

$$\sigma_{jk} = d_{ijk} E_i \,, \tag{2b}$$

where d_{ijk} is the piezoelectric modulus tensor, **P** is electric polarization, σ_{jk} is the mechanical stress tensor, **E** is the electric field, and u_{ij} is the strain tensor.

The presence of the piezoelectric effect implies a substantial narrowing of the class of materials being considered. Indeed, because equations (2) include polar vectors **E**, **P** changing sign under effect of the spatial inversion operation, while deformation — responsible for electric polarization — is invariant with respect to this operation, the components d_{ijk} of the piezoelectric tensor must change sign, too. In other words, it is a case of media lacking a center of symmetry.

A similar phenomenon (piezomagnetic effect and linear magnetostriction) is observed in antiferromagnets and weak ferromagnets [26, 27]. In this case, expression (1) contains two components of the order parameter **n** in the form of components of antiferromagnetic (**l**) and magnetization (**m**) vectors, respectively. Formally, such mixed invariant $u_{ij} l_k m_l$ is linear in terms of magnetization **m**, but it retains T-parity owing to the presence of the second magnetic order parameter l; therefore, the problem of 180-degree switching in magnetic electronics remains. Due to the T-parity of the mechanical strain, the change in its sign does not entail the change in the sign of magnetization, and the magnetization direction is determined by the direction of the other order parameter — the antiferromagnetic vector.

In the majority of cases, mechanical deformation in straintronic heterostructures is induced electrically via the piezoelectric layer mechanically connected to the layer of a magnetic material. A change in the magnetic state of matter under the effect of an electric field suggests the presence of efficient *magnetoelectric* interaction [4]. Because the latter in such composite structures is in essence the product of piezoelectric (2) and magnetoelastic (1) interactions [28], it will be linear in electric field and quadratic in magnetization, which means that switching electric polarity will turn magnetization vector by 90° rather than 180°.

As far as cross effects are concerned, a group of phenomena should be mentioned that have the prefix '*flexo*' (from Latin *flexura* — bend) in their names.

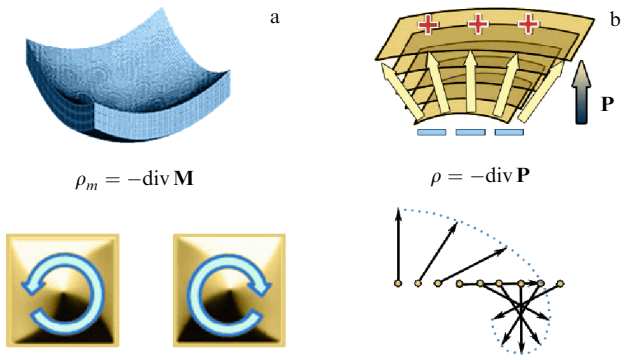

Figure 4. Flexomagnetism and flexomagnetoelectricity. (a) Bending a ferromagnetic plate creates nonuniformity in magnetization distribution, e.g., in the form of vortex distribution with chirality determined by the bend direction (see the lower part of the figure) [33]. (b) Similar to a mechanical bend giving rise to electric polarization, a 'bend' in magnetization distribution (that transforms into a spin cycloid while extending continuously, as in the lower part of the figure) electrically polarizes the magnetic dielectric [35].

The term *flexoelectric* effect defines the appearance of electric polarization in matter with a strain gradient usually induced by bending. The inverse effect implies the emergence of mechanical deformation in a nonuniform electric field. The flexoelectric interaction is described by the contribution to the thermodynamic potential in the form [29]

$$F_{\mathrm{FlexoE}} = \frac{f}{2}\left(P\,\frac{\partial u}{\partial x} - u\,\frac{\partial P}{\partial x}\right), \tag{3}$$

where f is a constant of the flexoelectric effect, P is the electric polarization, and u is the deformation.

The presence of flexoelectric effect, unlike the piezoelectric one, does not impose symmetry constraints on the choice of a crystal, since its cause (gradient strain) breaks the spatial inversion of the crystal. Due to this, the flexoelectric effect is intrinsic to all dielectrics. The inverse flexoelectric effect can be used to deform a straintronic heterostructure with the aid of a nonuniform electric field (e.g., from a scanning microscope tip) in the absence of a special piezoelectric layer.

The magnetic analog of flexoelectricity is *flexomagnetism* [30–34] coupling the strain gradient field ∇u and nonuniform distribution of magnetization **M**. In the case of flexomagnetism, inhomogeneous deformation changes in the magnetization distribution (e.g., gives rise to chiral magnetic structures and vortices (Fig. 4a) [33]), whereas the nonuniform magnetization distribution causes mechanical strain [32]. The magnetism of curved surfaces is considered in a special review [36].

The third group of flexoeffects includes *flexomagnetoelectric* effects [37–39] linking magnetic and electric order parameters with their gradients (arrows *11* and *12* in Fig. 3). Due to the flexomagnetoelectric interaction, spatial modulation of magnetization induces electric polarization in multiferroics [40], while an electric field can influence the domain boundaries [41, 42], vortices [35], skyrmions, and other magnetic topological defects [43]. The converse effect [44] suggests a variation of the magnetic state owing to gradient distribution of electric polarization, created, for example, in the strongly nonuniform field of a point electrode or scanning

microscope tip [45]. Flexomagnetoelectric effects, like magnetoelectric ones, can be realized both by means of mechanical deformation (in this case there is a bend of the crystal) and without it, in the latter case the solid remains intact and the 'bend' occurs in the magnetic subsystem in the form of spin cycloids (Fig. 4b). Such spatially modulated spin structures are analogous to molecular cycloids emerging in nematic liquid crystals under the effect of an electric field [46]. Structures formed by nematic molecule axes that can be regarded as a 'bend' in the order parameter (director) distribution inside a liquid crystal are nothing but a manifestation of flexoelectric interaction described by the contribution to the free energy in the following form

$$F_{\mathrm{FlexoME}} = \gamma \mathbf{P}\left[\mathbf{n}\,\mathrm{div}\,\mathbf{n} - (\mathbf{n}\nabla)\,\mathbf{n}\right], \tag{4}$$

where γ is the interaction constant, $\mathbf{P}$ is the electric polarization vector, and $\mathbf{n}$ is the order-parameter unit vector represented by the director in liquid crystals and by the magnetization or antiferromagnetic vector in magnetically ordered media [46]. This example emphasizes once again the close analogy between different kinds of phenomena, the names of which have the prefix 'flexo'.

The microscopic mechanism of magnetoelectric and flexomagnetoelectric effects is constituted by spin–orbit interaction resulting from the breakup of spatial inversion in a material, e.g., as a consequence of polar distortions of the ideal perovskite structure in multiferroic oxides [47]. This assertion holds for both bulk and 2D crystals. By way of example, bending of the double layer in the tungsten chalcogenide WTe_2 evokes in it a spin–orbit interaction forbidden by symmetry in the nondeformed state [13]. The same symmetry considerations suggest the availability of spin–orbit interactions induced by an electric field [11]. Another example of the spin–orbit interaction in two-dimensional materials concerns the formation of spin cycloids in monolayers of magnetic metals [48–50]. In this case, the 'surface' variant of the flexomagnetoelectric effect takes place, being associated with electric fields at the film–substrate interface and the film free surface.

Mechanical deformation of magnetic films is rendered possible by a variety of methods (Fig. 5):

— directly, by bending or using a substrate with a different lattice constant (*strain engineering*) (see Section 1.3);

— with the aid of an electric field, due to the converse piezoelectric effect (in magnetoelectric composites [see Sections 1.4 and 3)] and the flexoelectric effect;

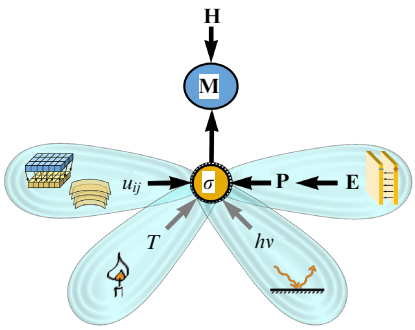

Figure 5. Possible schemes for manipulating magnetization **M** by the direct influence of a magnetic field and by deformation due to mechanical stress, the piezoelectric effect, thermo-induced and light-mediated effects.

— taking advantage of thermo-induced effects due to different thermal expansion coefficients of the magnetic film and the substrate or phase rearrangement of the crystallographic structure of the substrate whilst being heated (see Section 2.4);

— using optical irradiation due to photo-induced striction [9, 51]. Thus, the possibility of switching mechanical stresses with giga- and tera-hertz frequencies has been demonstrated for multiferroic bismuth ferrite [52].

A combined approach relying on several methods is equally possible.

The same techniques of strain engineering and electro- and thermo-induced action on the matter are employed in the physics of 2D materials. An electric field-induced influence on graphene electroinduction is possible by placing it on a piezoelectric substrate (the piezoelectric effect in graphene is forbidden for symmetry considerations) [53] or doping with lithium, which imparts piezoelectric properties to the material [54]. For example, to measure the influence of strain on graphene transport properties, it is placed on a flexible polymeric substrate [55]. Mechanical stresses in graphene are also induced thermally, taking advantage of the difference between thermal expansion coefficients of this or other 2D materials and the substrate [56–58].

The above examples illustrate the generality of the problems under consideration and the approaches employed in straintronics of graphene and two-dimensional media, on the one hand, and in straintronics of multiferroics and magnetic materials, on the other hand. It can be hoped that some initial duality of the notion straintronics will be overcome in the future owing to a convergence of its two branches.

1.3 Strain engineering

The term 'strain engineering' is a technology for producing materials with the desired properties by means of mechanical stresses. This term came into scientific use much earlier than 'straintronics' [59]. Strain engineering should be distinguished from 'engineering strain', by which is meant technical or (in physics) relative deformation.

Strain engineering initially used in semiconductor technologies [59–61] as a strategy for controlled change of material properties was later extended to magnetic [62, 63] and ferroelectric [64, 65] films, then to graphene [66, 67] and other 2D materials.

Mechanical stresses and strains, both homogeneous and inhomogeneous, are brought about in thin films during their epitaxial growth (Fig. 6a) due to the difference between crystal lattice constants of the film and the substrate, which is characterized by the so-called *X-ray strain* [68]

$$\varepsilon = \frac{\Delta a}{a} = \frac{a - a_0}{a_0}, \tag{5}$$

where a is the lattice constant of the film material, and a_0 is the lattice constant of the substrate.

Bulk materials are destroyed at a relative deformation of about 0.1%, unlike epitaxial films of oxide materials, in which relative deformation amounts to several percent [71].

Another method for producing deformation is mechanical action on a substrate coated with the study material (Fig. 6a, bottom picture). For example, a substrate can be bent and oversprayed with a magnetic film [72] (see Section 2.2 for details), or a graphene layer can be deposited on the

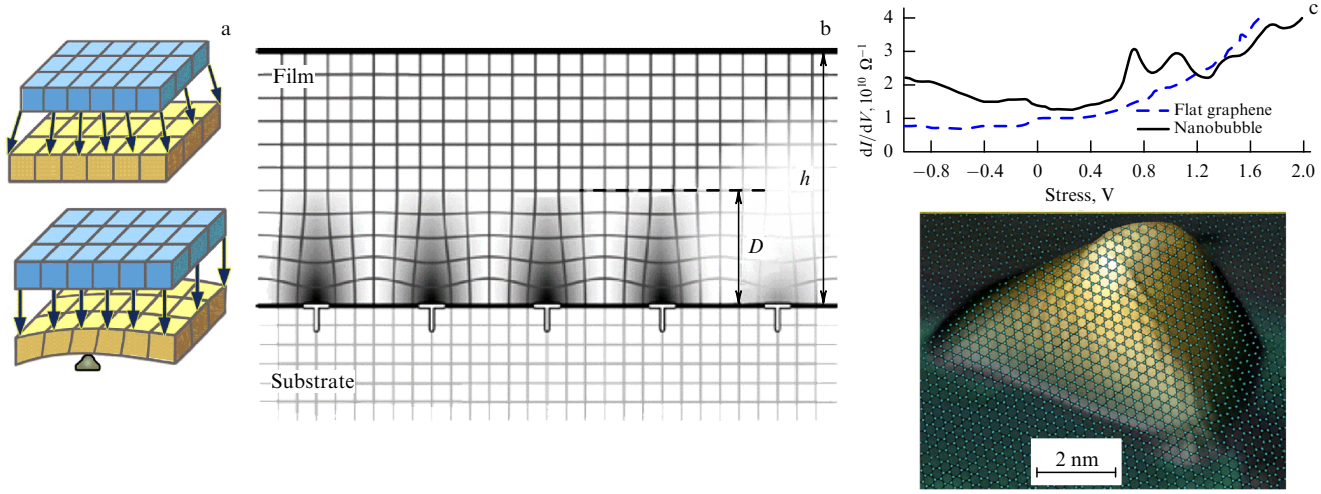

Figure 6. Strain engineering. (a) Creation of materials with a designed anisotropy: epitaxial growth of films on substrates differing in lattice constants and the deposition of the film on the bent substrate. (b) Inhomogeneous stress near the interface in a heterostructure: h — film thickness, and D — characteristic thickness of inhomogeneously stressed region (borrowed from paper [69] by courtesy of the authors). (c) Schematic of the inhomogeneous strain of a graphene lattice at the site of nanobubble formation (bubble height of ~ 1 nm is scaled up for clarity); the upper part shows the dependence of the STM signal on tip voltage for two surface regions: graphene bubbled surface (solid curve) and smooth surface (dashed curve) (plot reproduced from Ref. [70] by courtesy of one of the authors, M Crommie).

substrate [73, 74]; also, substrates can be subjected to homogeneous longitudinal deformation [75]. This may result in strong asymmetry: compressive strain in graphene does not exceed 0.1% (higher mechanical stresses relax spontaneously owing to the appearance of folds and wrinkles on the graphene surface), while tensile strains may be quite huge (tens of percent). Local actions can be realized with the use of scanning probe microscopy methods either by exerting the mechanical pressure with the cantilever of an atomic-force microscope (AFM) or optomechanically with the probe of a near-field microscope [76].

The electronic, magnetic, and ferroelectric properties of films are significantly different from those of bulk materials. Thus, epitaxial stresses affect the Curie temperature of thin ferroelectric films [71]. A characteristic example is strontium titanate $SrTiO_3$, which remains paraelectric when unstressed at arbitrarily low temperatures, but even a moderate (in terms of strain engineering) deformation of $\sim 1\%$ causes its transition into the ferroelectric state at room temperature [64]. This phenomenon is of great interest for applications. Epitaxial stresses in magnetic materials can also shift the point of magnetic ordering [77]. Another consequence of mechanical stresses in magnetic materials is magnetic anisotropy evoked by the magnetoelastic effect [see Eqn (1)], which allows the magnetic phase transitions to be induced by mechanical stress. Since magnetic anisotropy is one of the main factors in micromagnetism, there is a possibility to manipulate the magnetic domain structure by mechanical actions (see Section 2.2 for details). In multiferroics, the dependence of magnetic and electric properties on the state of the mechanical subsystem in the material is especially well pronounced [71, 78]. Strain engineering of multiferroics is discussed in Section 2.3.

The epitaxial growth of films poses the problem of creating the homogeneous elastic deformations with a 1% lattice parameter mismatch: such deformations are realized only in rather thin (pseudomorphic) films. The elastic strain energy increases with film thickness and decreases upon relaxation of elastic strains due to dislocation formation. The distribution of relieved strains becomes nonuniform, and they frequently form a characteristic periodic structure (Fig. 6b) [69, 79]. Naturally, it makes difficult an interpretation of experimental results.

In the case of graphene and other 2D materials [7], the loss of one dimension makes impossible the formation of *threading dislocations* within the thickness of the film, but the problem of *lateral dislocations* in the film plane remains. The accompanying inhomogeneous mechanical stresses produce an effect (the appearance of *an effective magnetic field*) that deserves special consideration in the context of magnetic straintronics.

Mechanical strains markedly change the electronic properties of 2D materials, while the mechanical stress gradient causes a transverse drift of conduction electrons during the passage of current [80], which is equivalent to the action of a magnetic field associated with components of the strain tensor as follows:

$$\mathbf{H} = \operatorname{rot} \mathbf{A}\,, \quad \mathbf{A} = \frac{\beta}{a} \begin{pmatrix} u_{xx} - u_{yy} \\ -2u_{xy} \end{pmatrix}, \tag{6}$$

where $a = 0.14$ nm is the lattice constant, $\beta \sim 2$ is the parameter connected with nearest-neighbor hopping conductivity, and u_{ij} are components of the strain tensor.

Direct confirmation of the presence of effective magnetic fields was obtained by scanning probe microscopic studies of graphene nanobubbles formed during its cooling down on a platinum substrate (Fig. 6c). The sites of bubble formation undergo 10% relative deformations [70]. Measurements of the graphene local electronic structure by scanning tunneling microscopy reveal quite apparent peaks in the local density of states at certain energies positioned equidistantly a few hundred millielectron-volts apart, which corresponds to the Landau levels in an effective field of up to 300 T (see the plot in Fig. 6c) [70]. The effective magnetic field locally changes the transport properties of a material, thus making the graphene nanobubbles to be a sort of quantum dots, and the folds of the graphene sheets to be a sort of quantum wires [81].

1.4 Composite materials of magnetic straintronics

Of special interest in the context of straintronics are composite materials, including different phases, the properties of which are altered by strain. Interactions between these phases give rise to new combinations of properties, as illustratively exemplified by artificial composites containing two phases: magnetic (from ferro- or ferrimagnets) and ferroelectric. The former undergo magnetostrictive deformation in an external magnetic field, while most of the latter show the piezoeffect. Strain-mediated interactions of composite components at the interfaces between them result in the occurrence of magnetoelectric (ME) effect as a combination of magnetostriction and the piezoeffect, i.e., in coupling the magnetic and electric parameters of the material [28].

In the case of the direct ME effect, a magnetic field H applied to the material causes deformation of its ferromagnetic component that is transferred to the ferroelectric one and gives rise to electric polarization P and electric field E by virtue of the piezoeffect. The direct ME effect is characterized by coefficient $\alpha_d = \delta P/\delta H$. In the case of the converse ME effect, the applied electric field E creates via inverse piezoeffect the deformation in the ferroelectric phase that is transferred to the magnetic phase, wherein converse magnetostriction [Villari effect; see formula (1)] alters magnetization M or magnetic anisotropy field H_a. The converse magnetoelectric effect is characterized by its own conversion coefficient $\alpha_c = \delta M/\delta E$.

The degree of coupling of magnetic and electric parameters in composites depends on the strain dimension and coefficient of strain transfer across the phase boundary. Figure 7 depicts schematically the main species of two-phase composite materials with 0–0, 0–3, 1–3, and 2–2 type deformations [82]. Paired digits denote the number of spatial coordinates along which deformation is transmitted in each phase, the first digit relating to the magnetic phase, and the second to the ferroelectric one. A composite with 0–0 type deformations contains magnetic and ferroelectric particles inserted into a neutral matrix. A composite with 0–3 type deformations is made up from separate magnetic particles localized in the ferroelectric matrix, whereas a composite with 1–3 type deformations comprise rods made of magnetic material and resided in a ferroelectric matrix. As this takes place, particles and rods of 0–0, 0–3, and 1–3 composites can be distributed in the matrix either regularly or chaotically. A composite with 2–2 type deformations looks like a planar structure made up of two or more alternating magnetic and ferroelectric layers. Obviously, the ME properties of composites can be altered in a broad range by selecting appropriate phase materials, changing their volumes, and varying specimen size.

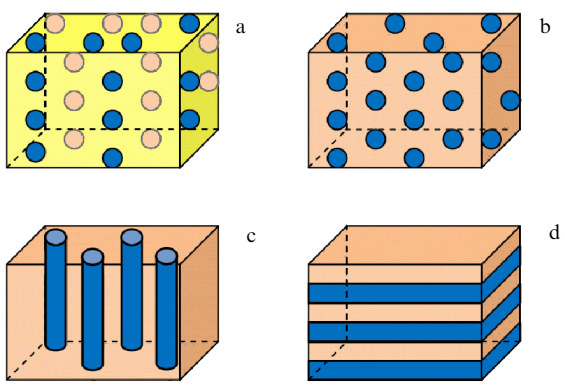

Figure 7. (Color online.) Composite structures with various types of deformations: (a) 0–0; (b) 0–3; (c) 1–3, and (d) 2–2. Yellow color marks the matrix, beige the piezoelectric, and blue the ferromagnet.

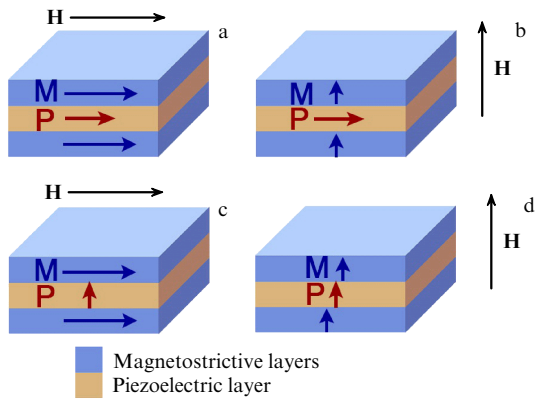

Figure 8. Directions of magnetization **M** and polarization **P** in two-layer structures; **H** — external constant magnetic field.

Of special interest for straintronic applications of the above composites are layered structures with two-dimensional 2–2 type deformations that are relatively easy to prepare in the form of rectangles, squares, disks, or rings of various sizes. In such structures, high-conductivity magnetic and piezoelectric layers are separated and retain their physical properties, which makes it possible to efficiently polarize the latter layers.

Figure 8 shows possible directions of magnetostrictive layer magnetization and piezoelectric layer polarization for the structure considered. In a structure tangentially magnetized by an external magnetic field **H** (Fig. 8a, c), demagnetization effects are inappreciable and deformation of the magnetic layer is saturated in weak fields; in the case of normal magnetization, saturation occurs in much stronger fields. The ferroelectric layer is easy to polarize throughout its thickness (Fig. 8c, d) by applying low voltage across the electrodes; polarization of this layer in the structure plane requires a much higher voltage.

A detailed description of materials currently used to produce straintronics composite structures, methods for manufacturing structures with layers of various thicknesses, characteristics of direct and converse ME effects in them, the potential to apply them for the development of magnetic memory devices, and sensor and microwave technologies are presented in Section 3.

1.5 Operating principle of magnetic straintronic devices

The principle expounded in Section 1.4 allows not only creating materials with magnetoelectric interaction linear in the electric field, but also reversing magnetization in the magnetic layer by applying voltage across the piezoelectric layer. This possibility is of interest in the first place for the magnetic memory industry, because magnetization switching is one of the constituent components of the *magnetic recording trilemma*. Its components (readout, recording, and storage) impose divergent requirements on the information-carrying magnetic medium [83]. Indeed, a successful solution of the problem of long-term storage of information implies a stability of magnetization with respect to the external

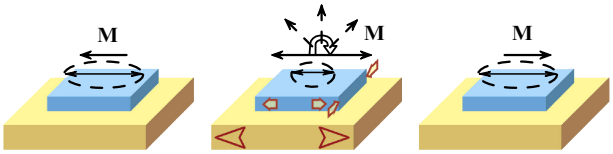

Figure 9. Illustration of the idea of strain-assisted recording. A memory element from a magnetic material is mechanically coupled to a piezoelectric layer. The eccentricity of the ellipse reflects the magnitude of magnetic anisotropy, the double-pointed arrow shows the direction of the easy magnetic axis, and hollow axis indicates mechanical stresses in the layers [84]. The torque rotating magnetization is caused either by an additional impact of a magnetic field or spin-polarized current.

perturbations that is reached by enhancing the magnetic anisotropy of the medium that, in its turn, increases the control current density and complicates data recording.

The electric field responsible for deformation of the piezoelectric substrate can weaken magnetic anisotropy in the recording layer due to the Villari effect and facilitate its transition into the state with an opposite orientation of magnetization (Fig. 9) [84]. This mode of magnetic recording is called strain-assisted recording [85–87] by analogy with heat-mediated magnetic recording. The latter technology makes use of material heating up to temperatures close to the Curie point to reduce its magnetic anisotropy and facilitate remagnetization.

The term 'strain-assisted' implies the auxiliary role of mechanical strain. Indeed, neither deformations nor the electric field can by themselves turn magnetization 180° for symmetry reasons (see Section 1.2). The magnetization rotation is driven by magnetic field pulses [87] or spin-polarized current [85] that remove symmetry degeneracy in the sign of magnetization projection onto the anisotropy axis (see Fig. 9).

However, these fundamental restrictions do not make straintronics a 'Cinderella' in spintronic family. First, there are various means to circumvent symmetry prohibition on electrically induced 180-degree rotation of magnetization, as shown in Section 2.1. They permit creating elements of magnetic memory, logic devices, and systems for image processing (see Section 3.2) and open up new prospects for the further development of innovative neuromorphic electronics (see Section 3.5).

Second, many devices operate without complete reversal of magnetization: two logical states can be given by mutually perpendicular orientations (see Sections 2.1 and 3.2).

Third, a local change in magnetic anisotropy with the aid of point electrodes results in the transformation of the micromagnetic structure of the material (see Section 2.2 for details); this phenomenon is not only of theoretical interest but is equally important for the development of race track memory [88] with electrically managed magnetic domain boundaries [89] and skyrmions [90].

2. Physical effects in magnetic micro- and nanoparticles and structures induced by mechanical stresses

2.1 Magnetization switching in particles

One of the most promising approaches to superdense magnetic recording of information is based on remagnetization of single-domain particles. The stability of a recorded state is supported by magnetic anisotropy created artificially by shaping the single-domain particles as ellipsoidal disks. Therefore, the optimal configuration of magnetic recording is one in which two logical states correspond to opposite magnetization directions parallel to the particle's long axis, and the magnetic re-recording process is nothing but magnetization rotation by 180°. Usually, such rotation is effected by the external magnetic field of the recording head [91]. As was mentioned in Section 1, realization of analogous magnetization switching by an electric field is a serious challenge from both fundamental and technical standpoints. This physical problem needs to be considered in greater detail, since its solution would drastically reduce energy consumption and ensure high reliability of information recording and storage.

In semiconductor electronics, the energy dissipated during the entry of one bit of information is on the order of $Nk_{\mathrm{B}}T\ln(1/p)$, where N is the number of electrons (information carriers) transferred into or out of the device, k_{B} is the Boltzmann constant, T is the temperature, and P is the probability of error in a binary digit bit arising from incorrect switching of the device, attributable to thermal noise [92]. Given that 0 and 1 are encoded in two stable magnetization orientations along the easy axis of a single-domain anisotropic nanoparticle, the energy dissipated during switching between these orientations for bit reversal is $\sim k_{\mathrm{B}}T\ln(1/p)$ [92, 93], because 'information carriers' in single-domain magnetic nanoparticles are electron spins (in contrast to electron charges in transistors); mutual exchange interaction between them maintains their collective behavior during re-magnetization. Taken together they behave like atoms with a giant classical magnetic moment (macrospin) that serves as an elementary information carrier [92–94]. Therefore, a magnetic nanoparticle dissipates energy of order $k_{\mathrm{B}}T\ln(1/p)$. With the same probability of bit recording error p, the ratio of the minimal energy dissipated for switching a nanoparticle to the energy dissipated in nanotransistor switching is $\sim 1/N$, i.e., much smaller than unity, because N is large. It makes a magnetic nanoparticle a much more efficient switch in terms of energy saving than a transistor. Moreover, a single-domain particle is less sensitive to noises at room temperature than a single-spin device [93]. For this reason, computations based on the use of a single-domain anisotropic nanoparticle with two stable orientations of magnetization have a double advantage, viz. a very small dissipated energy for switching and resistance to thermal noises at room temperature.

In the role of these nanoparticles it was proposed in Refs [93, 95–98] to use submicron-scale ferromagnetic disks of ellipsoidal shape, as thick as a few dozen nanometers, with homogeneous magnetization parallel to the long axis of the ellipse at room temperature. If a particle is placed on a piezoelectric substrate, an electric potential V applied across the substrate induces mechanical stresses (σ) and changes the orientation of magnetization in the particle due to the magnetoelastic effect [99]. For example, stretching an ellipsoidal Co nanoparticle with a negative magnetostriction coefficient turns its magnetization through 90° [23]. The particle remains in this state only in the presence of induced mechanical stress; after its relaxation (following voltage V switch-off), the total magnetization vector **M** either returns to the starting position or rotates through 180° relative to the initial direction, with equal probability, due to the symmetry

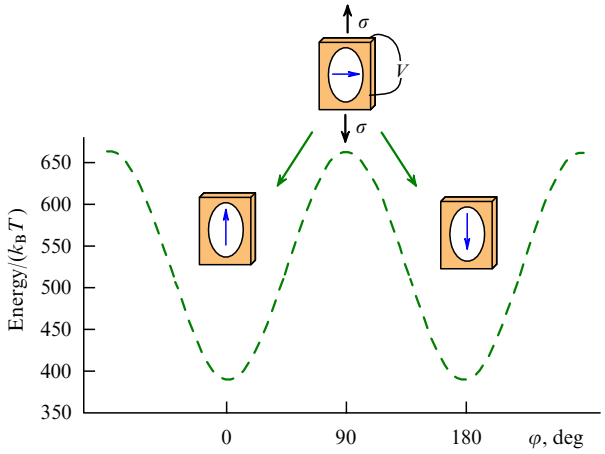

Figure 10. Dependence of the potential energy of a single-domain particle on the orientation of its magnetization. Representation of particle magnetization vector rotation upon tensile strain induced from a piezoelectric substrate.

of the potential energy curve of the particle, depending on the orientation of its magnetization (Fig. 10). However, symmetry can be broken in real setups. For example, experiments reported in Ref. [23] showed that only in two of the nine Co particles observed with a magnetic-force microscope (MFM) had magnetization rotated through 180° after stress relieving.

Manipulation of particle magnetization by induced mechanical stresses has been addressed in numerous theoretical studies [3, 5, 92, 93, 98, 100–118] and a recent review [119]. These papers were based on the Stoner–Wohlfarth model [94] assuming that the magnetic dynamics of a small single-domain particle exposed to an external action can be described by the motion of the total magnetic moment (macrospin **M**) during coherent rotations of magnetic moments of individual atoms in the particle. According to this model, the main quantities determining the potential energy of a single-domain particle W are energies conditioned by shape anisotropy (W_{shape}), magnetoelastic anisotropy (W_{strain}), and dipole–dipole interaction (W_{dip}) (the last is taken into account when particles are close to one another). Sometimes, Zeeman and magnetocrystalline energies needs to be taken into consideration as well [93]. The energy of magnetoelastic anisotropy depends not only on the particle volume Ω but also on saturation magnetostriction λ_s and the orientation of components of the induced stress tensor σ with respect to particle axes:

$$W_{\text{strain}}(t) = -\left(\frac{3}{2}\lambda_s \sigma \Omega\right) \sin^2\theta(t) \sin^2\varphi(t)\,, \tag{7}$$

where θ, φ are the orientation angles.

The dynamics of the temporal evolution of the magnetization vector **M** of a single-domain ferromagnetic particle under the effect of mechanical stresses is described by the Landau–Lifshitz–Gilbert (LLG) equation [93, 100, 120]

$$\frac{\mathrm{d}\mathbf{M}}{\mathrm{d}t} = -\gamma(\mathbf{M}\times\mathbf{H}_{\text{eff}}) + \frac{\alpha}{M_s}\left(\mathbf{M}\times\frac{\mathrm{d}\mathbf{M}}{\mathrm{d}t}\right), \tag{8}$$

where γ is the gyromagnetic ratio, and α is Gilbert's dissipation (relaxation) parameter. The effective magnetic field acting on magnetization is given by the expressions

$$\mathbf{H}_{\text{eff}}(t) = -\frac{1}{\mu_0\Omega}\frac{\mathrm{d}W(t)}{\mathrm{d}\mathbf{M}} + \mathbf{H}_s + \mathbf{H}_{\text{thermal}}(t)\,, \tag{9}$$

$$W(t) = W_{\text{shape}}(t) + W_{\text{strain}}(t) + W_{\text{dip}}(t)\,, \tag{10}$$

where Ω is the particle volume, M_s is the saturation magnetization, μ_0 is the permeability of a vacuum, $\mathbf{H}_s$ is the external magnetic field, and H_{thermal} is the magnetic field induced by thermal vibrations of the lattice magnetic atoms and described by a Gaussian distribution [121].

To evaluate the contribution of thermal vibrations to re-magnetization processes, the initial Gaussian distribution of the magnetization vector orientation with different weights corresponding to a given temperature is defined and equation (8) solved for each initial **M** orientation [93, 121]. The number of equations to be solved may be as large as 10^6 to collect switching statistics in the presence of random thermal perturbations. This yields a set of trajectories $\mathbf{M}(x, y, z, t)$ allowing us to estimate the contribution of thermal noise to re-magnetization processes [103]. Micromagnetic modeling shows that considering the deflection in the initial real orientations of atomic magnetic moments in particles at 300 K, depending on their size and shape, is of special importance for the choice of pulse duration and period-to-pulse duration ratio V responsible for multiple switches of magnetization in particles [122].

The solution of equation (8) demonstrates that mechanical stresses cause the magnetization vector to precess and hold a new position in space [93, 97, 101, 102, 105]. This process is illustrated in Fig. 11.

Figure 11 demonstrates two kinds of precession. Usually (see Fig. 11a), mechanical stress leads to **M** rotation through 90°. After the stress is relieved, the magnetization holds, with an equal probability, a position with the azimuthal angle being either $\theta = 0$ or $\theta = 180°$. However, numerical computations using the LLG equation (8) demonstrated the feasibility of a scenario in which magnetization rotates through 180° with a 99.99 % probability (Fig. 11b) [5, 100–102, 123–125], because precession of the magnetization vector results in its going beyond plane xy. If the voltage is turned off when the projection of the magnetization vector onto the plane xy is oriented in direction $-y$, the torque $\mathbf{M}\times\mathbf{H}_{\text{eff}}$ makes magnetization continue to move in direction $-x$, rotate through 180°, and hold a stable position due to the out-of-plane vector component (Fig. 11b). Modeling for 100-nm Ni, Co, or terfenol-D particles in the absence of thermal noise showed that magnetization can be switched for 1–10 ns by a voltage of ≈ 20 mV applied across the underlying piezoelectric layer, allowing binary information to be recorded at a frequency of 1 GHz with the energy consumption of only ~ 1 aJ on recording a single bit [5, 93]. At room temperature, thermal noises cause the spread in switching times on the order of 0.1 ns, while energy dissipation does not exceed ~ 1.5 aJ, with the probability of switching tending toward 100% [103]. Similar model computations giving evidence of the possibility of a 180-degree switch by stress removing at the proper instant of time are reported in Ref. [101] for ellipsoidal $Co_{40}Fe_{40}B_{20}$ nanoparticles. This principle of dynamic 180-degree switching by electrical voltage alone without additional magnetic fields is not confined to the case of planar geometry: numerical simulations showed the possibility of 180-degree switching also for states oriented normally to the film plane [124, 125].

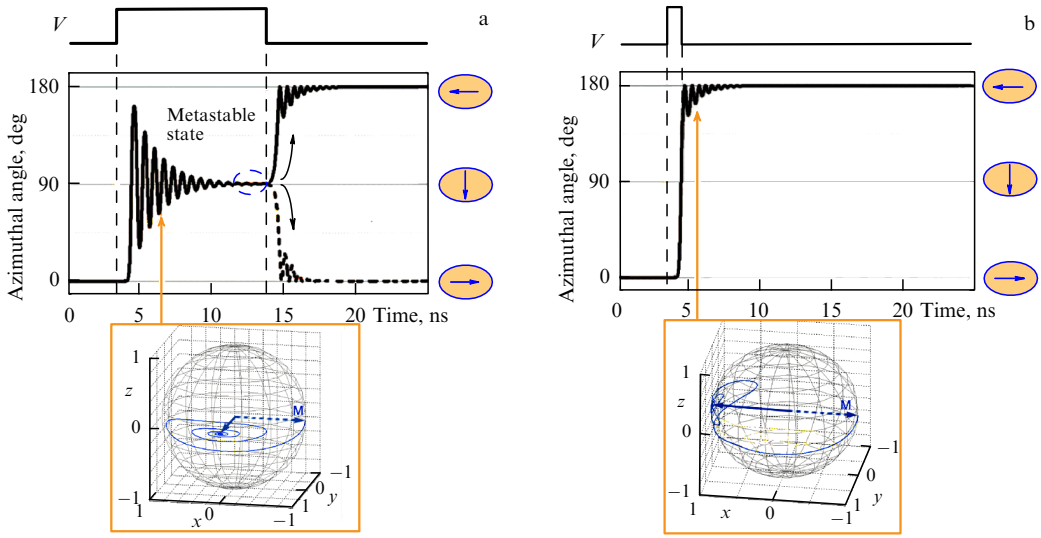

Figure 11. Variation of magnetization vector **M** in time and its precession in space after turning voltage V on and off: (a) in the case of equiprobable return from the metastable state to former and opposite orientations, and (b) in the case of voltage removal at the moment when **M** is out of plane xy, and the azimuthal angle is 90°.

One more variant of the 180-degree switch is based on a series connection of four electrodes in pairs; the electrodes are mounted on the surface of a piezoelectric substrate around the particle (Fig. 12a) [109, 126]. Calculations show that 180° magnetization rotation is possible in this case in the absence of an additional magnetic field. When mechanical stress in a particle is created by the AA′ pair, the energetically advantageous position of magnetization coincides with $\mathbf{M}'$ ($\theta = 60° \pm 4°$) (Fig. 12b). It moves to position $\mathbf{M}''$ ($\theta = 20° \pm 4°$) after shutdown of the AA′ pair and simultaneous application of the electrical potential to the BB′ electrodes. Disconnection of the BB′ pair causes magnetization to 'roll down' to position $\mathbf{M}_1$ (Fig. 12b). The dynamics of magnetization switching with reference to precession and thermal noises is illustrated in Fig. 12c. The spread of angle θ in the curves corresponding to the trajectory of **M** movement with time takes into consideration the contribution from thermal noises. The family of curves was obtained in the computer-assisted solution of up to 10^6 LLG equations; for each of them, the initial $\mathbf{M}_1$ values were given with a spread taking account of thermal vibrations at room temperature [109]. All the trajectories are different due to random thermal noises included in simulations employed to generate these trajectories (Fig. 12c).

The calculated switch time in this case was about 5 ns. The energy consumption for recording one bit of information comprised the energy internally dissipated during **M** movement (Gilbert damping) [93] and the external energy needed to produce mechanical stresses in a particle by means of tension or compression of the piezoelectric substrate during the application of electric potential V to the electrodes on its surface. Taking account of capacity C and the size of this 'sandwich', the energy required is CV^2. For the case in question, the total energy consumption for recording a bit amounts to 25 aJ, i.e., at least two orders of magnitude lower than in spin electronics elements, say for magnetization switching due to the spin-transfer torque effect [127].

Theoretical schemes of 180° magnetization rotation for nanoparticles in the form of a four-petal flower [110] or a square [111] were also proposed (Fig. 13). These particles, unlike ellipsoidal ones, have two mutually perpendicular easy magnetization axes and four stable positions of **M**. Due to this, their gradual tension and compression allow their magnetization to be reversed in two steps, each time through 90 degrees.

To sum up, one may distinguish a few methods for obviating symmetry prohibition (see Section 1.2) on a 180-degree magnetization switch by an electric field:

— a dynamic switch [101, 124, 125] when precessing magnetization passes the 90-degree energy minimum evoked by mechanical stress and 'rolls down' after its relaxation into the second 180-degree minimum of the stressless state (Fig. 11);

— switching in the field of several electrode pairs sequentially transferring magnetization through a few intermediate states [109] (see Fig. 12) with its relaxation in each of them;

— using tetragonally symmetric particles [110, 111] (see Fig. 13) in which a 180-degree switching is implemented in two steps, each time by 90 degrees, taking advantage the generation of consecutive compressive and tensile strains.

It is worth recalling that a 180-degree switching is of great practical value for the efficient operation of devices in which information is read out by virtue of magnetic resistance effects. For other devices, e.g., a magnetoelectric cell [128] in which both recording and reading out are based on magnetoelectric effects, the 180-degree switching is less significant, and the roles of logical zero and unity can be performed by any two states with differently directed magnetizations.

Methods for the creation of two stable states in single-domain particles with angles between their magnetizations other than straight ones are considered in Refs [104–106, 129]. They envisage greater energy expenditures and a bit recording time than in those methods considered in the preceding paragraphs but provide more opportunities for experimental implementation. One of them is the placement of a particle into a constant additional external magnetic field **H** directed along the short axis of an ellipsoidal particle (Fig. 14). In this case, vector **M** can be oriented in one of the two stable directions corresponding to potential energy minima marked

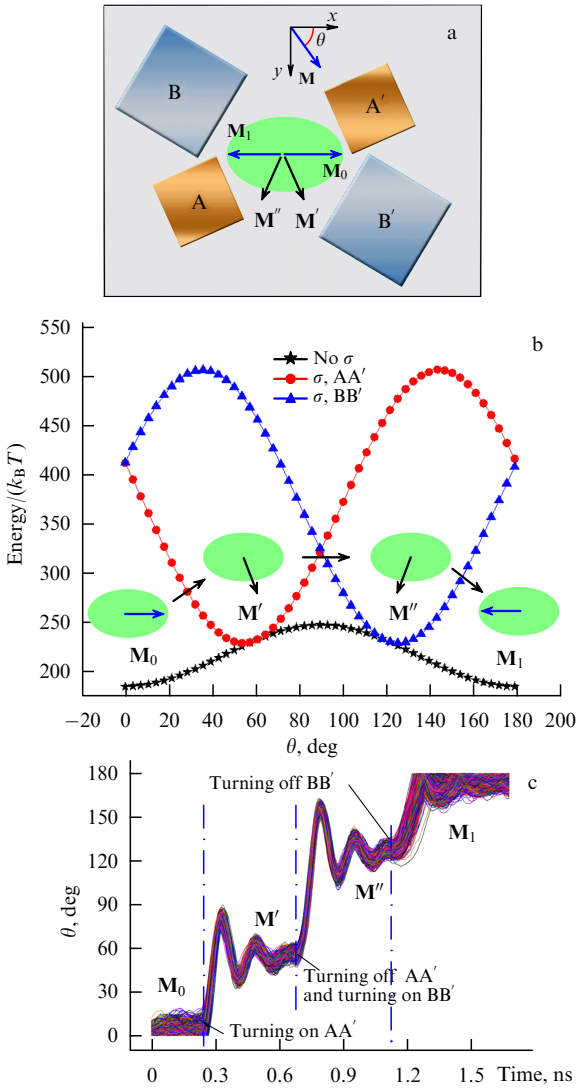

Figure 12. Magnetization rotation through 180° without an additional external magnetic field in the case of a series connection of four electrodes in pairs. (a) Connection scheme and possible magnetization orientations. (b) Potential curves for an elliptical particle in the case of the electrical potential application to different pairs of electrodes and the corresponding orientations of magnetization. (c) A family of curves describing the kinetics of variations in magnetization orientation, taking into account the spread of **M** values due to thermal noises (adapted figure taken from Ref. [109] by courtesy of the authors).

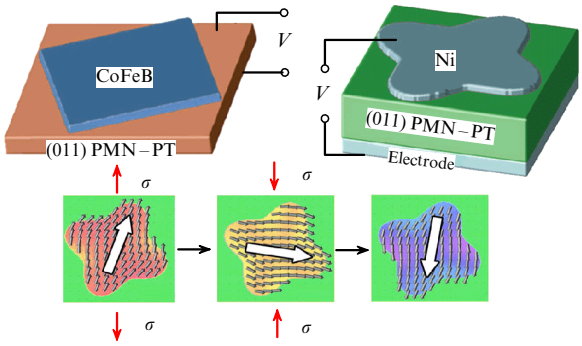

Figure 13. Particles with four stable states and a two-step 180-degree magnetization switch in the upper magnetic layer. (011) PMN–PT is the substrate from a solid solution of lead–magnesium niobate in lead titanate with (011) crystallographic orientation.

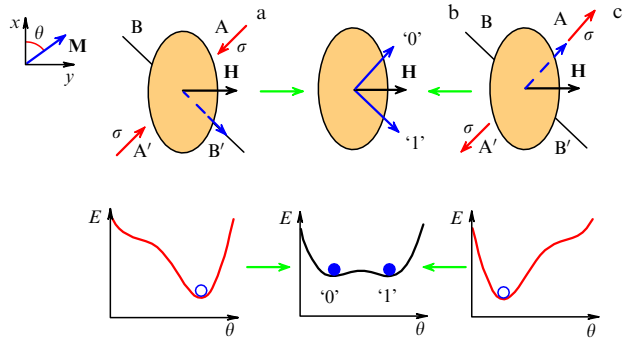

Figure 14. Switching of magnetization orientation in a particle with positive magnetostriction exposed to the combined action of an external magnetic field and tensile/compressive stresses. (a) **M** position in the compressed particle in the presence of a magnetic field **H**. (b) Two possible stable positions of **M** vectors after relief of mechanical stresses. (c) **M** position in the stretched particle in the presence of a magnetic field **H**. The lower part of the figure shows respective angular dependences of particle's potential energy.

as '0' and '1' on the plot of energy E versus magnetization orientation θ (Fig. 14b). The '0' and '1' states are separated by a rather high potential barrier and can be used for energy-independent storage of binary information. Mechanical compression or tension in one of these directions needs to be induced for recording a bit of information. Mounting an electrode on a piezoelectric substrate on either side of the particle along its AA′ axis allows compressing or stretching the particle along this axis, depending on the sign of the electric potential applied to the electrodes. For compression along the AA′ axis, the particle potential passes through a single minimum (Fig. 14a) corresponding to direction B′, while the orientation of **M** will remain in position '1' after relief of compressive strain (moving from Fig. 14a to 14b). In the case of stretching along the AA′ axis, magnetization will be directed parallel to A due to the transformation of the potential curve, and magnetization position '0' will become stable, in which **M** will be fixed after removal of the compression potential (moving from Fig. 14c to 14b). Thus, it is possible to erase or record separate bits by deformation alone. Disadvantages of this method are the necessity to generate an external magnetic field on the order of a few tenths tesla and the relatively small angle between the two stable positions of **M** [104].

To control magnetization, it is possible to employ two pairs of electrodes (four electrodes arranged in pairs on AA′ and BB′ axes around the particle). The application of the electric potential to one of the pairs orients **M** in the desired direction, while saving energy for information recording [106].

Model computations showed that a decrease in the strength H_s of the external field directed along the short axis of the nanoparticle increases the angle between the two stable orientations of magnetization **M**. Even rotation of **M** through 170° is possible, if two electrodes (insulated from the magnetic particle) to which an electric potential is applied alternately are placed directly under its edges to localize stresses induced in the particle [108]. For recording a single bit in this case, an energy of ~ 4 aJ is needed, which is five orders of magnitude lower than with the use of spin-polarized current (the spin-transfer torque (STT) method) [107, 127].

Table 1 illustrates the above-discussed magnetization switching options.

Table 1. Magnetization switching energy and time in different modes of mechanical stress induction in anisotropic particles.

No.	Scheme of electrode arrangement on piezoelectric substrate around ellipsoidal nanoparticle	Material and lateral size of the particle, nm	External additional magnetic fields H_s, mT	Angle between two stationary states of magnetization **M**, deg	Magnetization reversal energy, aJ	Magnetization reversal time, ns	References
1	Two electrodes on one line	$TbFe_2$ 45 × 25	190	90	30	~ 1	[101, 102]
2	Four electrodes in square corners	Ni 150 × 120	11.3	90	8×10^4	4.5	[103]
3	Two electrodes on one line	Terfenol-D 110 × 90	8.5	89	4.7	1.5	[104]
4	Four electrodes in rectangle corners	Terfenol-D 110 × 90	8.5	132	3.5	1.5	[104]
5	Two electrodes under the particle	Ni 130 × 117	0.6	170	200	10	[105]
6	Four electrodes in rectangle corners	Terfenol-D 110 × 90	0	180	25	5.4	[106, 123]

Some recent research in straintronics has been done on the employment of surface acoustic waves (SAWs) [113–115, 130]. It was shown in experiment [130] that SAW excitation using a system of interdigital electrodes on a lithium niobate surface may be a tool for controling magnetization of relatively large (submicron) ellipsoidal Co particles. Specifically, these particles go from the state with homogeneous magnetization to the stable state with a vortex structure. A combination of spin-polarized current and SAW-induced mechanical stresses allows magnetization in magnetic particles to be rotated through 180°, as shown theoretically in Refs [113–115]. SAW-induced mechanical stress on a magnetic particle is compressive in the first SAW half-period, and tensile during the second one. Magnetization turns in the direction of the hard (short) axis during one of the half-periods; in the second half (after an appreciable turn of magnetization under the stress effect), the 180° rotation of **M** with respect to the initial direction is completed due to the spin-transfer torque from spin-polarized electrons to lattice atoms. An advantage of the combined method lies in the fact that the induction of mechanical stresses in particles becomes possible without deploying a system of electrodes around each particle shown in Fig. 12a, because full 180° magnetization reversal occurs only in those particles through which spin-polarized current passes.

2.2 Changes to micromagnetic structure under the action of mechanical stresses

In addition to research on magnetization switching in single-domain particles, many studies are devoted to the rearrangement of the micromagnetic structure under the influence of mechanical stresses in multidomain films and microparticles. Section 2.1 describes the principle of controling the particle magnetization on a piezoelectric substrate by the application of electric potential. However, mechanical stresses can be generated directly in a magnetic film or particle by mechanical deformation, e.g., substrate bending. Then, a combination of two methods for creating mechanical stresses is possible, such as deposition of a magnetic film onto the preliminarily bent piezoelectric substrate [131].

Investigations into the influence of mechanical stresses on the magnetic properties of films have a rather long history (see, e.g., monograph [132]). Ongoing studies on the magnetoelastic properties of films are conducted with the application of modern techniques based on magnetic-force microscopy, ferromagnetic resonance (FMR), the magneto-optic Kerr effect (MOKE), X-ray photoemission, SQUID-magnetometry, and vibromagnetometry. The relationship between the magnetoelastic energy and tensors of mechanical strains and stresses [see formula (7)] provides a basis for model calculations of tensors for concrete substrates and a comparison of theoretical and experimental values of the induced magnetoelastic anisotropy field, one of the key characteristics of the magnetoelastic effect [133].

The simplest method for inducing stresses in films or particles is to bend the substrate on which they are formed. Outward bending of the clamped substrate induces tensile strain in particles (Fig. 15a), while inward bending produces compressive strain. Magnetoelastic effects in such structures can be studied by magnetic-force microscopy. The application of clamps restricts the possibilities of experimental investigation of such objects. Therefore, a different method is often employed where films and particles are formed on preliminarily bent substrates. Unbending the substrate removed from the clamps induces mechanical deformation in the particles. If the substrate was initially bent outward (Fig. 15b), its unbending results in particle compression; if it was bent inwardly, unbending produces tension.

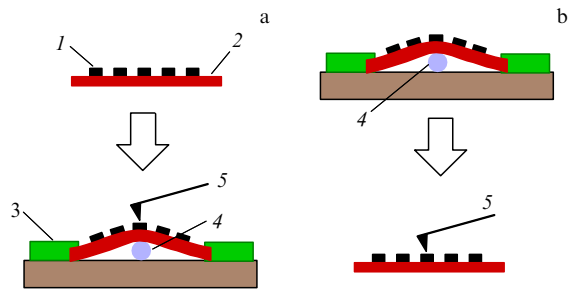

Figure 15. Shaping specimens with particles or films stressed by mechanical strains for registering by MFM. (a) Bending of substrate with the preliminarily formed particles. (b) Formation of particles on preliminarily bent substrate with its subsequent unbending. *1* — particles, *2* — substrate, *3* — clamps, *4* — microwire, and *5* — MFM cantilever.

An advantage of the former approach lies in the fact that it allows the degree of bending to be gradually changed with the use of special clamps and *in situ* controling the formation of magnetoelastic anisotropy by applying different stresses. The second approach to preparing elastically deformed ferromagnetic objects makes it possible to use a wider spectrum of experimental tools due to the absence of a limitation on the size of the specimens.

The latter method was employed, for instance, to study the transformation of hysteresis loops in 50–150-nm thick $Fe_{81}Ga_{19}$ films deposited on a bent polyethylene terephthalate (PET) substrate [134, 135]. The magnetoelastic effect induced in the film markedly changes the residual-to-saturation magnetization ratio (M_r/M_s) [134]. Stressed $Fe_{81}Ga_{19}$ films exhibited noticeable uniaxial magnetic anisotropy due to internal stresses that developed after unbending the PET substrate. An easy magnetization axis formed in the films along the tensile strain direction and the coercive field increased with stress [135]. The M_r/M_s ratio changed with a period of 180° as the sample rotated relative to the external magnetic field vector, which confirmed the presence of stress-induced uniaxial magnetic anisotropy. Similar results were obtained in experiments with 18-nm thick Co films prepared by electron-ray deposition on a preliminarily bent (111) Si substrate [136].

The most prominent changes in the coercive force and M_r/M_s ratio occur in the case of deformation of a 35-nm thick polycrystalline Ni nanofilm deposited on a thin plate of niobate lithium ($LiNbO_3$) crystal. By virtue of bending the crystal with a film, its coercive force enhanced by a factor of 4, up to 80 Oe, while the residual-to-saturation magnetization ratio increased by an order of magnitude up to $M_r/M_s = 1$ [137]. Similarly, large changes in the M_r/M_s ratio were observed in experiments with a bent polyimide substrate coated with a 20-nm thick $Co_{40}Fe_{40}B_{20}$ film [138].

The degree of stress uniformity in magnetic films, wherein the stresses form through a substrate bending, strongly depends on the character of this procedure prior to their deposition. For the wire substrate bending shown in Fig. 15b, nonuniformly distributed compressive stresses linearly increase from the periphery to the center of the specimen, as demonstrated in experiments with the aid of a scanning FMR spectrometer to study 50-nm thick Permalloy films prepared by vacuum deposition onto a glass substrate and confirmed by calculations of strain tensor components in Ref. [133].

Changes in the magnetic properties of micro- and nanoparticles in response to elastic mechanical strains are of primary importance for solving the problems facing straintronics. Such experimental studies are relatively few [72, 139–142]. The employment of various supports for substrate mechanical bending makes it possible to obtain both nonuniform and comparatively uniform distributions of strain tensor components over the sample surface.

The influence of homogeneous and gradient strains induced in the sample on the micromagnetic structure of Permalloy (Py) $Ni_{75}Fe_{25}$ microparticles arranged on its surface was studied in Refs [72, 139, 141]. Unstrained reference specimens of the first type were formed on the surface of a flat glass substrate using a mask in the form of a grid with equispaced 25×25-μm square holes separated by 7-μm bridges. For the specimens of the second type, a similar metallic grid was fixed on the surface of a glass substrate bent with the aid of a metal wire attached beneath it, as shown in Fig. 15b. An ascending periphery-to-center gradient of elastic stresses formed in this substrate. The magnitude of deformation estimated from characteristic parameters of the system (wire diameter 80 μm, substrate thickness 300 μm, substrate length ~ 1 cm) was $\sim 0.1\%$. Finally, the substrate for the specimen of the third type with homogeneous mechanical stress was bent when it was fastened to a cylindrical base with a radius three orders of magnitude greater than the wire radius (ca. 80 mm) to ensure relative strains of the same order of magnitude as in the preceding case but evenly distributed over the specimen. Then, a Py layer 30 nm thick was deposited in a superhigh vacuum on the substrates. With spraying completed, the specimens were removed from the holders; their entire surface was covered with regularly arranged square microparticles.

MFM images of square Py microparticles show the well-known structure of four 90-degrees domains, in which the domain walls converge at one point in the particle center (Landau domain structure) [143, 144]. Such a structure, characteristic of unstressed particles, is observed in practically all of those located on the surface of the type 1 specimen. Uniaxial compression of microparticles in the type 2 specimen results in the transformation of their domain structure, which increases from the edges to the center (Fig. 16a–d). Finally, MFM images of microparticles obtained from different parts of the surface for the third type specimen were practically identical and coincided with the image in Fig. 16c. Such a transformation of the domain structure of square microparticles caused by their mechanical compression was described theoretically in monograph [143].

Reconstruction of magnetization distribution in a particle from its MFM image presented a nontrivial problem that was addressed using additional experimental and numerical methods. At the first stage, the 3D image of the particle, taken with a scanning probe microscope in the AFM mode, served as a basis for simulating the distribution of local magnetic moments in the particle with the aid of the 'Object-oriented micromagnetic framework' (OOMMF) program [145] and data on the effective saturation magnetization of the sample and effective anisotropy field H_k obtained from FMR measurements [139]. At the second stage, the distribution of magnetization in the Py particle thus estimated was utilized to model its MFM image. Calculations at this stage were made with the help of the 'Virtual MFM' program [146]. Theoretical and experimental MFM images were compared. Their coincidence (see Fig. 16) was regarded as a criterion for the validity of the obtained model magnetization distribution.

The obtained local moment distribution suggests that an unstressed particle has the classical Landau structure characteristic of planar square particles. A stressed particle possesses the four-domain structure too, but the domains are different in sizes: those in which the local magnetization direction is perpendicular to the particle compression axis are larger than domains having their magnetization direction parallel to this axis. In such a case, a characteristic inter-domain bridge forms that grows in size as the degree of microparticle compression increases (Fig. 16) [139, 147, 148]. The length of the bridge can serve as a parameter characterizing the degree of deformation of a concrete particle. This parameter, derived from MFM images of the particles in different parts of the specimen, permits assessing the uniformity of stress distribution over the entire sample with a lateral resolution of about 10 μm.

An analogous transformation of the domain structure with forming the bridge between domains in the center of the

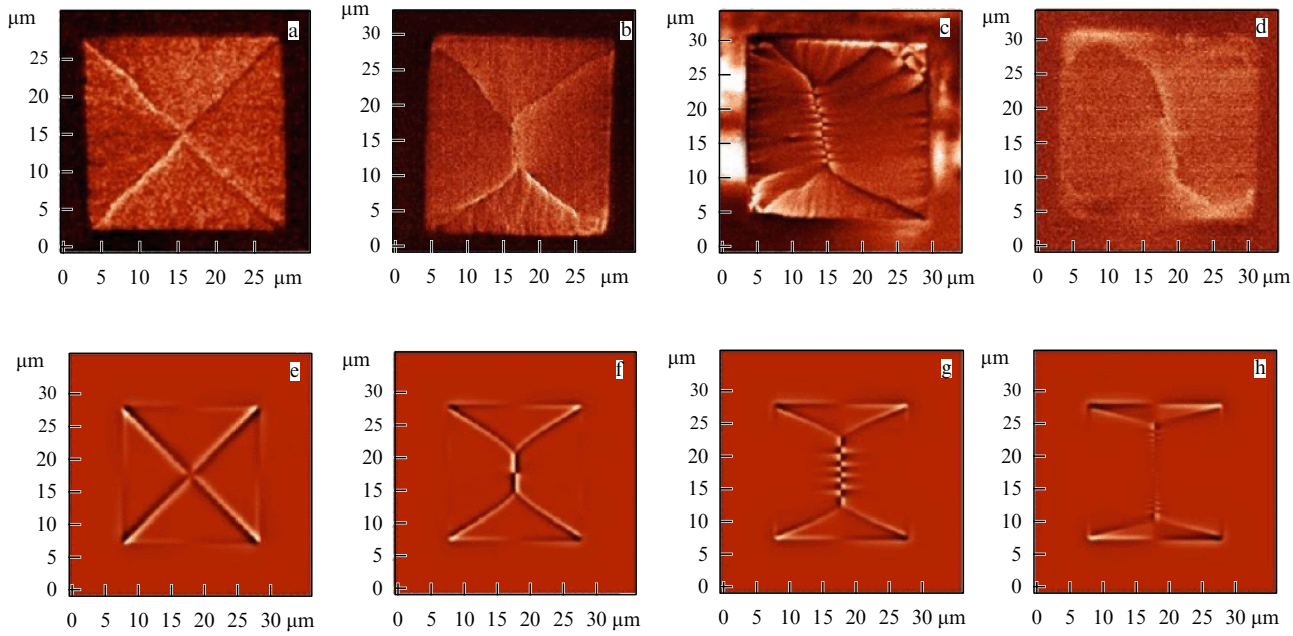

Figure 16. Experimental (a–d) and respective theoretical (e–h) MFM images of 25 × 25-μm Py microparticles from a specimen with the stress gradient along the surface. Model MFM images were obtained at effective anisotropy magnetic field strengths: (e) $H_k = 0.45$ mT, (f) $H_k = 1.12$ mT, (g) $H_k = 2.24$ mT, and (h) $H_k = 4.48$ mT.

particle have recently been registered by the X-ray magnetic circular dichroism (XMCD) technique. Elastic strains in 2×2-μm^2 Ni particles on the lithium niobate surface were induced by SAWs [142].

Reliable compression-induced values H_k can be obtained with the aid of a conventional FMR method only when all the particles are equistressed, i.e., for a type 3 specimen on a substrate bent by its pressing onto a cylindrical surface. The angular dependence of the resonance field permits determining saturation magnetization M_s and effective anisotropy field H_k. The calculation is based on the solution of a set of LLG equations for thin films [133, 139] containing experimentally found minimum and maximum strengths of the resonance field. Azimuthal dependences of FMR spectra of one such sample are represented in Fig. 17. The H_k values obtained were used in an MFM simulation that yielded images coincident with the MFM images in Fig. 16.

The formation of uniaxial magnetic anisotropy in a Py microparticle is also confirmed by measurements of the azimuthal dependence of hysteresis loops made by the MOKE technique [72]. Compression of the microparticles changes coercive force H_c and the M_r/M_s ratio with a 180° periodicity.

For practical applications, *a rearrangement of the micromagnetic structure in real time* is needed. The most natural approach for this purpose takes advantage of using composite ME structures and the principle described in Section 2.1 as an induction of mechanical stresses in a magnetic film by deformation of its piezoelectric substrate. Early research [149–151] demonstrated the possibility, in principle, of rearranging the domain structure under the effect of voltage applied across the piezoelectric substrate. Neither electric nor mechanical impact was localized, and transformation occurred only in selected randomly distributed parts of the domain structure (Fig. 18a).

The motion of individual domain boundaries in magnetic materials can be controlled by localized electric and mechanical impacts using the tip of a scanning microscope, as in single-phase ME materials [152] or the spraying of submicron electrodes [153] (Fig. 18b). Electrodes deposited on a certain area of the piezoelectric substrate (Fig. 18b) play the role of a gate controling the motion of domain boundaries along a magnetic nanowire [153]. A voltage applied to the gate causes the domain boundaries to be pinned in the interelectrode

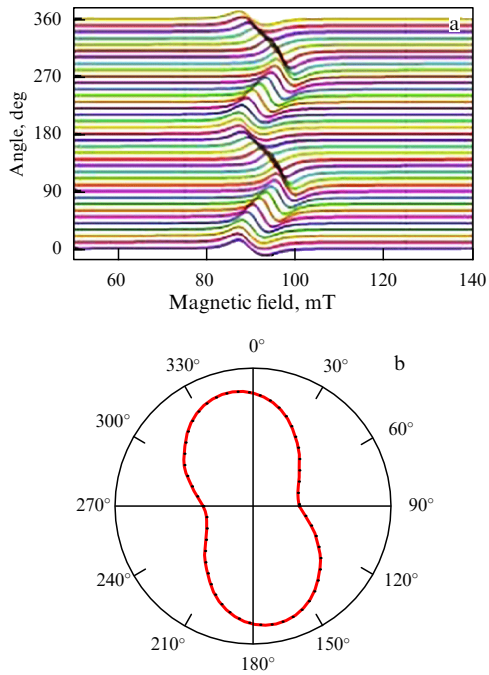

Figure 17. (a) Angular dependence of the resonance line in FMR spectra of compressed Permalloy particles. (b) Azimuthal dependence of the FMR line position in polar coordinates, reflecting the formation of uniaxial magnetoelastic anisotropy in particles.

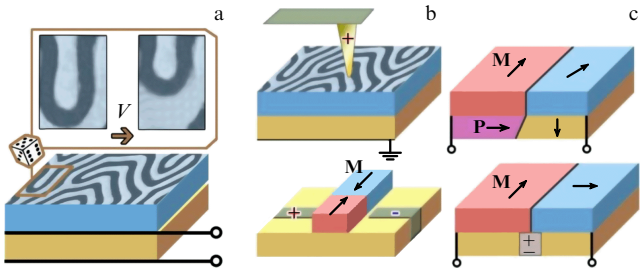

Figure 18. Manipulation of the micromagnetic structure by mechanical stresses: (a) substrate deformation causes real-time rearrangement at random sites of the magnetic structure [149]; (b) manipulation of individual domain boundaries by local mechanical impacts using a scanning microscope probe [43, 152] or preliminarily deposited gate electrode [153]; (c) electrical control of magnetic domain boundaries by their pinning on ferroelectric or polar ferroelastic boundaries [154].

region due to a local change in magnetic anisotropy induced by mechanical stress on the piezosubstrate in the vicinity of the electrodes. The position of the domain boundaries influences the electric resistance of the nanowire, which makes it possible to realize logical devices based on this principle [153].

One more method to localize stress was prompted by Nature and consists in using the substrate domain structure [154–156]. Mechanical stresses arising at the boundaries between ferroelectric or ferroelastic domains of the substrate induce a corresponding distribution of magnetic anisotropy in the overlying ferromagnetic layer. Control of ferroelectric boundaries by an electric field [155, 156] allows moving domain boundaries fixed on them in the magnetic layer (Fig. 18c).

Domain boundaries as interfaces have certain features absent in a crystal in the domain volume, namely possess interrelated ferroelectric, elastic, and magnetic properties [157], providing additional potential for manipulations. For example, an electric field can be applied to control polar domain walls in ferroelastic strontium titanate that, in turn, reorganize the magnetic domain structure by virtue of induced local strains in the overlying magnetic layer [154] (see the lower part of Fig. 18a).

A discussion of the full scope of research in the field of mechanically induced action on the magnetic subsystem of crystals is beyond the framework of the present review. Let us consider below only two examples from the promising area of spintronics concerned with domain boundaries and skyrmions:

• it is proposed to use mechanical stress to stabilize the structure of the moving domain boundary in the magnetoelectric Cr_2O_3 antiferromagnet [153], necessary because the maximum velocity of the antiferromagnetic domain boundary is very low (~ 10 m s^{-1}). In usual magnetic materials, such as ferromagnets, the speed of domain boundaries in fields below the so-called Walker limit [159] increases linearly with the field strength due to the relatively stable boundary structure (turn of magnetization in the boundary plane is the most favorable for magnetostatic considerations). However, this factor does not work in antiferromagnets, where sublattice magnetizations fully compensate for each other. To set the plane of magnetization rotation in the domain wall of an antiferromagnet, the authors of Ref. [158] propose to create artificial anisotropy in the plane of the ME material layer by means of mechanical shear strain, which allows the domain boundary speed to be increased by one order of magnitude (Fig. 19a);

• it is proposed to make use of the local mechanical impact created by the cantilever probe of a scanning microscope for controlled nucleation of single magnetic topological solitons (skyrmions) in the chiral MnSi magnet (Fig. 19b) [160]. A similar scheme has been implemented for the electrically induced generation of magnetic buble domains [161] and skyrmions [162], with the medium being affected by an electric field instead of mechanical stresses. In the case under consideration, however, different mechanisms operate, e.g., either magnetostriction or the Dzyaloshinskii–Moriya interaction modulated by mechanical strains [163]. It was shown in Ref. [160] that mechanical deformation on the order of 10^{-4} (corresponding to a mechanical stress of ~ 10 MPa) removes the energy barrier for the formation of a skyrmion lattice in MnSi. Similar pressure can be produced by a sharp cantilever tip with a radius of curvature of ~ 10 nm to which a force of 100 nN is applied. Because skyrmions are considered candidates for superdense magnetic recording systems, their characteristic of special interest is the energy efficiency in the course of recording. It was estimated in Ref. [160] that the energy losses do not exceed 0.1 aJ, i.e., 3–6 orders of magnitude smaller than in skyrmion-assisted recording with the use of a spin-polarized current.

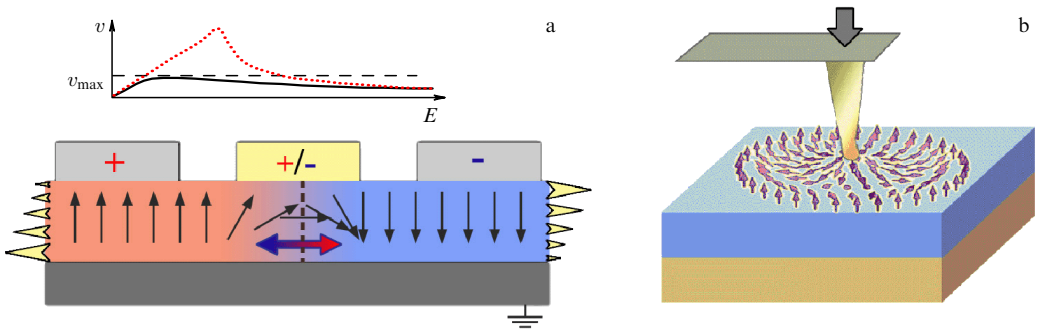

Figure 19. (Color online.) (a) Stabilization of domain boundary structure by shear strain of the magnetoelectric specimen. Shear strain-induced displacements are shown by yellow arrows at specimen butts. The boundary between ME domains moves under the influence of voltage applied across the gate (central electrode): application of potentials positive and negative with respect to ground transfers the boundary to the right and left, respectively. The upper part of the figure shows dependences of domain boundary speed v on electric field strength in the absence of mechanical impact (solid curve) and in the presence of in-plane anisotropy evoked by shear strain (dotted curve); dashed straight line shows the Walker velocity v_{max} [158]. (b) Hypothetical nucleation of a single skyrmion under the effect of mechanical impact by a cantilever tip [160].

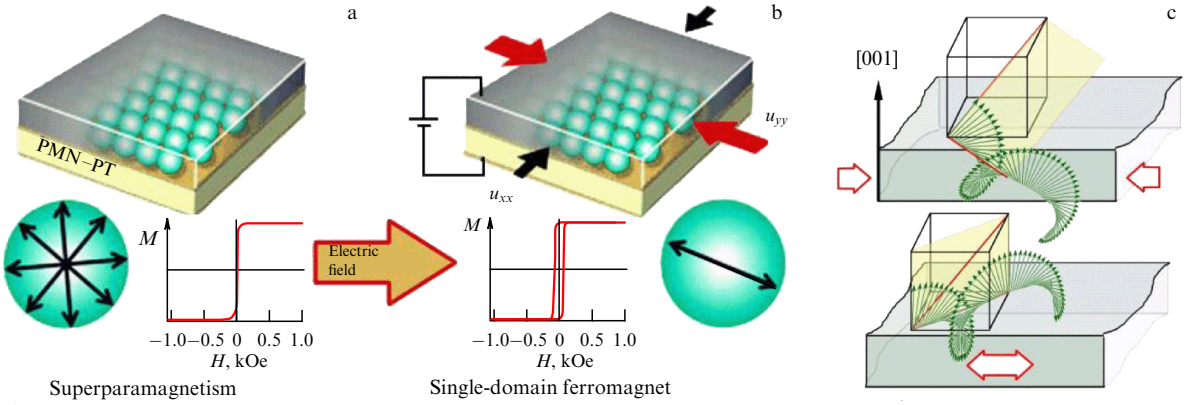

Figure 20. Examples of changes in magnetic states under the action of mechanical stress: transition of Ni nanoparticle from the superparamagnetic state (a) to the ferromagnetic state (b) upon polarization in a 4 kV cm^{-1} electric field [164]. (c) Strain engineering of spin structures in bismuth ferrite films: spin modulation direction and period vary with strain sign [166].

2.3 Stress-evoked magnetic transformations

Mechanical stresses in magnetically ordered substances cause not only rearrangement of the domain structure but also more important changes, such as a temperature shift during transition from a paramagnetic to magnetically ordered state [77]. The paramagnetic behavior can manifest itself at temperatures below the Curie point in magnetic nanoparticles, where the magnetic moment behaves like a giant atomic spin under the influence of thermal fluctuations. It was shown in Ref. [164] that such a *superparamagnetic* state is highly sensitive as well to mechanical deformations. Specifically, particles residing in the superparamagnetic state can be forced into the ferromagnetic state by applying a voltage across the piezoelectric layer harboring them. Their $\sim 0.1\%$ deformation induces in them additional magnetic anisotropy, which results in a 40-K increase in particle blocking temperature corresponding to the lower boundary of the superparamagnetic state, whereas the superparamagnetic magnetization curve (Fig. 20a) turns into a hysteresis loop with a nonzero area (Fig. 20b). The inverse phenomenon produced by mechanical deformations, i.e., the appearance of ferroelectric hysteresis at a temperature below the Curie magnetic point, was observed in superlattices composed of ferromagnetic and ferroelectric perovskites during their transition from the paramagnetic to ferromagnetic state [165].

Films from magnetic materials are intermediate between bulk crystals and nanoparticles. Spin modulation is possible in the film plane, but it can be suppressed owing to the reduced dimension and the presence of epitaxial stresses. This creates prerequisites for a specific form of magnetic phase transformations caused by mechanical strains, namely, transitions from a spatially modulated spin structure to a homogeneous magnetic state. A classic example of the realization of such phase transitions by strain engineering methods is transitions in bismuth ferrite films (Fig. 20c).

Bismuth ferrite $BiFeO_3$, with its relatively simple crystalline structure and a variety of effects observed in it, has remained for almost 10 years one of the most popular subjects of research dealing with magnetoelectric phenomena and multiferroics [167–169]. However, ME properties and the magnetization of bismuth ferrite manifest themselves only upon suppressing its inhomogeneous magnetic structure (the spin cycloid) that takes place, in particular, in strong magnetic fields [167, 170–172]. In this case, magnetic field H directed along the trigonal axis of the crystal serves as a source of efficient easy-plane magnetic anisotropy:

$$K_{u\_\mathrm{eff}} = K_u - \chi_\perp \frac{H^2}{2}\,, \tag{11}$$

where K_u is the uniaxial magnetic anisotropy constant, and $\chi_\perp$ is magnetic susceptibility in the direction perpendicular to sublattice magnetization (in the $\chi_\perp \gg \chi_\parallel$ approximation that holds at temperatures far from the Néel point T_N).

The phase diagram of magnetic states in bismuth ferrite in the magnetic field–magnetic anisotropy coordinates is pre-

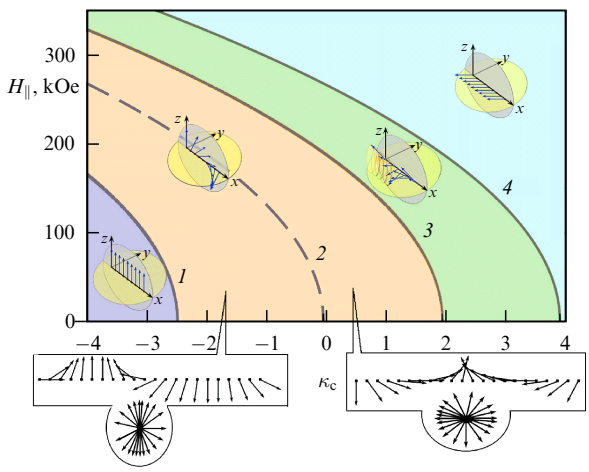

Figure 21. Phase diagram of bismuth ferrite in 'anisotropy constant–magnetic field' coordinates (the anisotropy constant κ_c is opposite in sign with respect to K_u in formula (11) and normalized to the exchage energy of the spin cycloid, the magnetic field is oriented along the principal crystallographic axis: $H \parallel c_3$). Curve *1* — transition from homogeneous antiferromagnetic state with sublattice magnetic moments directed along the principal crystallographic axis into the cycloid phase. Curve *2* — transition from 'easy-axis' anisotropy to 'easy-plane' anisotropy. Curve *3* — second-order transition between easy-plane cycloid and cone cycloid phase. Curve *4* — second-order transition between cone cycloid phase and homogeneous antiferromagnetic phase with 'easy-plane' type anisotropy [173]. Positive and negative degrees of anisotropy κ_c are induced by compressive and tensile strains, respectively. Arrows indicate antiferromagnetic vectors (i.e., sublattice magnetization differences at a given site rather than spins of individual atoms, which means, in particular, that in the cone phase *3* magnetization averaged over the cycloid period remains zero, as in phase *2*.

sented in Fig. 21. It suggests a large variety of magnetic phases, such as homogeneous easy-axis and easy-plane antiferromagnetic structures, as well as heterogeneous states corresponding to incommensurate spatially modulated cycloidal- or conical-type spin structures. Cycloids undergoing anharmonic distortions depending on the sign of anisotropy are, in turn, divided into easy-plane and easy-axis ones (see schematically depicted structures in Fig. 21). The phase transition between cycloids of these two types predicted theoretically in Ref. [174] has been observed in a recent study by means of analysis of temperature-dependent changes in the Mössbauer spectra [175]. The conical phase separating the spin-modulated state in the form of an easy-plane cycloid and the 'easy-plane' type homogeneous state was predicted in Ref. [173] and recently discovered in strong magnetic fields [176].

This great variety of magnetic states is realizable in high strong magnetic fields (10–20 T), of no value for practical applications in electronics. However, the application of strong magnetic fields is by far not the sole method for generating effective magnetic anisotropy; it can be just as well induced by strain engineering techniques in thin films.

Indeed, even the first synthesized bismuth ferrite-based thin films exhibited properties drastically different from those of bulk crystals investigated by earlier authors. These properties included extremely high electric polarization, a pronounced piezoelectric effect, the appearance of magnetization and the linear ME effect [177].

The last two properties related to spin cycloid suppression under the influence of the epitaxial stresses most clearly illustrate the essence of strain engineering for spin structures. Let us consider in greater detail the role of mechanical stresses in the magnetic state of bismuth ferrite-based films.

Even results of their early studies on bismuth ferrite films [178] gave reason to think that the cause of the suppression of the spin cycloid may be attributed to the influence of effective anisotropy described by formula (11) with an additional term proportional to mechanical stresses. However, this effect was impossible to distinguish from another factor (space constraint), film thickness being of the same scale as the spin cycloid period. Moreover, evidence of the existence of intermediate states between the unperturbed cycloid state and the homogeneous state with completely suppressed spatial spin modulation was lacking.

Systematic research on the influence of epitaxial stresses became possible only with the advent of a series of films of exactly the same thickness grown on substrates with different lattice constants: $(LaAlO_3)_{0.3}-(Sr_2AlTaO_6)_{0.7}$ (LSAT), $SrTiO_3$ (STO), $DyScO_3$ (DSO), $GdScO_3$ (GSO), $SmScO_3$ (SSO), $NdScO_3$ (NSO), and $PrScO_3$ (PSO) [166, 179]. Such a wide range of substrates made possible investigations into the properties of bismuth ferrite films exposed to mechanical stresses varying in sign and magnitude, from compressive strains (−2.6% for LSAT) to relative elongations (1% for PSO) (Fig. 22).

Measurements with the aid of a modern Mössbauer precision spectroscopy combined with synchrotron radiation, Raman spectroscopy, and resonant neutron scattering provide information about the magnetic state of bismuth ferrite films, including data on the presence of a spin cycloid, the orientation of its plane, the direction of spin modulation with respect to crystallographic planes, and even anharmonic distortions due to magnetic anisotropy induced by epitaxial stresses.

Figure 23 demonstrates Mössbauer spectra for a series of LSAT–PSO samples. The very apparent difference between the symmetric spectra of the films undergoing strong epitaxial stresses of both signs (LSAT, STO, NSO, PSO) and the asymmetric spectra of weakly stressed films (DSO, GSO, SSO) suggests their qualitatively different magnetic states. Namely, films with asymmetric spectra exhibit cycloidal spin ordering, whereas a spin cycloid in strongly stretched or constricted films is suppressed. A change in the relative intensity of lines *2* and *3* in the Mössbauer spectrum sextet (Figs 23d–f) permits measuring the averaged orientation of the antiferromagnetic vector in both homogeneous and spin-modulated states and thereby determining the orientation of the spin cycloid plane and wave vector **q**. It turned out that extended films exhibit a new type of spin cycloid absent in bulk crystals: its plane is oriented so as to include the normal to the film surface (in the case considered in Ref. [166], this is direction [001]), and the spin modulation direction lies in the film plane, whereas bulk crystals have only structures with orientation of the magnetization rotation plane containing the trigonal axis ([111] in the quasicubic orientation) and the modulation vector perpendicular to this axis.

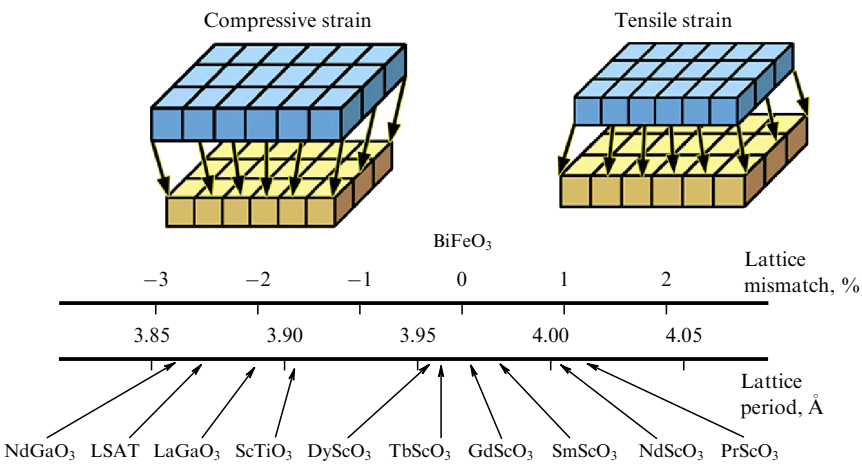

Figure 22. Strain engineering of bismuth ferrite films. The use of substrates made from different perovskites of a general formula ABO_3 permits varying the degree of relative deformation in the −3% to +1% range [166].

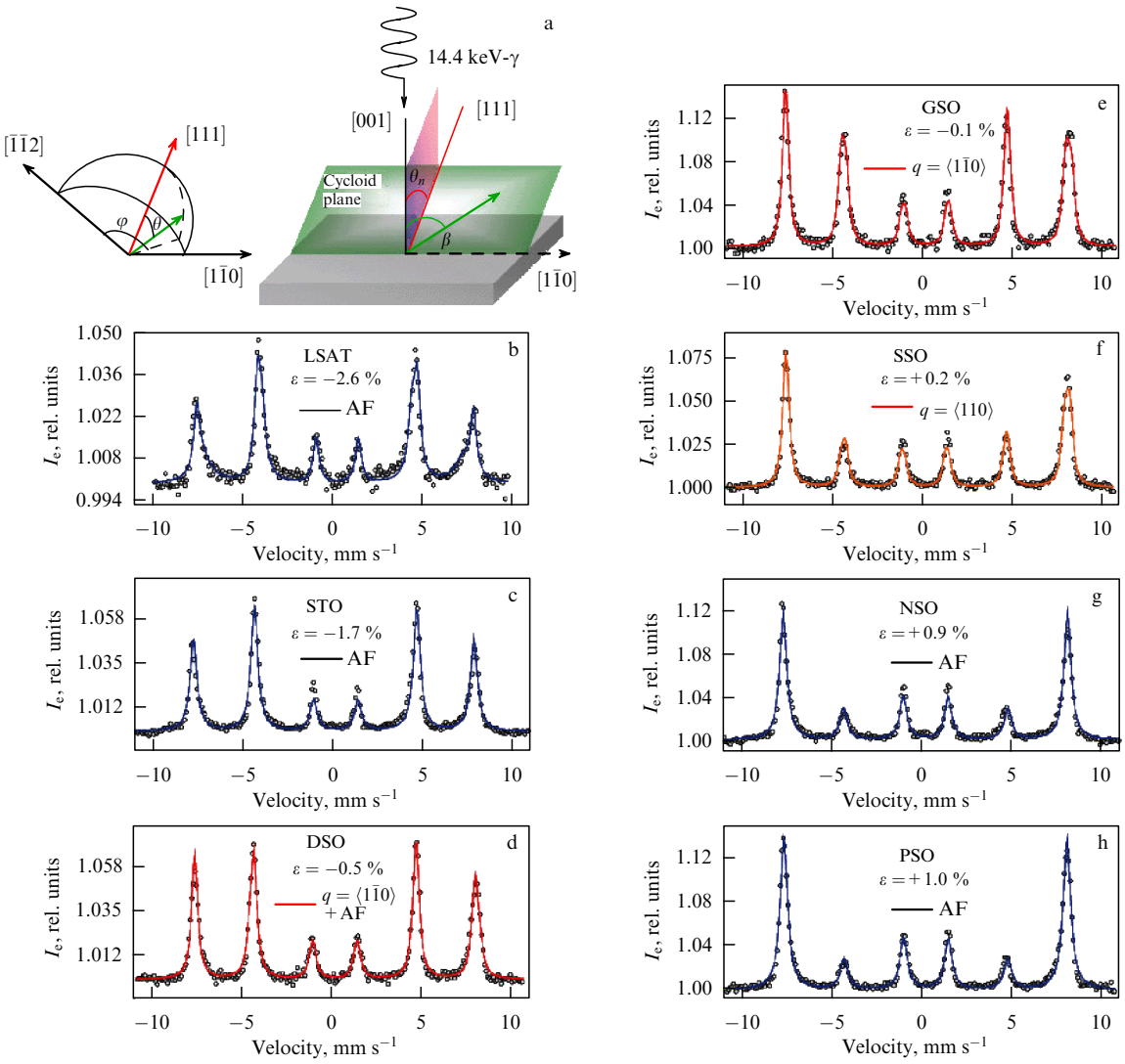

Figure 23. (Color online.) Mössbauer spectra of hyperfine interaction between ^{57}Fe nuclei and their electronic environment in bismuth ferrite (001) films with various epitaxial stresses. (a) Geometry of experiment. (b–h) Spectra measured at 295 K. I_e — radiation intensity of conversion electrons. Dots — experimental data, curves — approximations based on magnetic state models: homogeneous antiferromagnetic (AF) ordering (b, c, g, h), cycloid states similar to bulk crystalline state (d, e), and cycloid with propagation direction [110] existing only in stretched films (f) [166].

One more precision measuring technique, resonant scattering of polarized neutrons on the ^{57}Fe-enriched samples, yields additional information about the magnetic structure of bismuth ferrite films, allowing the reconstruction of the spin configuration in thin films (Fig. 24). The validity of theoretical models used to approximate Mössbauer spectra is confirmed by resonant neutron scattering data; namely, a cycloid characteristic of bulk crystals occurs in films undergoing compression from the substrate side, whereas the spin cycloid of a new type running in direction [110] appears in stretched films. Strong compressive and tensile strains cause a transition to the homogeneous antiferromagnetic state with easy-plane and easy-axis anisotropies, respectively.

Arguably, the most striking evidence of the presence of a cycloid in some films and its suppression in others is Raman spectra patterns. In a homogeneous state with a suppressed cycloid there are only two modes corresponding to parallel and crossed orientations of the analyzer and the polarizer (Figs 25a, e, f), whereas spin modulation gives rise to many peaks (Figs 25b–d). The point is that a film with a spin cycloid can be regarded as a magnon crystal in which the Brillouin zone is bounded by π/λ, where λ is the cycloid period. This leads to occurring a system of allowed and forbidden bands and, as a consequence, a series of Raman spectrum lines corresponding to transitions between the states separated by these bands.

Interestingly, the structure of emerging bands depends on both mechanical stresses and magnetic field. The simultaneous influence of these two factors on the spin cycloid was investigated in Ref. [179]. It turned out that epitaxial stresses markedly reduce the critical magnetic field at which the spin cycloid is suppressed. Figure 26a presents the phase diagram of the magnetic structure of a bismuth ferrite film in the magnetic field–relative deformation coordinates, taking account of Raman spectroscopy and resonant scattering data of polarized neutrons, as well as results of calculations. Even for weakly stressed films on a GSO substrate, the critical field is reduced to 8 T, in contrast to 20 T in bulk bismuth ferrite crystals.

This can be explained taking into consideration the following factors: (1) finite size effects in thin films, which manifest themselves even in the absence of mismatch between

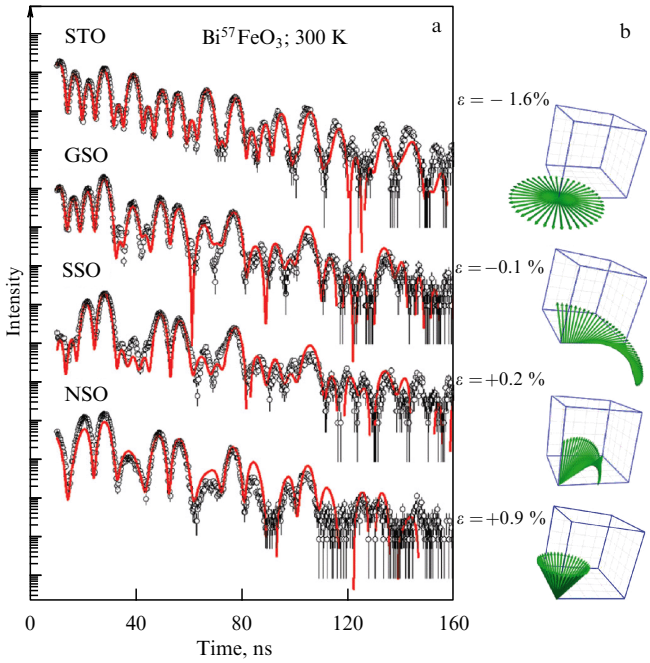

Figure 24. Nuclear time spectra for resonant scattering of synchrotron radiation in $Bi^{57}FeO_3$ thin films at room temperature: (a) beat pattern for films grown on STO, GSO, SSO, and NSO substrates with crystallographic (001) orientation; (b) schematic of a spin structure in bismuth ferrite films reconstructed from the data in figure (a). *NB*: To avoid misunderstandings in interpreting the images of spin structure in bismuth ferrite films on STO and NSO substrates, it should be borne in mind that they depict neither speromagnetic nor conical structures but reflect only the fact that real specimens are multidomain entities with different directions of the antiferromagnetic vector in individual domains [179].

the lattice constants of the substrate and the sample; (2) enhanced magnetoelastic properties in the thin-film phase, and (3) the difference between the spin cycloid present in thin films and the structure realized in bulk crystals. Indeed, the spin cycloid in thin films is characterized by enhanced susceptibility to external inputs; it undergoes anharmonic distortions, including changes of shape (see Fig. 21) and period, especially noticeable for stresses and magnetic fields close to the critical ones. Figure 26b shows the dependence of the spin cycloid period on the magnetic field strength deduced from results of Raman spectroscopy with the imposed theoretical curve tending toward infinity when the field approximates the critical value.

It follows from the above that a systematic research with the use of the bismuth ferrite films of the same thickness differing only in the magnitude of epitaxial stresses has revealed new intermediate phases separating unperturbed cycloidal and homogeneous antiferromagnetic states. In addition, the possibility of manipulating spin structures by mechanical stresses and magnetic field has been demonstrated, which can be used in magnon and spintronic devices:

• the spin cycloid in a bismuth ferrite film constitutes a magnon crystal with a period given by epitaxial stress in the film and additionally adjusted by the magnetic field;

• the rearrangement of the spin cycloid by mechanical stresses is possible in spintronic devices, too: spin reorientation from the film plane direction toward that orthogonal to it upon a change in the strain sign (see Fig. 24) allows altering the magnetoresistance of a many-layer structure based on bismuth ferrite and ferromagnetic layers coupled to it through an exchange interaction [166];

• states with differently directed spin cycloid planes, switching between which is effected by the application of

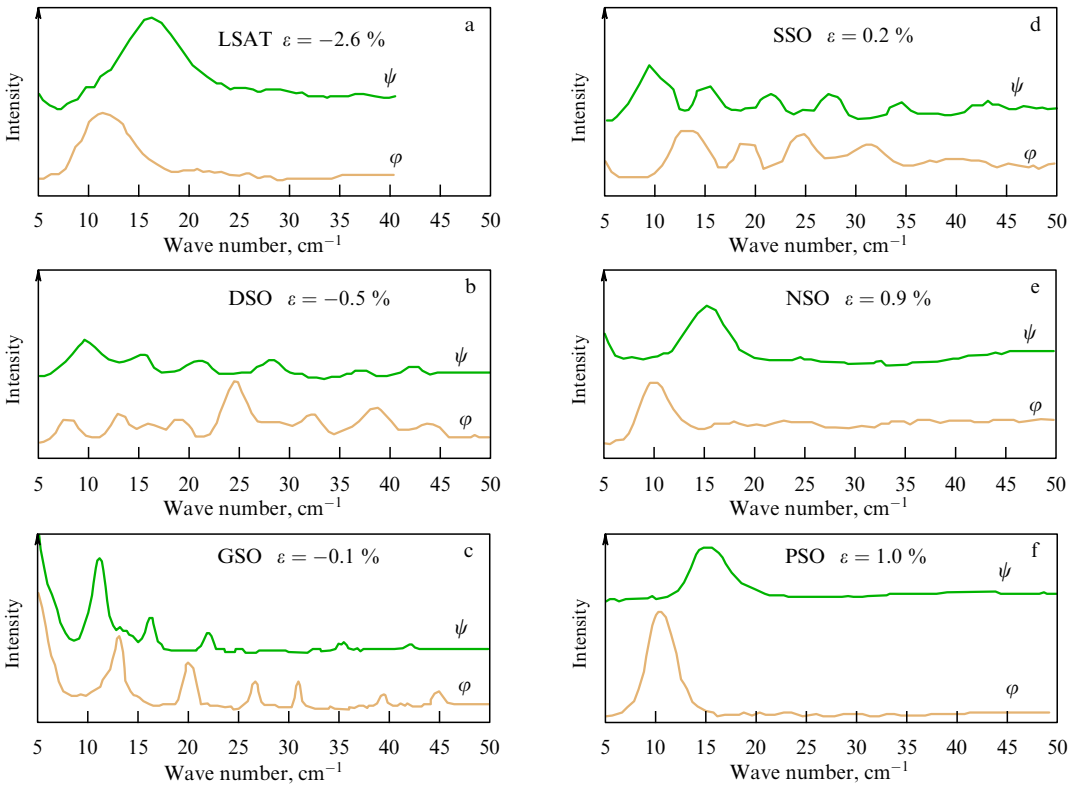

Figure 25. Low-energy Raman spectra of bismuth ferrite films grown on different substrates: φ and ψ modes shown by light (orange) and dark (green) curves, respectively, correspond to parallel and crossed orientations of polarizers [166].

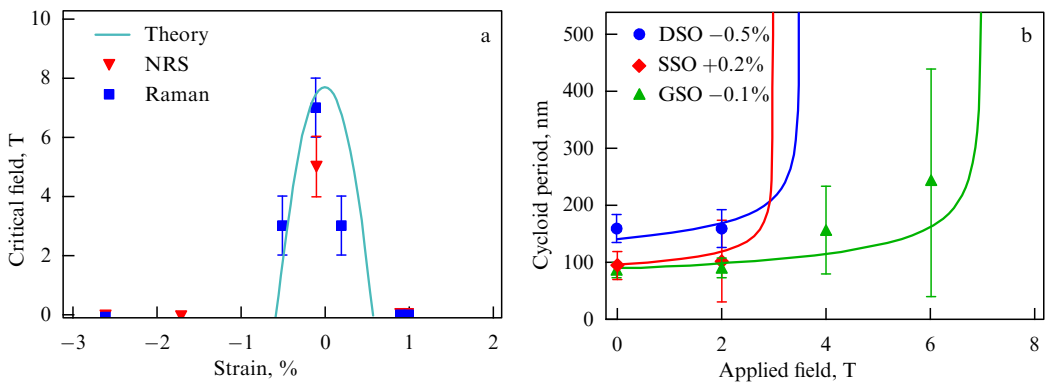

Figure 26. Influence of a magnetic field on the spin cycloid in bismuth ferrite films with crystallographic orientation (001). (a) Phase diagram in a 'magnetic field–relative deformation' axes. Solid curve corresponds to calculated phase boundary between spin cycloid and collinear ordering. Triangles and squares represent experimental data obtained by the nuclear resonant scattering (NRS) method and Raman spectroscopy. (b) Dependence of spin cycloid period on the magnetic field. Different symbols correspond to experimental data for three samples. Solid lines are theoretical curves showing the tendency toward an infinite increase in the period in the critical magnetic field [179].

mechanical stresses (see Fig. 20c), can be regarded as logical states in magnetic memory devices with electric recording.

The giant enhancement of the ME effect in bismuth ferrite films [177, 180] deserves special research. One hypothesis attributes this phenomenon to the heightened susceptibility of a special type of perovskite-lattice structure distortions (antiferrodistortions) to an electric field due to the influence of epitaxial tensions. Antiferrodistortion is defined as the turn of neighboring oxygen octahedrons in opposite directions, which is responsible for weak ferromagnetism. The electric field changes octahedron turn angle and thereby the magnetization conditioned by a weak ferromagnetism, thus making an additional contribution to the ME effect [181].

Epitaxial stresses in bismuth ferrite films are also responsible for the co-existence of two phases with distortions of different types in the initial perovskite structure, including rhombohedral and tetragonal [182]. An enormously large relative deformation gradient ($\sim 3\times 10^7\ \mathrm{m}^{-1}$) emerges at the interface between these phases, which gives rise to an unusual mechanism of ME interactions due to the joint action of flexoelectric and flexomagnetic effects (see Section 1.2): an electric field causes boundary re-orientation of the perovskite phases that, in turn, changes the direction of the antiferromagnetic vector [34]. Since the rhombohedral and tetragonal phases differ in terms of structural, magnetic, and optical properties, the electric field switching them heightens piezoelectric [183], magnetoelectric [182], and electro-optic [184] effects in the crystal.

Strain engineering techniques are successfully employed to manipulate the properties of other perovskite-based multiferroics, such as $R\mathrm{MnO}_3$ systems, where R is a rare-earth element [78, 185–188]. A detailed description of research efforts on materials of this class is beyond the scope of the present review; it can be found in special reviews [71, 78, 185, 188]. But it is worth highlighting the research results on the transition from an antiferromagnetic state to a ferromagnetic one induced by epitaxial stress in LuMnO_3 films [187].

2.4 Thermally induced magnetoelastic effect

One more approach to manipulating magnetization in films and particles is based on the difference between thermal expansion coefficients of the magnetic layer and the substrate, or on the phase rearrangement of the substrate crystallographic structure under heating. Elucidation of the mechanisms underlying the thermally induced magnetoelastic effect in heterostructures not only provides a deeper insight into the nature of this phenomenon, but also opens up prospects for combining different methods of magnetization control in straintronic devices.

One of the structures to demonstrate the thermally induced magnetoelastic effect is porous anodized aluminum. Its surface, prepared under specific anodic oxidation regimes, is formed of close packed extended vertical channels of aluminum oxide [189–193]. These channels can be filled with ferromagnetic metals by means of electrochemical deposition (Fig. 27a). Thermal expansion coefficients of aluminum base, nickel, and aluminum oxide differ approximately twofold ($23.8\times 10^{-6}\ \mathrm{K}^{-1}$ in Al, $13.0\times 10^{-6}\ \mathrm{K}^{-1}$ in

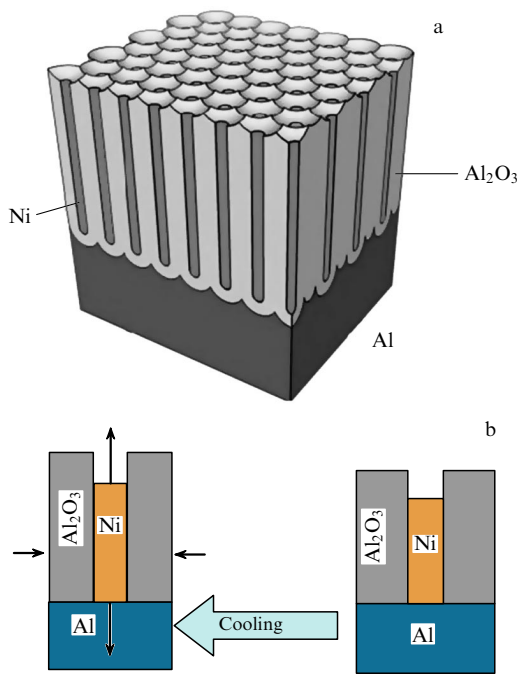

Figure 27. Stress formation in Ni nanowires: (a) schematic representation of nanowires in pores of anodized aluminum, and (b) deformation of a nanowire by aluminum substrate compression during cooling of the sample.

Ni, and 6×10^{-6} K^{-1} in Al_2O_3). This difference accounts for stresses in nanowires induced by the compression of aluminum and aluminum oxide upon a drop in sample temperature (Fig. 27b) [189]. This leads to the formation of the magnetoelastic anisotropy field that tends to turn magnetic moments in the wire in the direction perpendicular to its axis, i.e., it competes with the shape anisotropy field responsible for orientation of local magnetic moments along the wire. As a result, an anomalous peak appears on the temperature dependence of coercive force $H_c(T)$, corresponding to the maximum of effective anisotropy field $H_a(T)$ in the temperature range close to room temperature [190]. Similar thermally induced magnetoelastic effects were reported in Refs [191, 192].

Another way to induce the magnetoelastic anisotropy field in ferromagnetic films or particles is to use crystals undergoing structural phase transitions during their heating or cooling as substrates. One such crystal is barium titanate $BaTiO_3$, in which the crystal lattice transforms from tetragonal system into orthorhombic and then rhombohedral upon cooling to below room temperature [194–196]. The transformation is accompanied by a change in the size of the crystallographic cell on the $BaTiO_3$ surface. Rearrangement of atomic positions in the surface layer during phase transitions in $BaTiO_3$ crystals induces elastic stresses in the ferromagnetic metal deposited on the crystal surface. For example, stepwise changes of magnetization are observed in isolated 30-nm thick elongated Fe microparticles on the $BaTiO_3$ (001) surface during the above-mentioned phase transitions [194, 196]. X-ray diffraction studies revealed a 0.035% relative change in the crystallographic cell size in Fe particles, associated with a drop in the sample temperature from 300 to 150 K. MFM results suggest that the magnetoelastic anisotropy field induced by a temperature change is sufficient to rearrange the many-domain magnetization structure of the particles on the $BaTiO_3$ surface into a single-domain structure with magnetization oriented parallel to the particles' long axis [195]. Similar experiments on 10-nm thick Fe films on the $BaTiO_3$ (100) surface demonstrated a 120% change in coercivity due to a magnetoelastic effect induced by phase rearrangement of the substrate crystal lattice [195].

In situ rearrangement of the domain structure was observed in an 80-nm thick $CoFe_2O_4$ film on a $BaTiO_3$ substrate with crystallographic orientation (001) at the instant of phase transition of the substrate crystalline surface. Such experiments were carried out using a low-temperature magnetic-force microscope operating in a temperature range from 150 to 360 K. Heating the crystal during phase transition changed the symmetry of its crystallographic cells from rhombohedral to orthorhombic, and then tetragonal and cubic (at 188, 280, and 398 K, respectively). A mismatch between $BaTiO_3$ and $CoFe_2O_4$ lattice constants resulted in arising magnetoelastic stresses in the latter compound that caused displacement of domain walls and altered both the size of magnetic domains and the orientation of magnetization in these domains registered by MFM. Importantly, these changes occurred at the same temperatures as stepwise variations of macroscopic magnetization in these specimens recorded by a SQUID magnetometer [197]. This suggests that a heterostructure from a ferromagnetic metal on the $BaTiO_3$ surface can be regarded as a candidate for domain magnetic structure control by substrate phase transformations.

Other materials in which structural phase transitions can be used to form magnetoelastic anisotropy fields are exemplified by vanadium oxides (VO_2 and V_2O_3). In VO_2, the structural phase transition of the first kind from monoclinic to tetragonal symmetry of the lattice occurs on heating up to temperatures above 340 K, i.e, slightly higher than room temperature [198, 199]. The relative size of a unit cell in the process decreases along one axis but increases along two others [200]. The phase transition in VO_2 induces a magnetoelastic anisotropy field in an Ni film, under the effect of which H_c decreases from 236 Oe (at 320 K) to 88 Oe (at 350 K) [200]. Such a considerable reduction in H_c in response to gentle heating slightly above room temperature opens up prospects for using this effect in developing heat-assisted magnetic recording (HAMR) techniques. An analogous effect was documented in 10-nm thick Ni films on a V_2O_3 substrate, but only at much lower temperatures: 100–250 K [201].

Special attention is currently given to tensile materials in connection with the development of stretchable electronics, which enables embedding microcircuits into clothing and also using them in carrying devices. One such material for straintronics may be polyvinylidene fluoride (PVDF), a ferroelectric polymer composed of carbon chains that contain alternating CH_2 and CF_2 groups. The β-phase of PVDF is based on quasihexagonal packing of parallel long carbon chains (Fig. 28a) [202]. PVDF with a high β-phase content is characterized by a large negative anisotropic thermal expansion coefficient ($\alpha_1 = -13 \times 10^{-6}$ K^{-1} and $\alpha_2 = -145 \times 10^{-6}$ K^{-1}), besides the piezoelectric effect [203]. This means that heating the PVDF film-based substrate causes its greater compression along the y-direction (normal to carbon chains) than along the parallel x-direction (Fig. 28a). Due to the anisotropic thermal expansion coefficient of the substrate, heterostructures with ferromagnetic nanofilms ($Fe_{81}Ga_{19}$, $Co_{40}Fe_{40}B_{20}$, Ni) on a PVDF film-based substrate exhibit unusual magnetoelastic properties [204, 205]. Studies of the azimuthal dependence of hysteresis loops with a SQUID magnetometer showed that the ratio M_r/M_s of residual-to-saturation magnetization is practically unrelated to the rotation angle ϕ in the sample plane at a given temperature of the sample (Fig. 28c), suggesting the absence of magnetic anisotropy in the film. In particular, for 60-nm thick $Co_{40}Fe_{40}B_{20}$ on a 30-μm thick PVDF film, this temperature is 298 K. As it falls below 298 K, an easy magnetization axis forms in the film along the y-axis, and the azimuthal dependence of M_r/M_s takes on a figure-eight shape (see inset to the left part of Fig. 28c). As temperature rises to above 298 K, substrate compression along the y-axis prevails and uniaxial anisotropy forms along the x-axis (see inset to the right part of Fig. 28c), while the 'figure eight' is turned through 90°. The change in the M_r/M_s ratio in the temperature range from 250 to 350 K shown in Fig. 28c perfectly well reflects the accompanying 90° turn of anisotropy.

The anomalous behavior of the effective magnetoelastic anisotropy constant ($K_{eff} = M_s H_k/2$, where H_k is the effective anisotropy field) in the above ferromagnetic films with increasing temperature of the PVDF substrate deserves special mention. Usually, constant K_{eff} is negative due to a substantial reduction in the saturation magnetization with growing temperature (which, by the way, impedes reliable storage of magnetic information at the elevated temperature of the magnetic storage medium). In the case being considered, H_k increases with increasing temperature so quickly that K_{eff} becomes positive. This was demonstrated in Ref. [204] by

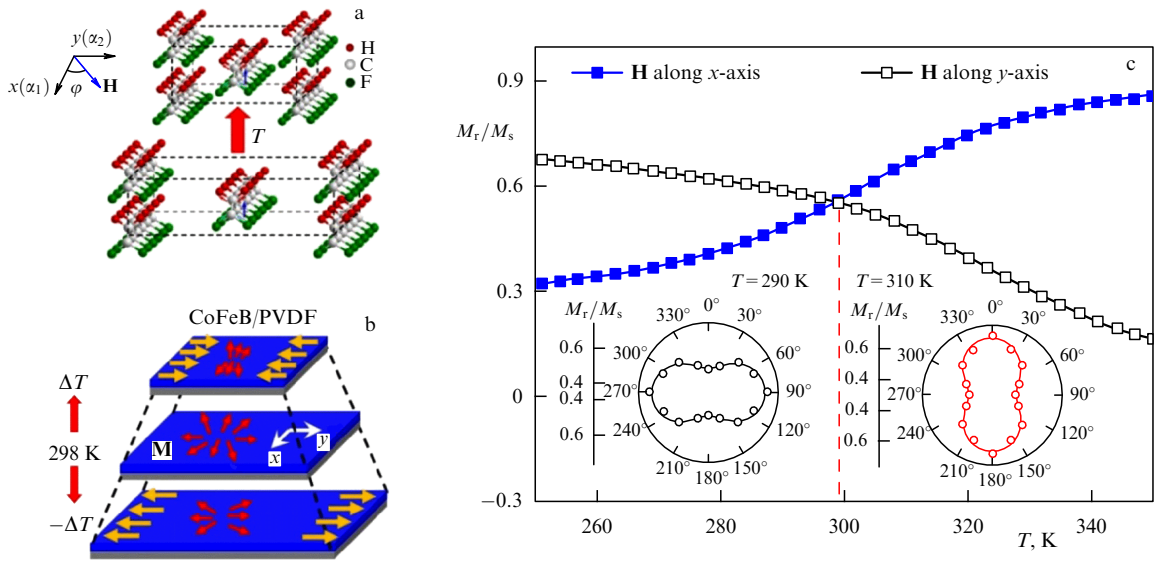

Figure 28. (a) Schematic of a change in PVDF molecular structure with rising temperature. (b) Schematic of rearrangement of magnetization structure in $Co_{40}Fe_{40}B_{20}$ film with varying substrate temperature. (c) A change in M_r/M_s with rising temperature at field orientation along the x-axis (dark squares) and y-axis (light squares). Insets: azimuthal dependences of M_r/M_s ratio reflecting formation of magnetic anisotropy along the x-axis (left) and y-axis (right) at varying temperature. (Adapted figure from Ref. [204] by courtesy of the authors.)

measuring the azimuthal dependence of FMR spectra in the 200–300 K range. A rise in temperature caused a shift of the FMR resonance line to the region of higher or lower fields, depending on the orientation of the external field of the spectrometer along the hard or easy magnetic axis, respectively, in the ferromagnetic film. To determine H_k at different temperatures, calculations based on the FMR resonance line position in the FMR spectrum were undertaken, by analogy with the method employed earlier to study transformations of FMR spectra in Permalloy films in which magnetoelastic anisotropy was mechanically induced [133, 139]. It turned out that heating $Co_{40}Fe_{40}B_{20}$/PVDF structure increases H_k from 160 Oe at 290 K to 260 Oe at 350 K, i.e., greater than the saturation magnetization falloff in the same temperature range; therefore, K_{eff} is positive in such a structure.

Because PVDF offers piezoelectric properties, nanofilm magnetization anisotropy can be controlled by the simultaneous application of an electric field and heat supply to the heterostructure [205]. To this end, a PVDF substrate is coated on both sides first with an aluminum film playing the role of electrodes, and then with an evaporated ferromagnetic metal. It proved possible to turn film magnetization through 180° in $Fe_{81}Ga_{19}$ films deposited on a PVDF substrate by varying the temperature from 320 to 280 K and back in the presence of a weak 20-Oe field (weaker than the film coercive field). After reversal of the magnetic field and repetition of the cooling–heating cycle, film magnetization returned to its previous position [205].

It is worth mentioning effects of optical irradiation in connection with the thermal impact on the elastic subsystem. Optical radiation can give rise to both thermally induced and photoinduced effects related to the transfer of photoexcited electrons and holes in ferroelectrics [206] and multiferroics [9, 51]. A detailed study in this field is reported in a review published in *Physics-Uspekhi* [206]. By way of illustration of light-induced dynamic effects, the optical recording of the periodic structure of mechanical stresses in ferroelectrics and its photoinduced excitation by SAWs [207] can be mentioned [207], together with the recently demonstrated possibility of switching mechanical stresses in the multiferroic bismuth ferrite with giga- and terahertz frequencies [52], which opens up new prospects for straintronic research in the high-frequency region.

2.5 Field transformation in composite structures

The linkage between the magnetic and electric parameters of composite structures via strain at the interface accounts for the generation by the structure of an electric field E in the external magnetic field H (direct ME effect characterized by linear transformation coefficient α_E) or a change in the structure magnetization M by the electric field E (converse ME effect characterized by linear transformation coefficient α_M). In recent decades, these effects have been discovered in composite structures containing various combinations of ferromagnetic (FM) and piezoelectric (PE) materials (see Table 2).

As a rule, the direct ME effect is observed in a dynamic regime when an alternating magnetic field $\delta H(t)$ with frequency f is applied to the composite and the alternating electric field $\delta E(t)$ generated by the PE layer is registered. It has been shown that the efficiency $\alpha_E = \delta E/\delta H$ of direct ME conversion of the fields at frequencies far from the structure acoustic resonances can vary between $\alpha_E \sim 0.1$ V cm^{-1} Oe^{-1} and ~ 50 V cm^{-1} Oe^{-1}, depending on the composition, i.e., it is one or two orders of magnitude greater than the efficiency of ME conversion in single-phase multiferroics. To reach the maximum α_E value, it is necessary to use FM layers with large piezomagnetic modulus $\lambda^{(1)}$, i.e., quite large magnetostriction λ_s and low saturation fields H_s (e.g., Metglas-like alloys [3]), and PE layers of materials with a large ratio of piezoelectric modulus-to-dielectric constant (d/ε), such as fiber-based PZT- or PMN–PT piezocomposites [208], crystals of langatate [209], aluminum nitride [210] and quartz [211], and

[3] Metglas is a thin tape of amorphous metal alloy formed by fast (roughly 10^6 K s^{-1}) solidification.

PVDF type piezopolymers [212, 213]. Under acoustic resonance conditions, transformation efficiency increases in proportion to the acoustic Q-factor of the structure. Structures containing PE layers from crystals with small acoustic losses and thin FM layers introducing small acoustic attenuation should be preferred. An enormously high ME-coefficient $\alpha_E = 20\,\mathrm{kV\ cm^{-1}\,Oe^{-1}}$ was obtained under the resonance conditions for a thin-film FeCoSiB – AlN structure on a silicon substrate oscillating in a vacuum [214].

The converse ME effect is also observed in the dynamic regime with the application of a small-amplitude alternating electric field $\delta E(t)$ to the piezoelectric layer of the structure and registering a change in magnetization $\delta M(t)$ in the FM layer of the structure by the electromagnetic coil. The efficiency of inverse transformation $\alpha_M = \delta M/\delta E$ grows resonantly when the electric field frequency coincides with the frequency of acoustic eigenmodes of the structure. Typical values of the converse ME conversion coefficient for structures of various compositions fall within the $\alpha_M = 0.1-10\ \mathrm{G\ cm\ V^{-1}}$ range. The most pronounced converse ME effect was documented in a structure containing a piezofiber converter between two Metglas layers. The transformation coefficient reached $\alpha_M = 80\ \mathrm{G\ cm\ V^{-1}}$ at a structure resonance frequency of 30 kHz [215].

It was shown that the efficiencies of direct and converse ME transformations in the same structure at far-from-resonance frequencies are related by the expression $\alpha_E = \alpha_M$ (in the CGS system) [216]. Under resonance conditions, the relationship between conversion coefficients of direct and converse ME effects is more complicated. In the same H and E fields, the direct ME effect is observed at the antiresonance frequency f_a, whereas the inverse effect occurs at the resonance frequency f_r. These frequencies are close to each other but not equal. The efficiencies of direct and inverse resonant ME effects are different, too.

Let us consider in greater detail the field transformation in the case of the direct ME effect taking into account the nonlinearity of magnetostriction. Voltage U generated in the structure by an alternating magnetic field can be determined based on the layer properties combination principle [28]. Let a ferrromagnetic/piezoelectric structure be placed in a tangential low-frequency excitation magnetic field H and a parallel constant field H_0: $H(t) = H_0 + h\cos(2\pi ft)$. The ferromagnetic layer of this structure undergoes magnetostrictive strain $\lambda(H)$ along the field, while the piezoelectric layer with piezomodulus d_{31} converts this strain into voltage U expressed as [217]

$$U(H) = Bd_{31}\lambda(H)\,, \tag{12}$$

where B is the constant coefficient depending on dielectric and mechanical parameters, and the size of the layers. Taylor's series expansion of nonlinear strain $\lambda(H)$ near H_0 on condition $h \ll H_0$ leads to

$$\lambda(H) = \lambda(H_0) + \sum_{n=1}^{\infty} \frac{1}{n!}\,\lambda^{(n)}\left[h\cos(2\pi ft)\right]^n\,, \tag{13}$$

where $\lambda^{(n)} = \partial^n\lambda/\partial H^n|_{H_0}$ is the nth-order derivative of magnetostriction over the field at $H = H_0$.

Substituting Eqn (13) into (12), while taking account only of terms up to the third-order infinitesimal, yields

$$U = U_0 + U_1\cos(2\pi ft) + U_2\cos(4\pi ft) + U_3\cos(6\pi ft) + \ldots\,. \tag{14}$$

Constant voltage in Eqn (14) has the form

$$U_0 = Bd_{31}\left(\lambda(H) + \frac{\lambda^{(2)}h^2}{4}\right), \tag{15a}$$

and the amplitudes of harmonics with frequencies nf are as follows:

$$U_1 = Bd_{31}\lambda^{(1)}h\,, \tag{15b}$$

$$U_2 = Bd_{31}\,\frac{\lambda^{(2)}h^2}{4}\,, \tag{15c}$$

$$U_3 = Bd_{31}\,\frac{\lambda^{(3)}h^3}{24}\,. \tag{15d}$$

Constant voltage (15a) across electrodes rapidly decreases due to the finite conductivity of the PE layer. It follows from expressions (15b)–(15d) that amplitudes of the nth-order voltage harmonics are proportional to the nth-order derivatives $\lambda^{(n)}$ of magnetostriction over field H; they increase in a power-law manner with the growth in alternating pump field h.

Figure 29 shows, by way of example confirming the theory, typical ME characteristics of a two-layer Metglas–langatate structure at small and large amplitudes of the exciting field h. Figures 29a, c plot amplitude–frequency characteristics of the structure, i.e., the dependence of voltage U generated by the structure under sweeping the frequency f of the field. Figures 29b, d display frequency spectra of the voltage generated by the structure at the fixed pump field frequency $f_1 = 1$ kHz. Figure 29a demonstrates a voltage peak near the frequency $f_0 = 4.7$ kHz at the small field amplitude $h = 0.1$ Oe, suggesting an 'enhancement' of the effect due to the resonant growth of strains at the bending vibration frequency f_0 of the structure [218, 219]. Off-resonance ME coefficient is $\alpha_E = 0.15\ \mathrm{V\ cm^{-1}\,Oe^{-1}}$; it increases at the resonance frequency by $Q \sim 800$ times (Q is the quality factor) and amounts to $\alpha_E \sim 120\ \mathrm{V\,cm^{-1}\,Oe^{-1}}$. In the weak excitation regime, the voltage frequency spectrum contains a single component with frequency f_1 (Fig. 29b) equal to the pump field frequency.

A rise in the alternating field amplitude to $h = 4.5$ Oe is associated with the pronounced nonlinearity of magnetostrictive strain in the structure, which radically changes the picture [217, 220]. The amplitude–frequency characteristic $U(f)$ acquires additional peaks with frequencies f_0/n (Fig. 29c), and the frequency spectrum shows harmonics with multiple frequencies $f_1 n$ (Fig. 29d). The amplitudes of the harmonics increase in a power-law manner as field h grows. They can be changed by constant field H, because their height is defined by the form of field dependence of respective derivatives $\lambda^{(n)}(H)$. Specifically, the first harmonic U_1 increases linearly with H; it reaches the maximum value at a certain field H_m, but decreases thereafter. The second harmonic U_2 reaches a maximum in the absence of the bias field at $H = 0$ and vanishes roughly at the same field H_m.

Excitation of a structure by two fields, $h_1\cos(2\pi f_1 t)$ and $h_2\cos(2\pi f_2 t)$, produces an effect of resonant mixing of the magnetic fields [221], and the structure generates voltage at difference and summary frequencies $f_1 \pm f_2$. Figure 30 plots amplitude–frequency characteristics of a PZT–Metglas structure upon a change in the frequency f_1 of the first field, and different fixed frequencies f_2 of the second one. Peaks on the curves correspond to the resonance condition $|f_1 \pm f_2| = f_0$, where $f_0 = 0.7$ kHz is the frequency of structure bending

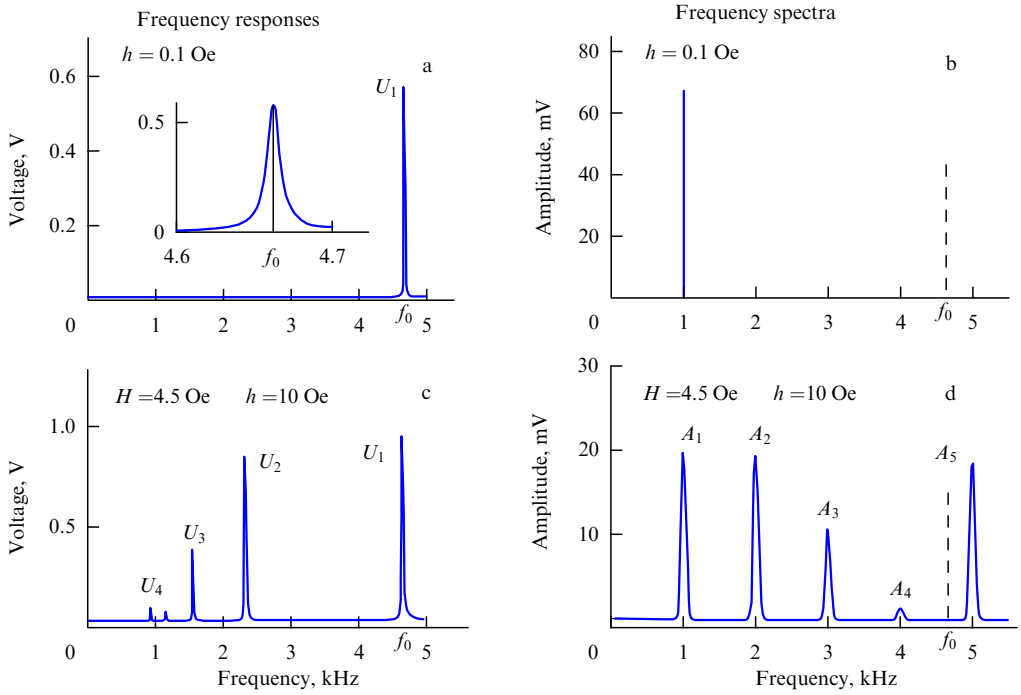

Figure 29. Amplitude–frequency characteristics (a, c) and frequency spectra (b, d) of ME voltage in Metglas–langatate structure at amplitudes $h = 0.1$ Oe (a, b) and $h = 10$ Oe (c, d) of a pumping magnetic field and $H = 4.5$ Oe.

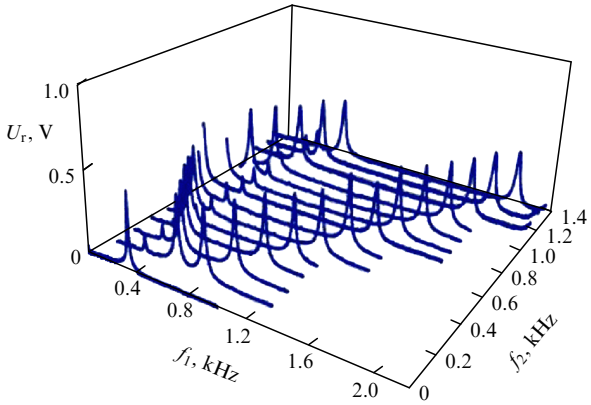

Figure 30. Nonlinear mixing of magnetic fields with f_1 and f_2 frequencies in a PZT–Metglas composite structure at fields $h_1 = h_2 = 2$ Oe and $H = 0$. Structure bending vibration frequency $f_0 = 0.7$ kHz.

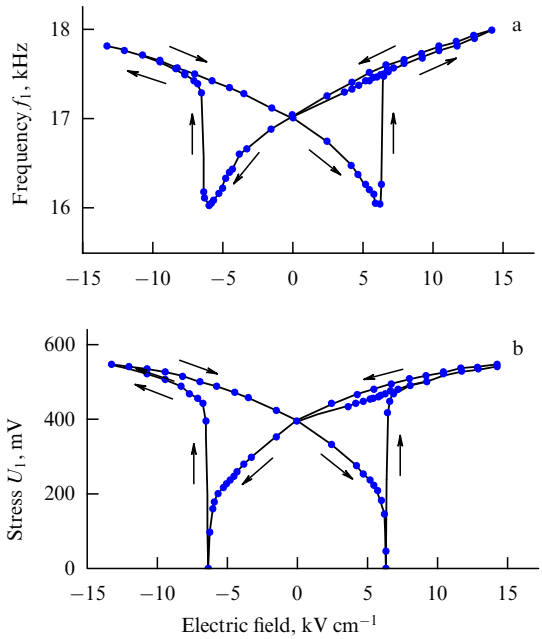

Figure 31. Dependence of resonance frequency f_1 and ME voltage U_1 on electric field E applied to the PE layer of an Ni–PZT composite structure.

vibrations. The field dependence of field mixing efficiency, as well as the efficiency of second-harmonic generation, is determined by the second derivative $\lambda^{(2)}(H)$ of magnetostriction over field and reaches a maximum at $H = 0$.

The efficiency of field transformation in composite structures can be controlled not only by a constant magnetic field H, but also by a constant electric field E applied to the PE layer [222]. Figure 31 depicts dependences of the resonant frequency f_1 of bending vibrations and voltage U_1 generated at this frequency on an applied electric field for an Ni–PZT structure. Deformations created by field E due to the inverse piezoeffect result in renormalization of Young's modulus in the PE layer and the entire structure, which causes a $\sim 12\%$ shift of the resonant frequency of bending vibrations. Moreover, field E alters piezomodulus d_{31} and dielectric constant ε of the PZT layer and thereby the amplitude of voltage U_1 generated by the structure. At fields $E \approx \pm 6.5$ kV cm^{-1}, polarization of the PZT layer becomes inverted, and the voltage amplitude vanishes.

The application of a strong constant electric field E to the structure PE layer results in manifesting the converse static ME effect [223, 224]. Due to the converse piezoelectric effect, the electric field causes deformation of the substrate under the PE layer that is transferred to the FM layer, thus giving rise in it to an effective field of uniaxial magnetic anisotropy

$$H_{\text{eff}} = 3\lambda_{\text{s}} d_{\text{eff}} \frac{EY}{M_{\text{s}}}\,, \tag{16}$$

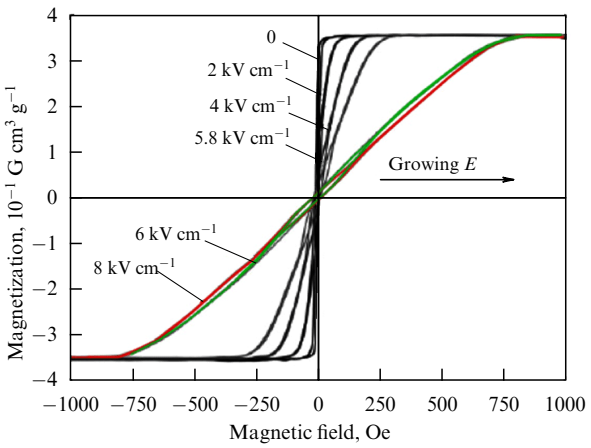

Figure 32. Influence of field E on hysteresis loop shape in an FeGaB layer (100 nm) on a PZN–PT substrate (0.5 mm). (Adapted figure from Ref. [224] by courtesy of N Sun.)

Table 2. Materials used to make composite structures.

Magnetostrictive phase	Piezoelectric phase
Metals: Ni, Co, Fe	Ceramics $Pb(ZrTi)O_3$ (PZT)
Alloys: permendur ($Fe_{0.49}Co_{0.49}V_{0.2}$), galfenol ($Ga_{0.17}Fe_{0.83}$), samfenol ($SmFe_2$), terfenol-D ($Tb_{1-x}Dy_xFe_2$), Ni_2MnGa	Ceramics and single-crystals: $Pb(Mg_{1/3}Nb_{2/3})O_3-PbTiO_3$ (PMN–PT), $Pb(Zn_{1/3}Nb_{2/3})O_3-PbTiO_3$ (PZN–PT), $Pb(Zn_{1/3}Nb_{2/3})_y-(Zr_xTi_{1-x})_{1-y}O_3$ (PMN–PZT)
Fe-based amorphous alloys: FeBSi, FeBSiC, FeCoB, FeCoSi, FeCoSiB	Piezocrystals: AlN, $BaTiO_3$, $LiNbO_3$, quartz, $Ba_{1-x}Sr_xTiO_3$, $LaGa_{5.5}Ta_{0.5}O_{14}$ (LGT)
Ferrites: $Y_3Fe_5O_{12}$, $NiFe_2O_4$, $CoFe_2O_4$, Li-ferrite, Mn-ferrite, Ba-hexaferrite	Piezopolymers: polyurethane (PU) and Polyvinilidene difluoride (PVDF)
Ceramics: Fe_3O_4, $Zn_{0.1}Fe_{2.9}O_4$, $La_xSr_yMnO_3$, $La_xCa_yMnO_3$	Semiconductors: ZnS, GaAs, GaP

where Y, λ_s, and M_s are Young's modulus, magnetostriction, and saturation magnetization of the FM layer, respectively, $d_{eff} = (d_{31} - d_{32})/(1+\gamma)$ is the effective piezomodulus, and γ is the Poisson coefficient of the PE layer.

Figure 32 demonstrates an converse static ME effect, i.e., a change in the shape of hysteresis loops in response to the application of a constant field E in an amorphous FeGaB film prepared by magnetron sputtering over a monocrystalline piezoelectric substrate. The loops were obtained with a vibrational magnetometer by PZN–PT crystal magnetization along the axis [100] at various E values.

3. Composite materials and devices of magnetic straintronics

The practical aspects of straintronics should be considered bearing in mind the key ideas underlying its applications in electronics, computer memory, energy-saving technologies, and microwave and sensor techniques originally intended for multiferroics and magnetoelectrics [3, 225–227]. The use of composite materials and straintronic heterostructures made it possible to bring to life many of these ideas or at least to come closer to their implementation.

3.1 Composition of structures and their formation methods

Of special interest for magnetic straintronics are layered structures with type 2–2 two-dimensional deformations (according to the classification made in Section 1.4) in the form of mechanically connected alternating magnetostrictive and piezoelectric layers. Table 2 lists the main magnetostrictive and piezoelectric materials utilized to prepare them [228–230].

The most promising magnetostrictive materials are iron-based amorphous alloys characterized by reasonably high saturation magnetostriction $\lambda_s \sim (2-4)\times 10^{-5}$ in small fields $H_s \sim 10-100$ Oe, gallium and rare-earth alloys with giant magnetostriction, $\lambda_s \sim 10^{-4}-10^{-2}$, and various low-conductivity ferrites. Relevant piezoelectrics include PZT-based ceramics, PMN–PT and PZN–PT crystals with a large piezomodulus, and crystals of aluminum nitride, langatate, lithium niobate, and some others characterized by a high piezomodulus-to-dielectric constant ratio and low acoustic losses. Flexible structures are manufactured from polymeric (polyurethane and PVDF) piezoelectrics. Finally, layered piezosemiconductor structures (ZnS, GaAs, etc.) have good prospects for integration with micro- and acoustoelectric technologies.

Composite structures are produced by various methods, depending on layer thickness. They may be built up by adhesive bonding of layers as thick as a few dozen micrometers to several millimeters to facilitate strain transfer between the layers. Coating with ceramic thin films and subsequent baking at $\lesssim 1000\,^\circ$C are applied to fabricate structures with 10–50-μm thick layers. Electrolytic deposition of metals (Ni, Co) allows making up magnetostrictive layers of several to a few dozen micrometers in thickness on arbitrarily shaped surfaces. Well-established methods of laser spraying and magnetron deposition, gas-phase deposition, molecular beam epitaxy, spin coating, spray pyrolysis, and a combination of these techniques are employed to produce thin-film structures with magnetostrictive and piezoelectric layers of thicknesses ranging from a few nanometers to several micrometers. The choice of substrate material and thermal expansion coefficients (which must be close to the respective characteristics of the layers to prevent their destruction during cooling) is crucial for engineering thin-film composite structures by high-temperature techniques.

3.2 Memory and logical devices switched by an electric field

The great interest in straintronics is supported by hopes to create magnetic memory cells and computer logical elements [3, 5, 23, 93, 96, 97, 109, 110, 118, 126, 231–233]. The advantages of straintronic devices include minimal energy dissipation in recording, readout, and processing information, as well as their compatibility with logic technologies based on metal–oxide–semiconductor (CMOS) transistors. The memory and logical schemes considered below can be described as a hybrid of straintronics and spintronics, because the application of mechanical stress causes rotation of magnetization (spin ensemble) for performing the computing operations [5, 93].

By analogy with the tunnel magnetoresistive random-access memory (MRAM) cell, a straintronic magnetoelectric random-access memory (MeRAM) cell consists of two

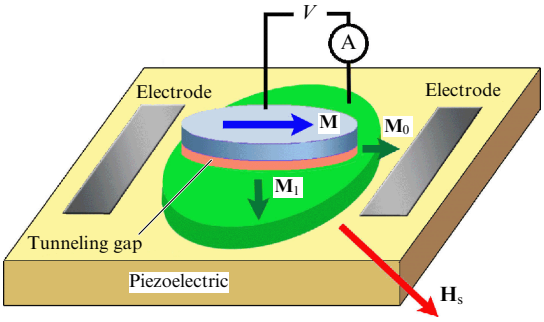

Figure 33. Schematic of straintronic tunneling magnetoelectric memory cell with elliptical particles differing in aspect ratios.

uniformly magnetized ferromagnetic layers (with fixed and relatively free orientation of magnetization) separated by a tunneling gap of oxide and deposited on a piezoelectric base (Fig. 33). The free layer lies near the piezoelectric, and the orientation of its magnetization varies under the influence of mechanical stresses induced by compression and tension of the piezosubstrate to which an electric potential is applied. Simultaneously, the fixed layer retains the orientation of its magnetization. The current flowing through such a magnetoresistive device encounters electrical resistance, depending on the angle between magnetization vectors in the fixed and free ferromagnetic layers. The most pronounced change in the current is associated with a 180° turn of magnetization in the free layer with respect to magnetization in the fixed one. In the MeRAM cell, the change is caused by mechanical stresses induced from the side of a substrate, which accounts for the special attention paid to the magnetization rotation in ferromagnetic particles in response to their compression and tension (see Section 2.1).

One-domain ellipsoidal ferromagnetic particles are most suitable for creating nanoscale straintronic elements. The shape of the particles or, to be precise, their aspect ratio (long-to-short axis ratio) determines their susceptibility to strain. In elongated particles with a large aspect ratio, magnetic shape anisotropy prevails over magnetoelastic anisotropy, and they have a fixed orientation of magnetization (another way to fix magnetization in a given layer consists in its exchange-coupling to an additional antiferromagnetic layer [234]). Magnetization of a wider particle in which magnetoelastic anisotropy prevails over shape anisotropy can be regarded as relatively free; it will turn when an electric potential is applied to the piezosubstrate. This principle underlines the MeRAM cell schematically presented in Fig. 33. Its two electrodes need to be supplemented by an additional external magnetic field H_s for inducing two energetically stable states with different magnetization orientations corresponding to '0' and '1'. In the cell shown in Fig. 33, the maximum current flows through a tunneling structure when $\mathbf{M}$ and $\mathbf{M}_0$ vectors are unidirectional (state '0'), and the minimum current when magnetization transfers to position $\mathbf{M}_1$ after the electric potential is applied to the piezosubstrate [the angle between magnetization directions in two positions, $\mathbf{M}$ and $\mathbf{M}_1$, ranges from 90 to 170°, depending on the value of H_s and the magnetic anisotropy of the particle (see Table 1)].

Recently, the possibility of applying the four-electrode scheme to control memory cell resistance, analogous to the one shown in Fig. 33 but without an additional external magnetic field, has been demonstrated [235]. A distinctive feature of the cell is the use of ellipsoidal particles with fixed and free magnetizations and long axes directed at an angle of 45° to each other. Modeling a straintronic memory device composed of an ensemble of such cells gave evidence that its efficiency in terms of energy consumption and frequency characteristics is one order of magnitude higher than that of the existing analogous storage structures designed with the employment of CMOS technology [235].

Lead zirconate–titanate — PZT ($PbTiO_3 - PbZrO_3$) [106, 109, 236] and lead magnoniobate — PMN–PT ($0.70Pb(Mg_{1/3}Nb_{2/3})O_3 - 0.3PbTiO_3$) [23, 129] are most frequently used as piezosubstrates. The ferromagnetic layers for model calculations are usually made of Ni [24, 106, 237], Co [23, 96, 109], FeGa [129], $TbFe_2$ [104], and $Co_{40}Fe_{40}B_{20}$ [111]. Maximum magnetostriction of $Tb_{0.7}Dy_{0.3}Fe_2$ alloy (terfenol-D) at room temperature was utilized in many calculations [238].

In the usual MeRAM scheme presented in Fig. 33, recording time varies from 2 to 10 ns, and the energy dissipated in the recording of one bit is close to 4 aJ with almost 100% probability (according to model calculations [93, 97, 129]). In other words, the energy consumption is 10^4 and 10 times lower that in the STT–RAM [239] and STT–Hall [240, 241] methods, respectively. In the latter method, energy gain is achieved owing to the STT-effect (magnetic moment transfer to free layer atoms from spin polarized electrons formed due to the giant Hall spin effect).

An appreciable change in resistance in a tunneling magnetoresistive cell is impossible in materials with high magnetostriction coefficients ensuring a pronounced magnetoelastic effect, such as terfenol-D. Therefore, a more efficient scheme of a straintronic memory cell was proposed with two separate blocks, one for reading and the other for recording (Fig. 34) [242]. In this cell, the piezoelectric layer adjoins the magnetostrictive layer of terfenol-D with magnetization turning by virtue of stress anisotropy induced in it by the application of an electric potential to the piezosubstrate in the course of information recording. Magnetization of the adjacent free layer also turns due to its magnetic dipole coupling with the magnetostrictive layer. In the reading block, the free magnetization layer forms from CoFeB, the use of which in tunneling structures permits magnetoresistance up to 300% to be achieved [243].

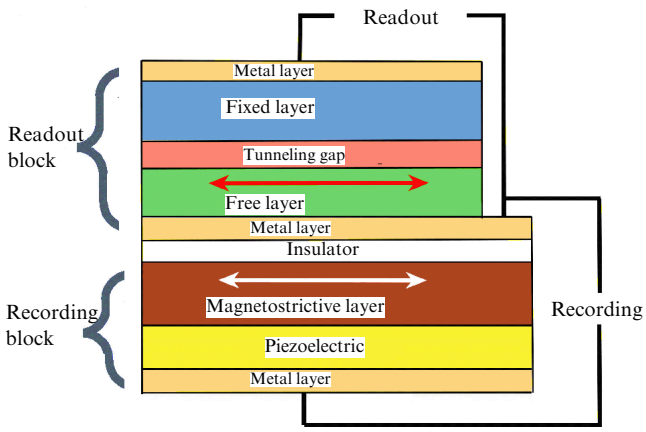

Figure 34. Diagram of a straintronic tunneling magnetoelectric memory cell with dipole-coupled magnetostrictive and free layers.

When high enough mechanical stress is induced in a magnetostrictive layer, projections of magnetization vectors of both layers are oriented along the short axis of a particle, and the vectors themselves go out of the plane. Magnetizations of the layers retain an antiparallel orientation when they reach the hard axis (because they remain antiferromagnetically coupled). Stress relieving switches the magnetostrictive layer in the opposite direction due to out-of-plane deflection of magnetization (by the mechanism described in Section 2.1) that is turned through 180° in the absence of an external additional magnetic field (Fig. 11) [5, 100, 101, 124]. As a result, the regime of 180° magnetization turn in the free layer relative to magnetization of the fixed layer is realized in the recording mode, markedly changing the resistance of the readout unit. Model calculations with the use of the LLG equation showed that the energy dissipated for recording one bit of information is less than 1 aJ, and recording time is shorter than 1 ns [242]. Such a 180° magnetization switching procedure requires a readout of the magnetization state for determining the instant of time at which magnetization projection falls along the short axis of an ellipsoidal particle. If usual current-operated devices (transistors) with high heat release from electron transport are used for the purpose, energy dissipation reduces to zero the advantages of straintronic recording procedure [93]. The authors of Ref. [18] argue that the problem can be solved by designing and using a straintronic transistor to replace analog current transistors in devices with ultralow energy consumption for information processing systems.

Most efforts to design and develop straintronic memory cells are based on results of theoretical research and model calculations allowing the magnitude of energy dissipation, single-bit recording time, estimation of error probability, and contribution from thermal noises to be predicted.

In one of the first experimental studies, a multilayer ferromagnetic macroparticle was deposited onto a commercial piezoelectric actuator [236] in an external magnetic field, due to which the deposited particle acquired uniaxial magnetic anisotropy. In later studies, the external magnetic field $H_s = 0.13$ T was applied to maintain two stable magnetization states in the particles, corresponding to '0' and '1' (an approach analogous to that described in Section 2.1 and Refs [104, 105, 129]). The delivery of a 10-ms electric pulse to the piezoelectric element induced either compression or tension (depending on pulse polarity) and a transition of magnetization to one of the stable states due to the magnetoelastic effect. This observation was confirmed by measurements of magnetization using a vibration magnetometer and the magneto-optic Kerr effect.

Further development of this idea was the creation of a prototype MeRAM memory cell with the opportunity of magnetoelectric readouts (Fig. 35) [128, 244].The prototype model was stably switched by 0.25-ms pulses (Fig. 35b). The recorded information (i.e., position of vector **M**) can be readout using a magnetoresistive sensor or taking advantage of ME effect reversibility (a change in the magnetic state of the FM layer is accompanied by pulses of 'magnetoelectric' voltage V_{ME} that the authors of Ref. [128] define as the difference between signals picked off a load resistance in the presence or absence of a magnetic field: $V_{ME} = V_R(H) - V_R(0)$). This voltage differs from zero only when a magnetization switch in the device occurs; therefore, a repeated recording pulse of the same polarity failing to change the element's state does not induce a V_{ME} signal (see

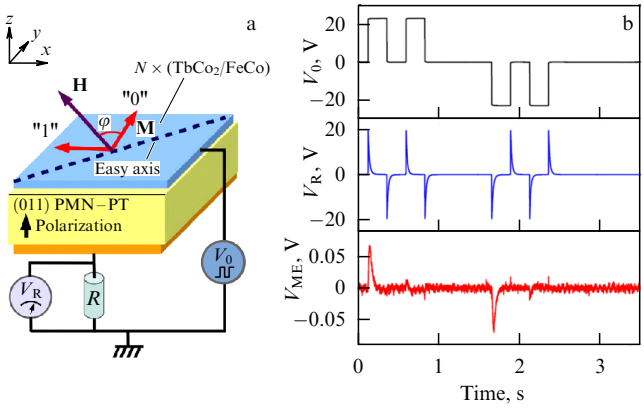

Figure 35. Nonvolatile memory with electric field switching $(TbCo_2)_{4nm}/(FeCo)_{4nm}$. Magnetostrictive film from 25 exchange-coupled layers (total thickness 100 nm). (Adapted figure from Ref. [128] by courtesy of the authors.)

the bottom plot in Fig. 35b). This procedure is a variant of the *destructive reading mode*, because the readout requires a change in the element's state. Once the initial state was read out, it is restored by an additional recording pulse. In a recent publication [245], the same authors proposed a new modification of the ME readout method based on difference measurements with the aid of a bridge configuration.

Presence of two kinds of ordering (magnetic and ferroelectric) in ME composites make it possible to realize a new type of memory with four stable states [246]. Stable states of MeRAM memory element I–IV differ in opposite directions of magnetization in the magnetic Co layer and polarization in the piezoelectric PZT layer (Fig. 36). The two materials have rather wide hysteresis loops, as well as strong residual magnetization and polarization. Information can be read out based on the direct ME effect [128] or traditional methods for reading out information from magnetic storage, e.g., using resistive transducers. The application of four-level memory elements will require new designs of

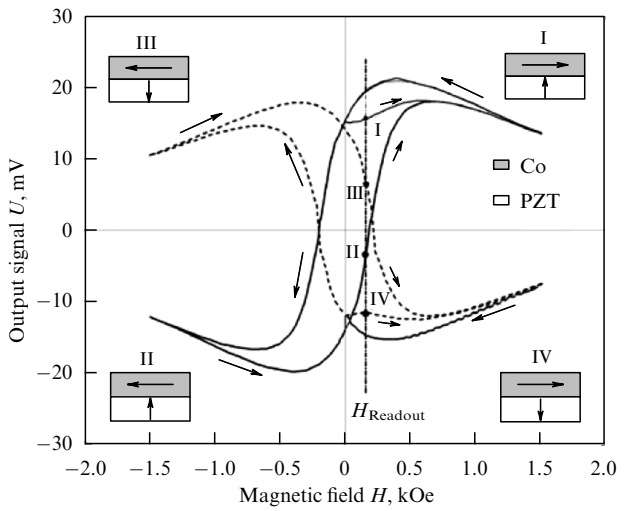

Figure 36. Four-level memory based on Co–PZT composite structure. Switching between states is effected by applying external field $H > 1.5$ kOe or electric field $E > 2$ kV cm^{-1} pulses. (Adapted figure from Ref. [246] by courtesy of C W Nan.)

memory architecture, but may have a number of advantages over existing technologies.

A recent breakthrough in experimental studies is the creation of a MeRAM prototype operating in the tunneling spin valve regime regulated by an electric field through a piezosubstrate [247]. It is a multilayer structure composed of $Co_{20}Fe_{60}B_{20}$(10 nm)/MgO(1.8 nm)/$Co_{20}Fe_{60}B_{20}$(4 nm), 8×3 μm^2 in size, elliptically shaped in its plane, and placed on a PMN–PT crystalline piezosubstrate. The device has some distinctive features, viz. closely spaced dipole-coupled magnetic layers, a 10-nm thick magnetically hard layer with the coercive force greater than that of the magnetically soft 4-nm layer, a weak external magnetic field (3 mT) directed along the particle's long axis, and two electrodes specially shaped to concentrate mechanical stresses on the particle and induce local stresses in both layers through the piezosubstrate. When an 80-V voltage is applied across the electrode, the effective field of magnetoelastic anisotropy compensates for the action of an external field, and magnetization vectors of the upper and lower layers of the particle become oriented in opposite directions due to magnetostatic dipole interaction between them, as confirmed by results of magnetization modeling with the aid of the well-known OOMMF software (Fig. 37a) [247]. The 180° angle between magnetizations of the upper and lower layers accounts for maximum resistance. The application of −80 V to the electrodes proves enough for the external magnetic field to form a co-directed orientation of magnetizations of the two layers and thereby ensure minimal resistance to electricity flowing through them (Fig. 37b). In other words, the electric potential with a variable sign allows switching the resistance of a tunneling magnetoresistive heterostructure (Fig. 37c). It was hypothesized in Ref. [247] that the use of a 100-nm thick piezosubstrate would decrease the dissipation energy by six orders of magnitude, to 20 aJ, while the use of four electrodes instead of two makes it possible to give up the external magnetic field.

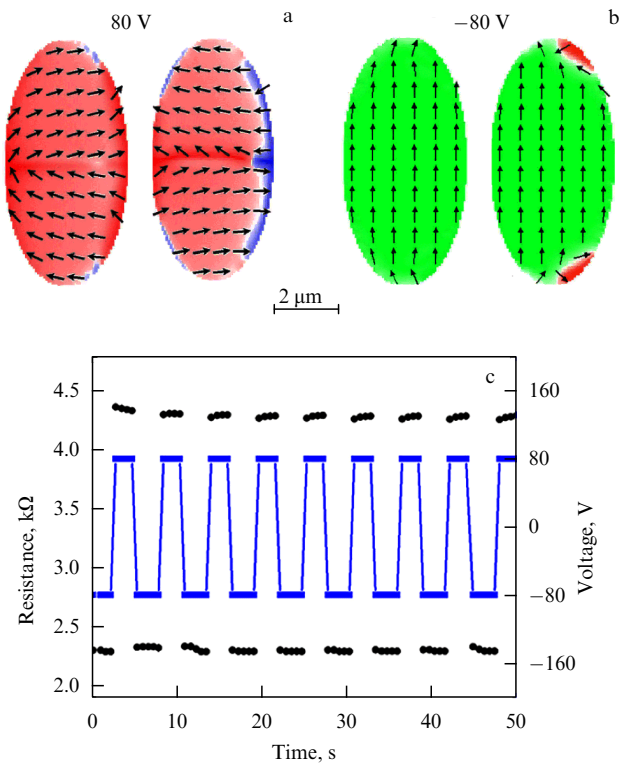

Figure 37. Resistance variation in a straintronic tunneling cell (spin valve). Orientation of magnetization in upper and lower magnetic layers at maximum (a) and minimum (b) resistance. (c) Experimental dependences of resistance changes upon sequential switching of voltage applied across the piezosubstrate from −80 to 80 V. (Adapted figure from Ref. [247] by courtesy of the authors.)

The necessity of minimizing the energy consumption for information recording and processing stimulates the development of straintronic logical devices [23, 24, 93, 95, 238, 248–250]. Logical elements (nanomagnets) are placed at certain sites on the surface, so that dipole interactions between them determine the desired logical operations on bits encoded in their magnetization orientations. In this case, the logical switching schemes are interconnected by 'wires' in the form of a chain of closely spaced dipole-coupled magnetic nanoparticles. The transmission of binary information proceeds not by virtue of the electron transfer, as in conventional electronics, but owing to a consecutive magnetization reversal in single-domain nanoparticles placed on a piezosubstrate (so-called Bennet clocking) [251].

Magnetization turn in two dipole-coupled particles is exemplified by remagnetization of two neighboring Co particles on a PMN–PT piezosubstrate [23]. Particles *1* and *2*, 12 nm thick each, have different aspect ratios, 1.67 and 1.14, respectively (Fig. 38). The unidirectionally pre-magnetized particles are spaced ∼ 300 nm apart (in Fig. 38d, magnetic field direction is indicated by the white arrow). Mechanical stress induced from the side of the piezosubstrate (∼ 80 MPa) turns the magnetization of particle *2* with a lower shape anisotropy through about 90°, whereas magnetization of particle *1* turns insignificantly due to the predominance of magnetic shape anisotropy over induced magnetoelastic anisotropy (Fig. 38b). Such an orientation of magnetizations in particles *1* and *2* is due not only to evoked magnetic anisotropy but also to dipole–dipole interaction between them. After stress relieving, magnetization of particle *2* rotates owing to dipole–dipole interaction with particle *1*

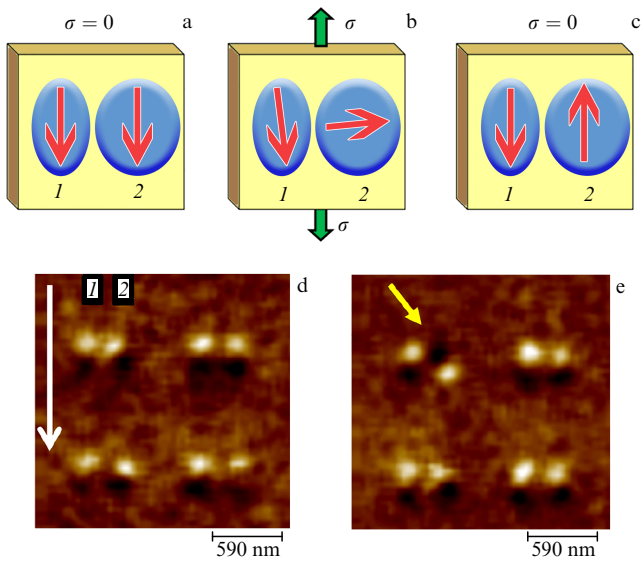

Figure 38. (Color online.) Remagnetization of dipole-coupled Co particles *1* and *2* differing in aspect ratios in the initial state (a), under tensile strain from the side of piezosubstrate (b), and after strain relaxation (c). MFM images of four pairs of particles before (d) and after (e) applying elastic strain. (Adapted figure from Ref. [23] by courtesy of the authors.)

and takes a new energetically favorable position (Fig. 38c). Importantly, the turn of magnetization of one of the dipole-coupled particles through an angle close to 90° is sufficient to switch its magnetization to a stable state with the opposite orientation, i.e., from state '0' to state '1'. In experiments, magnetization turnover in the second particle can be observed with the aid of MFM. Such switching occurred only in one pair of particles of the four present in the MFM image (indicated by the yellow arrow in Fig. 38d, e) due to the imperfection of the lithographic process applied to obtain particles of the desired size and shape. Even in the case of a slight deviation in size, this leads to the spread in magnetic anisotropy determined by particle's shape and reduces the probability of switching the particle magnetization [23].

An important element of the logical scheme is a 'binary nanowire', indispensable for unidirectional bit transfer from one logical element to another. The 'binary nanowire' may consist only of identical single-domain dipole-coupled nanoparticles, as shown in Fig. 39. The necessary orientation of magnetization for each nanoparticle is set by strain generated in the piezoelectric layer underlying each particle by applying an electric potential to the particle. An important role is played then by magnetic dipole interaction with the nearest neighbors. In the initial state, a chain of four ellipsoidal nanoparticles resides in the ground state with the antiferromagnetic mutual orientation of magnetization, indicated by red arrows in Fig. 39a. If the magnetization of the first particle turns over in response to external input, the second one proves to be in an unstable state, where dipole impacts from left and right neighbors are canceled out (Fig. 39b). At the next stage, the second and third particles are subjected to electrically induced stresses and their magnetizations take a new direction close to that of the hard axis (Fig. 39c). Then, the second particle is relieved from strain and passes into the desired state with magnetization opposite to that of the first particle (Fig. 39d), because its dipole interaction with the left neighbor becomes stronger than with the right one, the field-induced torque from the side of the left particle being greater than from the right one. Thus, step by step (from left to right), turning on the voltage in two neighboring particles allows transmitting information about magnetization turn in the first particle to the last one in the chain. Just this process underlies Bennet clocking [93, 95, 238]. Numerical estimates show that such a straintronic wire with a bit transfer rate of 1 GHz needs as low an energy as 0.8 aJ to remagnetize a single 100-nm terfenol-D nanoparticle when the distance between particles is about 200 nm. In a wire from four nanomagnets, the overall energy dissipation during the transfer of a single bit is $\sim$ 1.6 aJ [238].

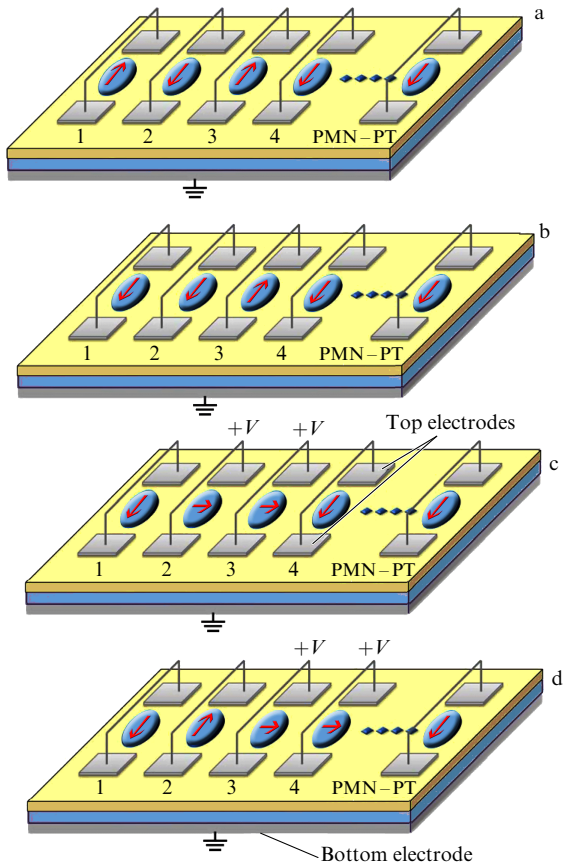

Figure 39. (Color online.) Magnetization switching in a chain of dipole-coupled elliptical particles on a piezosubstrate: (a) initial state, (b) after magnetization turn in particle *1*, (c) after applying potential to the piezosubstrate underlying particles *2* and *3*, (d) after voltage removal from particle *2* and induction of mechanical stresses in particles *3* and *4*.

Round particles, in addition to elliptical ones, can also be used in binary nanowires [24]. In this case, magnetoelastic anisotropy must be induced in each particle instead of the absent magnetic shape anisotropy by application of a potential to the underlying piezosubstrate, as before. It makes the round particles bistable, and a chain of them, like a chain of elliptical particles, can be used to transmit numerical information by the Bennet mechanism. At the same time, round-shaped particles offer certain advantages in this context: (1) the absence of a shape anisotropy energy barrier decreases the amount of energy needed to reorient magnetization, and (2) the in-plane size can be reduced to 20 nm, which otherwise would be impossible due to the thermal stability problem. Voltage-induced magnetoelastic anisotropy in round particles stabilizes magnetization, even if they are only a few dozen nanometers in size, which eliminates the problem. It allows building up nanomagnetic logic based on much smaller particles than before. Model calculations are confirmed by the results of experimental studies making use of the magneto-optical Kerr effect for an ensemble of 100 nm round Ni particles on a PMN–PT piezosubstrate. It was shown that dipole–dipole interactions between the particles strongly affects the formation of magnetic anisotropy in them by the electric potential applied to the piezosubstrate [24].

This method of information transfer between dipole–dipole interacting particles can be employed, in principle, to design straintronic logical devices, as exemplified by a structure from 12 terfenol-D nanoparticles 100 nm in size with a 1.1 aspect ratio, capable of performing an AND–NOT logical operation [96]. In Fig. 40, the interparticle distance $r = 200$ nm and $\sqrt{3/2}\,r$ in the direction of the short and long axes, respectively. Modeling the operation of such a device with LLG equations showed that the consecutive application of potentials to piezoelectrics under each particle ensures a response time of 2 ns with a dissipated power in each AND–NOT operation of about 5 aJ per bit [96].

Unfortunately, the probability of incorrect switching of magnetization in dipolar logical structures is quite high not only because of fabrication-induced imperfections in elements (particles) but also due to contribution from thermal noises [103, 118, 250]. Reducing interparticle distances

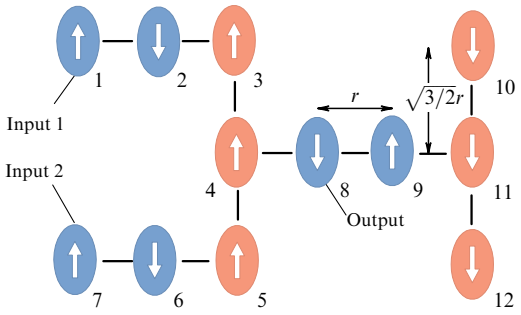

Figure 40. Illustration of a straintronic device from 12 elliptical dipole-coupled nanoparticles performing an AND–NOT logical operation.

decreases the probability of an error to 10^{-6} owing to enhanced dipole–dipole interaction between particles; yet, it is still unacceptably high. Attempts to improve the stability of the performance of such logical devices are based on additional control of magnetization switching in the particles, but the problem remains unsolved [118].

More promising is the employment of the tunneling magnetoresistive cell [236, 248], shown in Fig. 33 as a straintronic element of the above logic. This cell can also perform the AND–NOT operation if input signals are V_1 and V_2 potentials applied to the left and right electrodes, respectively, placed on a piezoelectric near the cell, and the output signal is a voltage drop on the cell. Theoretical estimates show that the time needed for a single operation in such a structure is 1.3 ns, dissipated energy 12.4 aJ, and probability of error less than 10^{-8} [248].

Magnetic dipole–dipole interaction between straintronic elements can also be utilized in image processing [252] to suppress noises (random pixels differing in color from the immediate neighbors) or to enhance and detect an object edge. In this case, pixels stand as straintronic elements with two logical states, corresponding to the mutually perpendicular directions of magnetization given by particle shape anisotropy and external magnetic field (see Fig. 33). Computer simulation [252] shows that the induction of mechanical stress in the matrix of straintronic elements by applying an electric potential to the common ferroelectric substrate under dipole interaction conditions changes the magnetization of the element, so that the 'color' of the element becomes comparable with the background. After removal of voltage, most pixels return to the initial state and occasional contrast divergences become corrected. Figure 41 shows results of the treatment of the diffuse interface between dark and light fields; clearly, the application and removal of voltage produce a very apparent boundary between the dark and light fields.

Obvious advantages of straintronic elements in the form of memory cells and logical devices include ultralow energy consumption in recording [5] and readout [128] of information. Their major disadvantage is the relatively low density of arrangement. However, a great variety of applications of such elements in mobile electronic products, computers used in space, and implanted medical processors, where energy efficiency is the critical characteristic, make straintronic devices very attractive for the purpose.

3.3 Sensors, energy converters, and microengines

Strain-assisted conversion of magnetic and electric fields in composite structures can also be used to create highly

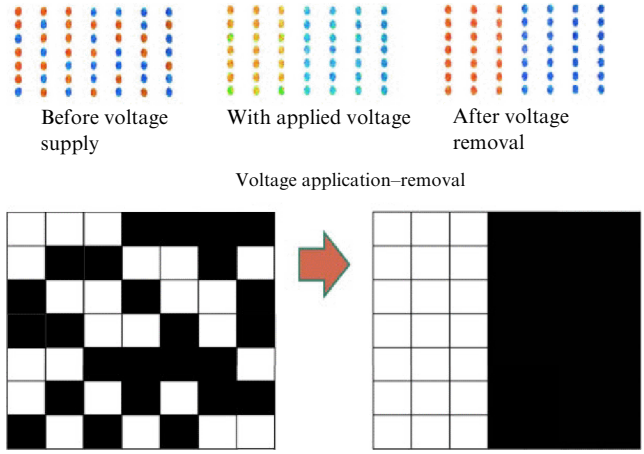

Figure 41. Image processing by straintronic technology: dark band edge extraction in the matrix of straintronic elements after application and relaxation of mechanical stress (dark and light pixels correspond to elements of two logical states with mutually perpendicular magnetization-affecting voltages) (Based on Ref. [252].)

sensitive magnetic field sensors [253, 254] and autonomous sources of energy [255].

The dependence of the amplitude of alternating voltage generated by a composite structure on the magnetic field can be used to measure the alternating magnetic field amplitude [256]. Such sensors contain micrometer-thick layers of magnetostrictive and piezoelectric materials deposited on a silicon beam (Fig. 42a), which makes up an oscillatory system with a relatively high (~ 300) Q-factor. At a resonance frequency of ~ 0.9 kHz, the structure is characterized by the magnetoelectric coefficient $\alpha_E = 5$ kV cm^{-1} Oe^{-1} and inherent magnetic noises below 4 nV Hz$^{-1/2}$. This allows the detection of alternating magnetic fields with a minimal amplitude of ~ 400 fT.

A similar sensor operating in the low-frequency range was made from a flexible Metglas–PVDF structure obtained by the deposition of a piezopolymer directly on a magnetostrictive layer [213]. The sensor permitted detecting magnetic fields with a minimal amplitude up to ~ 10 nT (at the resonance frequency of bending vibrations of ~ 30 Hz, the structure had an ME coefficient $\alpha_E = 850$ V cm^{-1} Oe^{-1}, i.e., 40,000 times the coefficient of the linear ME effect in the classical magnetoelectric Cr_2O_3). ME sensors of magnetic fields are shown to be suitable for data reading from magnetic disks [257]. Composite-based ME sensors can also be used as antennas to detect the magnetic component of mega- and giga-hertz electromagnetic radiation; one of their merits is the additional possibility of miniaturization by a few hundred times compared with traditional electromagnetic antennas, because the size of ME sensors depends on the acoustic vibration wavelength in a composite structure rather than the electromagnetic radiation wavelength [258].

For many applications, e.g., magnetocardiography and magnetoencephalography, highly sensitive broad-band sensors capable of recording fields in a low-frequency range of 1–100 Hz are needed. This stimulated the development of new principles of designing magnetic field sensors based on composite structures.

It was proposed to use the mixing of magnetic fields with frequency translation to a higher frequency region to measure low-frequency fields [259–261]. To this end, the field to be

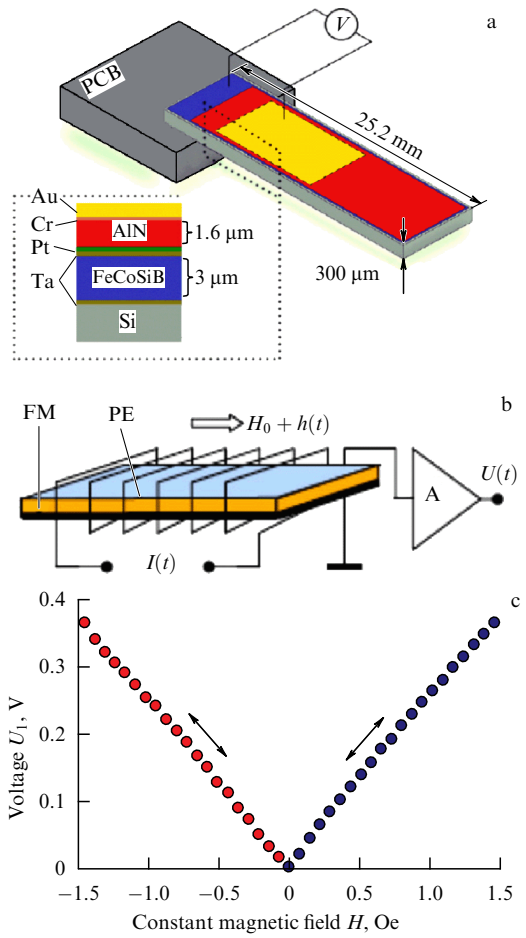

Figure 42. Magnetic field sensors based on magnetoelectric composite materials. (a) FeCoSiB–AlN-based sensor of alternating fields [256], PCB — printed-circuit board. (b) Layout of constant field sensor. (c) Dependence of output signal of constant field sensor on the field being measured.

measured with frequency f is applied to the structure, together with a modulating field of frequency f_1, such that $f \pm f_1 = f_0$, where f_0 is the resonance frequency of the structure. The frequency spectrum of a field being measured is translated into a higher frequency region with minimal noise from the measuring electronic instruments. In this way, it is possible to record low-frequency fields and reduce the minimal field strength by one order of magnitude. A similar idea is implemented in a spectrum analyzer of the low-frequency magnetic field [262]. The alternating magnetic field being studied is mixed with a field induced by a pumping oscillator, and the signal is registered at a summary or difference frequency equal to the acoustic resonance frequency. Scanning the pump field frequency f_1 gives the frequency spectrum of the measured magnetic field.

However, the above sensors do not allow constant magnetic fields to be measured, because the output signal highly decreases at frequencies $f < 1$ Hz [263] due to the finite conductivity of the PE layer in the structure [263]. A magnetostrictive analog of the fluxgate magnetometer (Fig. 42b) has been proposed, in which the nonlinear dependence of the FM layer magnetostriction on the magnetic field is used [264, 265]. A composite structure is placed in a coil-generated harmonic pump field with a high enough amplitude $h(t)$ and the parallel field H being measured. Due to the nonlinear ME effect, the structure generates voltage harmonics (see Section 2.5). As shown in Refs [264, 265], the amplitudes of the first and third harmonics are linearly dependent on H; this dependence is put on to measure the constant field. Hysteresis is suppressed in the case of a high enough modulating field amplitude, comparable to that of the FM layer saturation field, $h \sim H_s$; this ensures a high accuracy of measurements. The sensor can be utilized to register fields up to 1 μOe with frequencies ranging from 0 to 200 Hz.

References [266, 267] describe an ME sensor of constant fields based on measuring the dependence of the acoustic resonance frequency of an ME structure on a constant magnetic field, originating from the dependence of the FM-layer Young's modulus on magnetic field-induced magnetostrictive deformation. A Metglas–PZT-based sensor with a sensitivity of 10 Hz mOe^{-1} permitted registering magnetic field variations of up to 10 nT.

To recall, permanent magnetic fields can also be detected in straintronics based on a different principle, i.e., making use of the changes in the optical properties of semiconductor magnetic materials under the influence of mechanical strains. For example, the IR reflection coefficient of ferrimagnetic spinel $CoFe_2O_4$ varies under the action of the magnetic field owing to magnetostrictive properties of the material and the dependence of the spinel band structure on mechanical stresses [268]. However, the sensitivity of optical straintronic sensors is still far from that of composite heterostructures: the reflection coefficient in an ~ 1 kOe magnetic field undergoes a change of several percent [268].

By virtue of the high limiting energy density in the FM phase ($w \sim 10$ W cm^{-3} for terfenol-D) and PE phase ($w \sim 10$ W cm^{-3} for PZT), composite structures can be used not only for measuring magnetic fields but also for designing solid-phase devices to convert magnetic field energy into electric field energy. Reference [269] describes a transformer

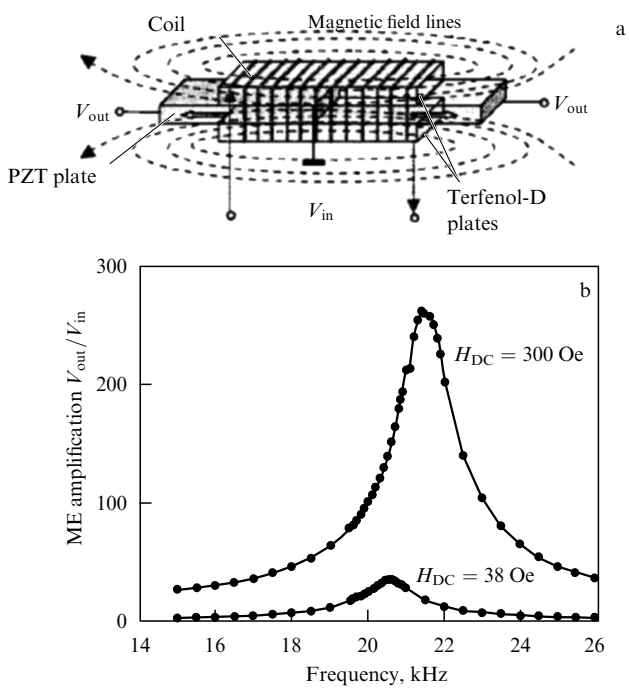

Figure 43. (a) Transformer layout. (b) Frequency dependence of transformation ratio on bias fields $H_{DC} = 38$ and 300 Oe. (Adapted figure from Ref. [269] by courtesy of the authors).

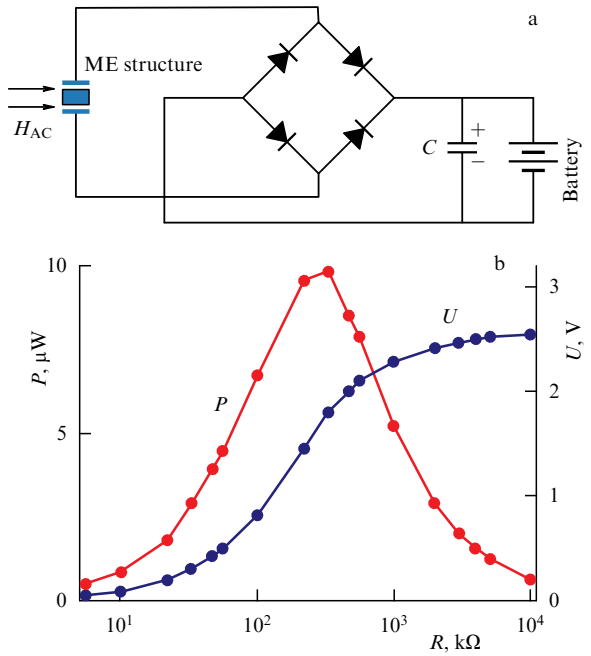

Figure 44. (a) Schematic of autonomous source of constant voltage. (b) Load resistance (R) dependence of voltage U and power P.

with voltage buildup regulated by a constant magnetic field (Fig. 43). The transformer contained a composite structure placed in a low-ohmic electromagnetic coil. Coil input voltage generated a resonance-frequency modulating magnetic field; the output voltage was picked up from a piezoelectric plate. The transformation ratio varied from zero to a maximum value of 260 as the constant magnetic field changed from 0 to 300 Oe; the estimated efficiency of energy transfer amounted to 50%. Transformers based on composite structures guarantee a higher transformation ratio than purely piezoelectric devices do.

A promising trend in straintronics is the development of autonomous low-power generators of electric energy with the use of composite structures capable of converting technogenic or natural alternating magnetic fields into constant voltage (energy harvesting) [270–272]. Such a generator (Fig. 44) contains a composite structure, semiconductor rectifier, and resistance (R)-loaded supercapacitor. Under the influence of an alternating magnetic field and due to the direct ME effect, the structure induces voltage with an amplitude up to several volts. Rectified voltage increases with load resistance R, and the power generated may reach a few dozen or hundreds of microwatts (Fig. 44b), enough to charge a battery or feed a module containing a sensor and a radioset for wireless transmission of information. Such generator has an almost unlimited service life and can substitute for a chemical power source. Areas of applications of ME energy sources include a variety of sensor, control, and security wireless systems.

Straintronic heterostructures can also be used in microscale engines. They are magnetic particles in the form of a flat nickel ring 500 nm in diameter placed on a piezoelectric substrate (Fig. 45) [112, 237]. One of the metastable magnetic states of such a ring corresponds to 'onion'-shaped magnetization with two magnetic poles at two opposite points of the ring (Fig. 45a). Because the geometry of the magnetic ring does not imply any distinguished direction, the positions of the 'onion' poles can be easily changed by applying voltage across the piezosubstrate to induce magnetoelastic anisotropy in the ring. Six electrodes sequentially connected in pairs around the ring on the piezosubstrate allow the ring poles to be turned through 360° [112]. If a constant magnet is mounted on an axis orthogonal to the ring plane, the stray magnetic fields from the poles of the ring make it rotate to convert the electric energy into mechanical energy (Fig. 45b). Such flagella-driven microengines can be used for cell-targeted drug delivery, control of nanorobot movements, and other nanomedical applications (Fig. 45c) [273].

The design of miniature engines, as well as some straintronic sensors and energy harvesting devices, assumes the mechanical movements of their parts. Therefore, this area of straintronics tends to interlock with more advanced manufacturing industries making use of silicon microelectronics technologies, such as micro- and nanoelectromechanical systems (MEMSs and NEMSs).

3.4 Electric field-tunable devices processing radio signals

One of the promising areas of magnetic straintronics covers electrically operated microwave devices [274, 275]. The principle behind their operation is the induction of an effective magnetic anisotropy field in an FM layer by PE layer-generated strain. The uniaxial anisotropy field may considerably change the orientation of magnetic layer magnetization and thereby enable a controlled shift of the ferromagnetic resonance (FMR) frequency of the structure.

Figure 46 depicts a microwave resonator/filter tunable by electric and magnetic fields [275]. The resonator contains a PZT plate with a bonded epitaxial yttrium–iron garnet (YIG) film. The structure is placed in field H perpendicular to its

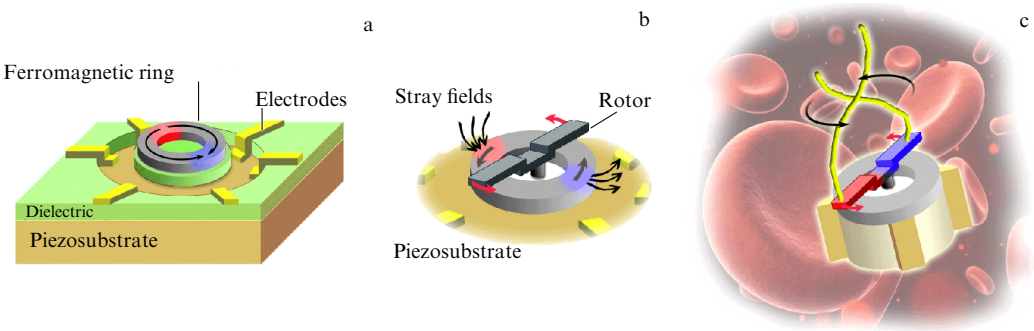

Figure 45. Microengines based on a ring-shaped straintronic heterostructure: (a) schematic of the structure, (b) rotor spinning upon displacement of ring magnetic poles, and (c) nanorobot for medical applications [273].

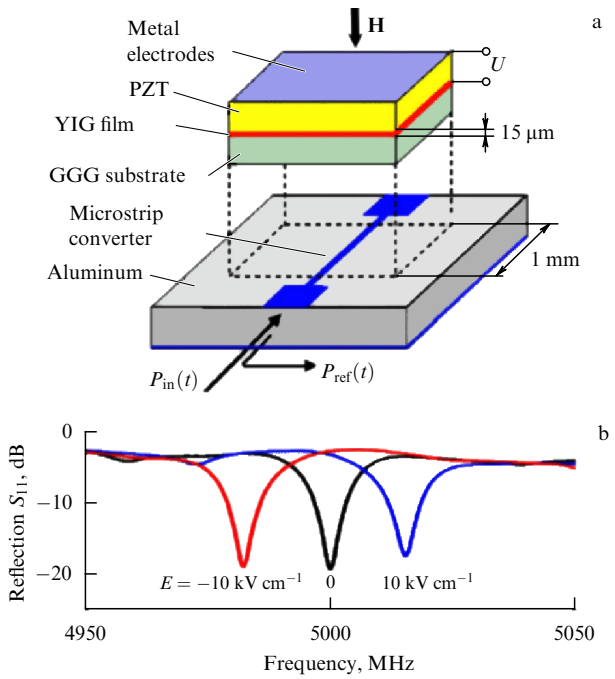

Figure 46. YIG–PZT-based microwave resonator tuned by electric and magnetic fields. (a) Device layout; GGG — gadolinium–gallium garnet, and (b) displacement of ferromagnetic resonance line under the effect of electric fields of various polarities.

plane. A microstrip converter excites FMR in the YIG film at frequency $f = \gamma(H - 4\pi M)$, where $\gamma = 2.8$ MHz Oe^{-1} and $4\pi M = 1750$ G are YIG gyromagnetic ratio and magnetization, respectively. The application of voltage across PZT electrodes deforms the plate, and the strain is transferred to the YIG film, which changes the anisotropy field and shifts the FMR frequency. The maximum bandwidth in which the resonator absorption line was tuned upon application of field $E = \pm 10$ kV cm^{-1} was much greater than the line width (47 MHz, i.e., $\sim 1\%$ of the central one). Simultaneously, this resonator can be tuned in a broad frequency range of 2–10 GHz (even if rather slowly) with a change in the external magnetizing field H. A similar effect of electric field tuning the FMR frequency was observed in structures with Ni-ferrite and Ba-hexaferrite films. For the FeGaB–PZN–PT structure, a record-breaking width of FMR frequency tuning (from 1.8 to 7.5 GHz) was achieved, with the electric field strength E varying from 0 to 8 kV cm^{-1} [223]. However, the width of an absorption line in all these materials is great compared with the YIG films, and microwave power absorption is insignificant, which limits their application.

An analogous composite structure containing a YIG film and two microstrip lines with an electrode-carrying PZT plate bonded between them can function as a controllable delay line [276] or a phase shifter [277]. A microwave signal is fed onto the input microstrip line to excite a spin wave of 10–100-μm wavelength, propagating over the YIG film. The microstrip line on the other side of the piezoelectric converts a spin wave into the output microwave signal. The electrodes on the 1-μm thick piezoelectric plate do not really influence wave propagation. The application of field E to the piezoelectric deforms the YIG film, alters microwave dispersion, and modulates delay time of the output microwave signal. In an experiment with the signal at a frequency of 3.6 GHz, an increase in E from 0 to 8 kV cm^{-1} reduced the delay time of the microwave signal by 1/3, from 180 to 120 ns. When this system was used in the phase-shifter regime, a registered change in the output signal phase under the effect of the same control field E amounted to 100°. The above microwave filters, delay lines, and phase shifters can also find applications in controllable generators, phased-array antennas, and other devices in which fast readjustment of microwave signal parameters is needed.

Miniaturization of straintronic devices for processing microwave signals opens up a new research area, magnon straintronics [278], in which magnetic dipole–dipole interaction between spin waves allows us to perform logical operations by electrically switching microwave radiation between microstrip channels. Interestingly, the absence of explicitly distinguished waveguides in a magnetic medium does not prevent inhomogeneous mechanical stress in a composite structure consisting of a piezoelectric and an yttrium–iron garnet film from forming the waveguide channels in the film along which spin waves propagate [279]; it gives additional degrees of freedom for designing electric field-tunable magnon devices.

3.5 The spin-offs of straintronics: gyrators, transtors, and neuromorphic elements

Straintronics provides an opportunity for considerable extension of the requisite components of conventional electronics. For example, magnetoelectric composite structures can be used to create a *gyrator* (from Greek 'gyros' — revolution), a device proposed by the American engineer B D H Tellegen in 1948 [225] and so named for the ability to invert impedance. Transformation of currents and voltages in a four-terminal network of this type obeys the following law:

$$\begin{pmatrix} v_1 \\ v_2 \end{pmatrix} = \begin{pmatrix} 0 & -R_g \\ R_g & 0 \end{pmatrix} \begin{pmatrix} i_1 \\ i_2 \end{pmatrix}, \tag{17}$$

where v_1 and v_2 are input and output voltages, respectively, i_1 and i_2 are the currents at the inlet and outlet, and R_g are nondiagonal elements of the gyrator resistance matrix (Fig. 47a).

Transformation (17) is equivalent to impedance inversion at the input and output:

$$Z_1 = \frac{R_g^2}{Z_2}, \tag{18}$$

where Z_1 and Z_2 are input and output impedances, respectively.

It follows from Eqn (18) that closed input terminals are equivalent to an infinite output impedance and that by loading the output of a gyrator with a low capacitor you can get a large equivalent inductance at the input.

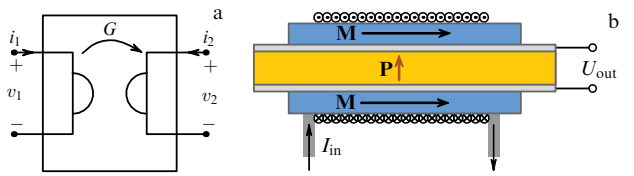

Figure 47. (a) Electric circuit diagram of Tellegen's gyrator [225]. (b) Engineering implementation of a composite-based gyrator [280].

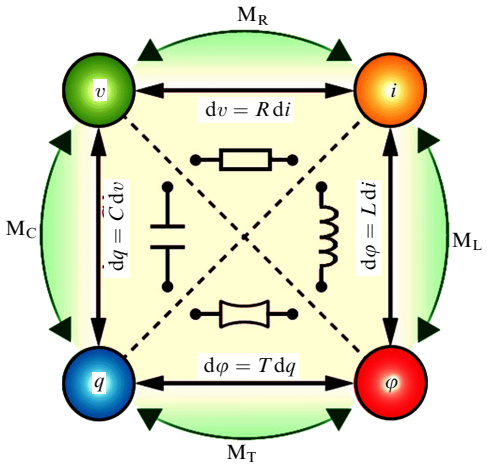

Figure 48. (Color online.) Diagrammatic representation of electronic two-pole elements: linear resistor, capacitor, and inductor are supplemented by the fourth element (*transtor*) [287]. Four main memory elements: M_R — memristor, M_C — memcapacitor, M_L — meminductor, and M_T — memtranstor.

Tellegen's original idea was to use a material with ME properties for manufacturing gyrators, but in 1948 such materials were purely hypothetical. As a result, designers of gyrator functions for electronics had to be content with an electric circuit on a feedback operational amplifier. The initial scheme designed by Tellegen (inductive and capacitive elements connected via an ME converter) could be implemented only in the 21st century [280, 281]. Current fed to the gyrator input creates a magnetic field that causes deformation of the magnetic core, which is converted into voltage across the terminals of the capacitive element with a piezoelectric filler (Fig. 47b).

In composite structures from Metglas and lead zirconate–titanate operating at the mechanical resonance frequency, the efficiency of conversion amounts to 90% in terms of power [282].

Tellegen's gyrator is considered to be the 'fifth element' of traditional electronics, in addition to the resistor, capacitor, inductor, and transformer. However, the transformer appears to be irrelevant on this list. It would be more logical to supplement the three main elements of electric circuits (resistor, capacitor, and inductor) by a fourth two-pole element (element T) (Fig. 48) and a linear characteristic complementing the former three (Fig. 49a–d). Indeed, resistance is defined in terms of the volt–ampere characteristic, capacitance connects electric charge with voltage, and inductance relates magnetic flux to electric current, but there is no element relating magnetic flux to charge.

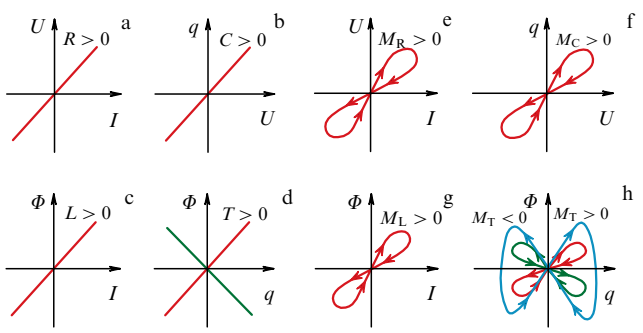

Figure 49. (Color online.) Characteristics of four linear elements: (a) resistor, (b) capacitor, (c) inductor, and (d) transtor, and respective nonlinear memory elements: (e) memristor, (f) memcapacitor, (g) meminductor, and (h) memtranstor (the butterfly-like trajectory is characteristic of large charge and flow values).

To address this problem, it was proposed in the early 1970s [283] to use derivatives of quantities in the consideration of the magnetic flux/charge characteristic, which is equivalent to the volt–ampere characteristic (on the assumption that the magnetic flux is converted into voltage by virtue of electromagnetic induction). In this case, the nontrivial fourth element has to be a resistor with a nonlinear, hysteretic relationship between voltage and current, i.e., a memory resistor, or *memristor* [283]. The memory effect for the resistor is realized by the transposition of oxygen vacancies, e.g., in semiconducting titanium oxide-based structures [284], or by altering the structure of ferroelectric domain boundaries in multiferroic bismuth ferrite [285]. It has been recently revealed that the nonuniform distribution of mechanical strains in voltage-controlled vertically aligned carbon nanotubes also produces the memristive effect [286], which opens up new prospects in straintronics.

Turning back to the original definition of the fourth element, it is impossible not to notice that the introduction of the memristor does not solve the initial problem of finding a *linear* element relating magnetic flux to charge. Such a linkage could be realized in an ME composite-based straintronic device in which magnetization is induced by a constant electric field. To distinguish a memristor from the fourth linear element, the authors of a recent publication [287] propose to call it the '*transtor*'.

The same authors also attempted to update the classification scheme of nonlinear elements in which the nonlinear element memristor remains a resistor with a memory to which the memcapacitor, meminductor, and memtranstor correspond (indicated in Fig. 48 by green arrows and the letter M with subscripts L, R, C, T). Characteristics of such elements exhibit a hysteretic character (Fig. 49e–h).

A memtranstor, like a memristor [288], can be utilized in so-called *neuromorphic electronics*, where electric circuits are believed to reproduce the function of the neural network, the role of neurons being performed by usual semiconductor transistors and that of synapses (connections between neurons) by memory elements. It was shown in memristor studies [288] that memory elements have a property analogous to synaptic plasticity, i.e., a mechanism that enables neural networks to learn by multiply strengthening interneuron connectivity.

Straintronic elements can function not only as synapses but also as neurons [8] (Fig. 50). Synapses are formed by a set of input resistors, where each current is combined with its weight, depending on resistor value. A straintronic element based on a magnetoresistive sandwich structure (see inset to Fig. 50), similar to those considered in Section 3.2, produces a nonlinear response with a stepwise transient characteristic: voltage across A and A′ electrodes representing the superposition of signals from 'synapses' creates mechanical stress in the piezoelectric substrate that switches magnetization of the magnetically soft layer in the sandwich structure and abruptly changes its resistance.

Numerical simulation shows that such straintronic elements allow not only radically decreasing the power consumed to a level competitive with that attainable in semi-

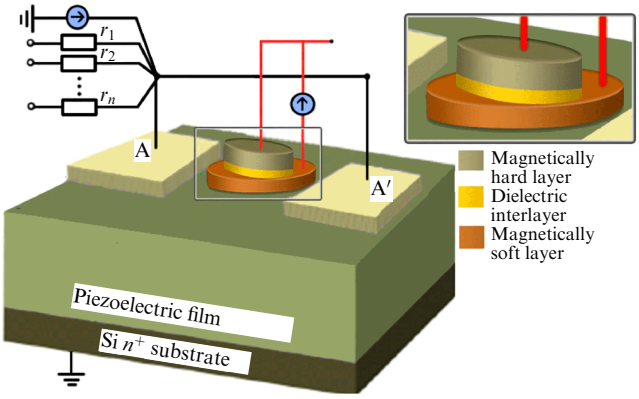

Figure 50. Straintronic element of artificial neural networks: tunneling magnetoresistor-based reading element (the insert shows a magnified view) lies on a piezoelectric substrate (strongly doped silicon layer) [8].

conductor electronics, but also making the transient characteristic much closer to the step pattern by diminishing the effect of thermal noises that blur the front [8].

It can be concluded that an obvious advantage of straintronic elements in the form of memory cells and logical devices is their record-breaking low energy consumption for both recording [5] and reading out [128] information. They meet modern requirements as to switching time but are slightly inferior to their best semiconductor counterparts. Another drawback of straintronic devices is their relatively low packaging density. Still, they find a variety of applications where a miniature size and high operation speed are of less significance than low energy consumption and operational reliability at near-room temperatures, as in mobile electronics, medical implanted processors and wearables, and wireless remote sensing systems.

4. Conclusion

To sum up, it can be concluded that current progress in straintronics is to a large extent based on achievements in semiconductor and magnetic technologies. Thus, the possibility of mechanically induced changing the semiconductor band structure in strain sensors [10] began to be used since the mid-20th century, and the application of strain engineering techniques for manufacturing helicoidal spin structures in antiferromagnets had been reported much before the term 'straintronics' was coined [62].

Magnetic straintronics emerged at the interface between spin electronics and the physics of magnetoelectric materials after its major advantage (low energy of switching between two logical states) over existing technologies had been appreciated [5]. From the standpoint of energy saving, straintronic devices offer some benefits in comparison with spintronic recording systems based on spin-transfer torque and even tunneling magnetoresistive readout heads [128].

Fundamental challenges have played an equally important role in the development of straintronics. Thus, symmetry prohibition on 180-degrees switching of magnetization and methods to circumvent it were considered in many straintronics studies discussed in detail in Section 2.1, although this issue is not very important from a practical point of view. Ninety-degrees magnetization switching schemes are equally feasible. At the same time, little attention is given to such obvious drawback of straintronic technologies as the relatively large switching time. Even in theoretical calculations intended to illustrate 'fast 180-degrees switching' [101], magnetization relaxation times are several nanoseconds in the absence of explicitly formulated constraints on operation speed. A comparison with the results of work on ultrafast magnetism [25, 289, 290] gives evidence to talk that switching times on the order of 1 ns, reported in publications concerned with modeling straintronic devices, leave the reserve of a few orders of magnitude for their further reduction. Thus far, the most straintronic-friendly applications have been those that do not require ultrahigh operation speed (magnetic field sensors, transformers, and autonomous low-power energy harvesting generators) (see Section 3.3); other promising fields are implantology (17), nanomedicine [273], and other medical applications. The employment of technologies for manufacturing micro- and nano-electromechanical systems may give an additional impetus to developments in this field of low-frequency electronics.

A breakthrough in the area of high-frequency switching may well come from technologies at the intersection of photonics and straintronics that can be termed light-mediated straintronics [9] or photostraintronics. Photo-excited striction in ferroelectric materials and multiferroics brings the switching rate of straintronic elements into the terahertz frequency range [52].

Finally, elastic gauge fields in inhomogeneously strained graphene (see Section 1.3) are of great theoretical interest, since they provide a basis for physical simulation of electron behavior in strong (a few hundred teslas) magnetic fields [7]. Research activities in this field are just gathering momentum and await dedicated investigators.

Acknowledgments

This study was supported by grants 16-29-14037 and 16-29-14017 from the Russian Foundation for Basic Research (RFBR) for topic 614, "Straintronics as a platform for the development of a new generation of information processing devices." Studies based at Zavoisky Kazan Physical-Technical Institute of the Federal Research Center 'Kazan Scientific Centre of the Russian Academy of Sciences,' were supported by RFBR grants 15-02-02728 and 18-02-00204, and those carried out at the MIREA — Russian Technological University by the Ministry of Education and Science of the Russian Federation (project No. 8.1183.2017/PCh). The participation of A P P and A K Z was supported by RFBR grant 16-02-00494.

The authors are grateful to D A Bizyaev, N A Nurgazizov, S A Ziganshina, P A Chuklanov, and T F Khanipov for their cooperation, and O A Tyshova for her interest in this work and valuable comments. Special thanks are due to Z A Pyatakova for help with the illustrations.

References

1. Ramesh R, in *CMD26, The 26th Conf. of the Condensed Matter Division, 4–9 September, 2016, Gröningen, Netherlands* (Mulhouse: European Physical Society, 2016) p. 19/3A
2. Atanasov V, Saxena A *J. Phys. Condens. Matter* **23** 175301 (2011)
3. Pyatakov A P, Zvezdin A K *Phys. Usp.* **52** 557 (2012); *Usp. Fiz. Nauk* **182** 593 (2012)
4. Bichurin M, Viehland D *Magnetoelectricity in Composites* (Singapore: Pan Stanford Publ., 2011); Bichurin M I et al. *Magnitoelektricheskii Effekt v Kompozitsionnykh Materialakh* (Magnetoelectric Effect in Composite Materials) (Velikii Novgorod: Izd. NovGU, 2005)

5. Roy K, Bandyopadhyay S, Atulasimha J *Appl. Phys. Lett.* **99** 063108 (2011)
6. Shiri D et al. *Sci. Rep.* **2** 461 (2012)
7. Si C, Sun Z, Liu F *Nanoscale* **8** 3207 (2016)
8. Biswas A K, Atulasimha J, Bandyopadhyay S *Nanotechnology* **26** 285201 (2015)
9. Iurchuk V et al. *Phys. Rev. Lett.* **117** 107403 (2016)
10. Smith C S *Phys. Rev.* **94** 42 (1954)
11. Heine T *Acc. Chem. Res.* **48** 65 (2015)
12. Bhattacharyya S, Pandey T, Singh A K *Nanotechnology* **25** 465701 (2014)
13. Zibouche N et al. *Ann. Physik* **526** 395 (2014)
14. Wei W, Dai Y, Huang B *Phys. Chem. Chem. Phys.* **19** 663 (2017)
15. Cortijo A et al. *2D Mater.* **3** 11002 (2016)
16. Roy K *Proc. SPIE* **9167** 91670U (2014)
17. Yilmaz Y, Mazumder P *IEEE Trans. Very Large Scale Integr. Syst.* **21** 1181 (2013)
18. Roy K *IEEE Trans. Nanotechnol.* **16** 333 (2017)
19. Nikonov D E, Young I A *J. Mater. Res.* **29** 2109 (2014)
20. Ngo D-T, Duc N H, in *Advanced Magnetism and Magnetic Materials* Vol. 2 *Aspects of Magneto-Electrostructive Materials and Applications* Ch. 3 (Hanoi: Vietnam National Univ. Press, 2015) p. 274
21. Iurchuk V, Doudin B, Kundys B *J. Phys. Condens. Matter* **26** 292202 (2014)
22. Ahmad H, Atulasimha J, Bandyopadhyay S *Nanotechnology* **26** 401001 (2015)
23. D'Souza N et al. *Nano Lett.* **16** 1069 (2016)
24. Salehi-Fashami M et al. *Nanotechnology* **27** 43LT01 (2016)
25. Stupakiewicz A et al. *Nature* **542** 71 (2017)
26. Borovik-Romanov A S *Lektsii po Nizkotemperaturnomu Magnetizmu*: *Magnitnaya Simmetriya Antiferromagnetikov* (Lectures on Low-Temperature Magnetism: Magnetic Symmetry of Antiferromagnets) (Novosibirsk: Novosibirskii Gos. Univ., 1976)
27. Zvezdin A K et al. *Sov. Phys. JETP* **61** 645 (1985); *Zh. Eksp. Teor. Fiz.* **88** 1098 (1985)
28. van Suchtelen J *Philips Res. Rep.* **27** 28 (1972)
29. Zubko P, Catalan G, Tagantsev A K *Annu. Rev. Mater. Res.* **43** 387 (2013)
30. Eliseev E A et al. *Phys. Rev. B* **79** 165433 (2009)
31. Lukashev P, Sabirianov R F *Phys. Rev. B* **82** 094417 (2010)
32. Eliseev E A et al. *Phys. Rev. B* **84** 174112 (2011)
33. Hertel R *Spin* **03** 1340009 (2013)
34. Lee J H et al. *Phys. Rev. B* **96** 064402 (2017)
35. Pyatakov A P, Meshkov G A, Zvezdin A K *J. Magn. Magn. Mater.* **324** 3551 (2012)
36. Streubel R et al. *J. Phys. D* **49** 363001 (2016)
37. Pyatakov A P, Zvezdin A K *Eur. Phys. J. B* **71** 419 (2009)
38. Tanygin B M *J. Magn. Magn. Mater.* **323** 1899 (2011)
39. Kabychenkov A F, Lisovskii F V *JETP* **118** 643 (2014); *Zh. Eksp. Teor. Fiz.* **145** 733 (2014)
40. Cheong S-W, Mostovoy M *Nature Mater.* **6** 13 (2007)
41. Bar'yakhtar V G, L'vov V A, Yablonskii D A *JETP Lett.* **37** 673 (1983); *Zh. Eksp. Teor. Fiz.* **37** 565 (1983)
42. Logginov A S et al. *JETP Lett.* **86** 115 (2007); *Pis'ma Zh. Eksp. Teor. Fiz.* **86** 124 (2007)
43. Pyatakov A P et al. *Phys. Usp.* **58** 981 (2015); *Usp. Fiz. Nauk* **185** 1077 (2015)
44. Kabychenkov A F, Lisovskii F V, Mansvetova E G *JETP Lett.* **97** 265 (2013); *Pis'ma Zh. Eksp. Teor. Fiz.* **97** 304 (2013)
45. Arzamastseva G V et al. *JETP* **120** 687 (2015); *Zh. Eksp. Teor. Fiz.* **147** 793 (2015)
46. Sparavigna A, Strigazzi A, Zvezdin A *Phys. Rev. B* **50** 2953 (1994)
47. Zvezdin A K, Pyatakov A P *Europhys. Lett.* **99** 57003 (2012)
48. Zvezdin A K *Bull. Lebedev Phys. Inst.* (4) 5 (2002); *Kratk. Soobshch. Fiz. Fiz. Inst. Ross. Akad. Nauk* (4) 7 (2002)
49. Bode M et al. *Nature* **447** 190 (2007)
50. Pyatakov A P, Zvezdin A K *Europhys. Lett.* **107** 67002 (2014)
51. Kundys B et al. *Nature Mater.* **9** 803 (2010)
52. Lejman M et al. *Nature Commun.* **5** 4301 (2014)
53. Ding F et al. *Nano Lett.* **10** 3453 (2010)
54. Ong M T, Reed E J *ACS Nano* **6** 1387 (2012)
55. Guan F, Du X *Nano Lett.* **17** 7009 (2017)
56. Ferralis N, Maboudian R, Carraro C *Phys. Rev. Lett.* **101** 156801 (2008)
57. Yoon D, Son Y-W, Cheong H *Nano Lett.* **11** 3227 (2011)
58. Lee M-S et al. *Nano Res.* **8** 2082 (2015)
59. Singh J *Superlatt. Microstruct.* **8** 225 (1990)
60. Banerjee S K *Proc. SPIE* **3212** 118 (1997)
61. Guffarth F et al. *Phys. Rev. B* **64** 085305 (2001)
62. Giebultowicz T M et al. *Phys. Rev. B* **46** 12076(R) (1992)
63. Collins M, Saslow W M *Phys. Rev. B* **53** 8533 (1996)
64. Haeni J H et al. *Nature* **430** 758 (2004)
65. Posadas A B et al., in *Physics of Ferroelectrics. A Modern Perspective* (Topics in Applied Physics, Vol. 105, Eds K M Rabe, Ch H Ahn, J-M Triscone) (Berlin: Springer, 2007) p. 219; Translated into Russian: in *Fizika Segnetoelektrikov. Sovremennyi Vzglyad* (Eds B Strukov, A Lebedev) (Moscow: Binom, 2015) p. 308
66. Gui G, Li J, Zhong J *Phys. Rev. B* **78** 075435 (2008)
67. Pereira V M, Castro Neto A H *Phys. Rev. Lett.* **103** 046801 (2009)
68. Loshkarev I D et al. *Bull. Russ. Acad. Sci.* **77** 233 (2013); *Izv. Ross. Akad. Nauk. Fiz.* **77** 264 (2013)
69. Trukhanov E M et al. *Bull. Russ. Acad. Sci.* **78** 307 (2014); *Izv. Ross. Akad. Nauk. Fiz.* **78** 472 (2014)
70. Levy N et al. *Science* **329** 544 (2010)
71. Akbashev A R, Kaul A R *Russ. Chem. Rev.* **80** 1159 (2011); *Usp. Khim.* **80** 1211 (2011)
72. Chuklanov A P et al. *J. Phys. Conf. Ser.* **714** 12006 (2016)
73. Yu T et al. *J. Phys. Chem. C* **112** 12602 (2008)
74. Li X et al. *Sci. Rep.* **2** 870 (2012)
75. Bousige C et al. *Nano Lett.* **17** 21 (2017)
76. Salary M M et al. *Phys. Rev. B* **94** 235403 (2016)
77. Kartavtseva M S et al. *Thin Solid Films* **518** 4750 (2010)
78. Ramesh R, Spaldin N A *Nature Mater.* **6** 21 (2007)
79. Bolkhovityanov Yu B, Pchelyakov O P, Chikichev S I *Phys. Usp.* **44** 655 (2001); *Usp. Fiz. Nauk* **171** 689 (2001)
80. Guinea F, Katsnelson M I, Geim A K *Nature Phys.* **6** 30 (2010)
81. Wu Y et al. *Nano Lett.* **18** 64 (2018)
82. Newnham R E, Skinner D P, Cross L E *Mat. Res. Bull.* **13** 525 (1978)
83. Khvalkovskiy A V et al. *J. Phys. D* **46** 74001 (2013)
84. Wang Z et al. *ACS Nano* **8** 7793 (2014)
85. Khan A et al. *Appl. Phys. Lett.* **104** 262407 (2014)
86. Huang H B et al. *Appl. Phys. Lett.* **105** 122407 (2014)
87. Gopman D B et al. *Sci. Rep.* **6** 27774 (2016)
88. Parkin S S P, Hayashi M, Thomas L *Science* **320** 190 (2008)
89. Bauer U, Emori S, Beach G S D *Nature Nanotechnol.* **8** 411 (2013)
90. Kang W et al. *Sci. Rep.* **6** 23164 (2016)
91. Varvaro G, Casoli F *Ultra-High-Density Magnetic Recording. Storage Materials and Media Designs* (New York: CRC Press, 2016)
92. Salahuddin S, Datta S *Appl. Phys. Lett.* **90** 093503 (2007)
93. Atulasimha J, Bandyopadhyay S *Nanomagnetic and Spintronic Devices for Energy-Efficient Memory and Computing* (New York: J. Wiley, 2016)
94. Tannous C, Gieraltowski J *Eur. J. Phys.* **29** 475 (2008)
95. Atulasimha J, Bandyopadhyay S *Appl. Phys. Lett.* **97** 173105 (2010)
96. Fashami M S, Atulasimha J, Bandyopadhyay S *Nanotechnology* **23** 105201 (2012)
97. Barangi M, Mazumder P *IEEE Nanotechnol. Mag.* **9** 15 (2015)
98. Roy K, Bandyopadhyay S, Atulasimha J *Phys. Rev. B* **83** 224412 (2011)
99. Buzzi M et al. *Phys. Rev. Lett.* **111** 027204 (2013)
100. Roy K, Bandyopadhyay S, Atulasimha S *Sci. Rep.* **3** 3038 (2013)
101. Peng R-C et al. *Sci. Rep.* **6** 27561 (2016)
102. Yi M et al. *Acta Mech.* https://doi.org/10.1007/s00707-017-2029-7 (2017)
103. Roy K, Bandyopadhyay S, Atulasimha J *J. Appl. Phys.* **112** 023914 (2012)
104. Tiercelin N et al. *J. Appl. Phys.* **109** 07D726 (2011)
105. Giordano S et al. *Phys. Rev. B* **85** 155321 (2012)
106. Liang C-Y et al. *J. Appl. Phys.* **116** 123909 (2014)
107. Biswas A K, Bandyopadhyay S, Atulasimha J *Appl. Phys. Lett.* **104** 232403 (2014)
108. Liang C-Y et al. *J. Appl. Phys.* **119** 113903 (2016)
109. Biswas A K, Bandyopadhyay S, Atulasimha J *Appl. Phys. Lett.* **105** 072408 (2014)
110. Wang J J et al. *Sci. Rep.* **4** 7507 (2014)

111. Peng R-C et al. *Appl. Phys. Lett.* **106** 142901 (2015)
112. Liang C-Y et al. *J. Appl. Phys.* **118** 174101 (2015)
113. Biswas A K, Bandyopadhyay S, Atulasimha J *Appl. Phys. Lett.* **103** 232401 (2013)
114. Kovalenko O, Pezeril T, Temnov V V *Phys. Rev. Lett.* **110** 266602 (2013)
115. Khan A et al. *Appl. Phys. Lett.* **104** 262407 (2014)
116. Fashami M S et al. *Nanotechnology* **22** 155201 (2011)
117. Behin-Aein B, Salahuddin S, Datta S *IEEE Trans. Nanotechnol.* **8** 505 (2009)
118. Barangi M, Mazumder P *J. Appl. Phys.* **118** 173902 (2015)
119. Madami M et al. *J. Phys. D* **50** 453002 (2017)
120. Gilbert T L *IEEE Trans. Magn.* **40** 3443 (2004)
121. Brown W F (Jr.) *Phys. Rev.* **130** 1677 (1963)
122. Cui H et al. *J. Phys. D* **50** 285001 (2017)
123. Roy K, Bandyopadhyay S, Atulasimha J *J. Appl. Phys.* **112** 023914 (2012)
124. Hu J-M et al. *Nano Lett.* **15** 616 (2015)
125. Li X et al. *J. Appl. Phys.* **118** 014101 (2015)
126. Biswas A K et al. *Nano Lett.* **17** 3478 (2017)
127. Wang K L, Alzate J G, Khalili Amirim P *J. Phys. D* **46** 74003 (2013)
128. Klimov A et al. *Appl. Phys. Lett.* **110** 222401 (2017)
129. Ahmad H, Atulasimha J, Bandyopadhyay S *Sci. Rep.* **5** 18264 (2015)
130. Sampath V et al. *Nano Lett.* **16** 5681 (2016)
131. Liu Y et al. *IEEE Trans. Magn.* **51** 2501404 (2015)
132. Buravikhin V A *Vliyanie Mekhanicheskikh Napryazhenii na Magnitnye Svoistva Plenok* (The Influence of Mechanical Stresses on Magnetic Properties of Films) (Irkutsk: Vostochno-Sibirskoe Knizhnoe Izd., 1968)
133. Belyaev B A, Izotov A V *Phys. Solid State* **49** 1731 (2007); *Fiz. Tverd. Tela* **49** 1651 (2007)
134. Dai G et al. *Appl. Phys. Lett.* **100** 122407 (2012)
135. Dai G et al. *J. Appl. Phys.* **114** 173913 (2013)
136. Kumar D et al. *J. Magn. Magn. Mater.* **418** 99 (2016)
137. Wu T et al. *IEEE Magn. Lett.* **2** 6000104 (2011)
138. Hao Z et al. *Chin. Phys. B* **24** 77501 (2015)
139. Bizyaev D A et al. *Tech. Phys. Lett.* **42** 1034 (2016); *Pis'ma Zh. Tekh. Fiz.* **42** (20) 24 (2016)
140. Bur A et al. *J. Appl. Phys.* **109** 123903 (2011)
141. Bizyaev D A, Bukharaev A A, Nurgazizov N I, Khanipov T F *J. Phys. Conf. Ser.* **859** 012005 (2017)
142. Foerster M et al., arXiv:1611.02847
143. Cullity B D, Graham C D *Introduction to Magnetic Materials* (New York: John Wiley and Sons, 2008)
144. Zabel H, Farle M (Eds) *Magnetic Nanostructures. Spin Dynamics and Spin Transport* (Berlin: Springer-Verlag, 2013)
145. Donahue M J, Porter D G "Object oriented micromagnetic framework (OOMMF)", http://math.nist.gov/oommf/
146. Ovchinnikov D V, Bukharaev A A *Tech. Phys.* **46** 1014 (2001); *Zh. Tekh. Fiz.* **71** 85 (2001)
147. Bukharaev A A et al., in *Materialy XX Mezhdunarodhogo Simpoziuma 'Nanofizika i Nanoelektronika', Nizhnii Novgorod, 14–18 Marta 2016* (Proc. of the XX Intern. Symp. "Nanophysics and Nanoelectronics", Nizhny Novgorod, March 14 – 18, 2016) (Nizhny Novgorod: Izd. Nizhegorodskogo Gos. Univ., 2016) p. 277
148. Finizio S et al. *Phys. Rev. Appl.* **1** 021001 (2014)
149. Chung T-K, Carman G P, Mohanchandra K P *Appl. Phys. Lett.* **92** 112509 (2008)
150. Brintlinger T et al. *Nano Lett.* **10** 1219 (2010)
151. Parkes D E et al. *Appl. Phys. Lett.* **101** 072402 (2012)
152. Arzamastseva G V et al. *JETP* **120** 687 (2015); *Zh. Eksp. Teor. Fiz.* **147** 793 (2015)
153. Lei N et al. *Nature Commun.* **4** 1378 (2013)
154. Fontcuberta J et al. *Sci. Rep.* **5** 13784 (2015)
155. Lahtinen T H E, Franke K J A, van Dijken S *Sci. Rep.* **2** 258 (2012)
156. Franke K J A et al. *Phys. Rev. X* **5** 011010 (2015)
157. Gareeva Z V et al. *Phys. Status Solidi Rapid Res. Lett.* **10** 209 (2016)
158. Belashchenko K D et al. *Appl. Phys. Lett.* **108** 132403 (2016)
159. Malozemoff A P, Slonczewski J C *Magnetic Domain Walls in Bubble Materials* (New York: Academic Press, 1979)
160. Nii Y et al. *Nature Commun.* **6** 8539 (2015)
161. Kulikova D P et al. *JETP Lett.* **104** 197 (2016); *Pis'ma Zh. Eksp. Teor. Fiz.* **104** 196 (2016)
162. Hsu P et al. *Nature Nanotechnol.* **12** 123 (2016)
163. Koretsune T, Nagaosa N, Arita R *Sci. Rep.* **5** 13302 (2015)
164. Kim H K D et al. *Nano Lett.* **13** 884 (2013)
165. Mishina E D et al. *Ferroelectrics* **500** 37 (2016)
166. Sando D et al. *Nature Mater.* **12** 641 (2013)
167. Popov Yu F et al. *JETP Lett.* **57** 69 (1993); *Pis'ma Zh. Eksp. Teor. Fiz.* **57** 65 (1993)
168. Zalesskii A V et al. *JETP* **95** 101 (2002); *Zh. Eksp. Teor. Fiz.* **122** 116 (2002)
169. Wu J et al. *Prog. Mater. Sci.* **84** 335 (2016)
170. Kadomtseva A M et al. *Phase Trans.* **79** 1019 (2006)
171. Tokunaga M, Azuma M, Shimakawa Y *J. Phys. Soc. Jpn.* **79** 64713 (2010)
172. Kadomtseva A M, Popov Y F, Vorob'ev G P, Zvezdin A K *Physica B* **211** 327 (1995)
173. Gareeva Z V, Popkov A F, Soloviov S V, Zvezdin A K *Phys. Rev. B* **87** 214413 (2013)
174. Tehranchi M-M, Kubrakov N F, Zvezdin A K *Ferroelectrics* **204** 181 (1997)
175. Rusakov V S et al. *Dokl. Phys.* **63** 223 (2018); *Dokl.Ross. Akad. Nauk* **480** 657 (2018); in *Moscow Intern. Symp. on Magnetism, 1–5 July 2017. Book of Abstracts* (Eds N Perov et al.) (Moscow: Faculty of Physics M V Lomonosov MSU, 2017) p. 914
176. Kawachi S et al. *Phys. Rev. Mater.* **1** 024408 (2017)
177. Wang J et al. *Science* **299** 1719 (2003)
178. Bai F et al. *Appl. Phys. Lett.* **86** 32511 (2005)
179. Agbelele A et al. *Adv. Mater.* **112** 1602327 (2016)
180. Lazenka V et al. *Appl. Phys. Lett.* **106** 12 (2015)
181. Popkov A F et al. *Phys. Rev. B* **93** 094435 (2016)
182. He Q et al. *Nature Commun.* **2** 225 (2011)
183. Cheng C-E et al. *Sci. Rep.* **5** 8091 (2015)
184. Sando D et al. *Nature Commun.* **7** 10718 (2016)
185. Prellier W, Singh M P, Murugavel P *J. Phys. Condens. Matter* **17** R803 (2005)
186. Lee J H et al. *Nature* **466** 954 (2010)
187. White J S et al. *Phys. Rev. Lett.* **111** 037201 (2013)
188. Fiebig M et al. *Nature Rev. Mater.* **1** 16046 (2016)
189. López-Ruiz R et al. *J. Appl. Phys.* **112** 073906 (2012)
190. Kumar A et al. *Phys. Rev. B* **73** 064421 (2006)
191. Zeng H et al. *J. Phys. Condens. Matter* **14** 715 (2002)
192. Vazquez M et al. *J. Magn. Magn. Mater.* **294** 174 (2005)
193. Paulus P M et al. *J. Magn. Magn. Mater.* **224** 180 (2001)
194. Taniyama T et al. *J. Appl. Phys.* **105** 07D901 (2009)
195. Sahoo S et al. *Phys. Rev. B* **76** 092108 (2007)
196. Venkataiah G et al. *J. Appl. Phys.* **111** 033921 (2012)
197. Pan M et al. *J. Phys. D* **46** 055001 (2013)
198. Ilinskiy A V, Kvashenkina O E, Shadrin E B *Semiconductors* **46** 422 (2012); *Fiz. Tekh. Poluprovodn.* **46** 439 (2012)
199. Shadrin E B, Il'inskii A V *Phys. Solid State* **42** 1126 (2000); *Fiz. Tverd. Tela* **42** 1092 (2000)
200. de la Venta J et al. *Appl. Phys. Lett.* **102** 122404 (2013)
201. de la Venta J et al. *Appl. Phys. Lett.* **104** 062410 (2014)
202. Blinov L M et al. *Phys. Usp.* **43** 243 (2000); *Usp. Fiz. Nauk* **170** 247 (2000)
203. Chang H H S, Whatmore R W, Huang Z *J. Appl. Phys.* **106** 114110 (2009)
204. Liu Y et al. *Sci. Rep.* **4** 6615 (2014)
205. Liu Y et al. *Sci. Rep.* **4** 6925 (2014)
206. Golenishchev-Kutuzov A V, Golenishchev-Kutuzov V A, Kalimullin R I *Phys. Usp.* **43** 647 (2000); *Usp. Fiz. Nauk* **170** 697 (2000)
207. Deev V N, Pyatakov P A *Pis'ma Zh. Tekh. Fiz.* **11** 76 (1985)
208. Wang Y et al. *J. Alloys Comp.* **513** 242 (2012)
209. Sreenivasulu G et al. *Appl. Phys. Lett.* **100** 052901 (2012)
210. Greve H et al. *Appl. Phys. Lett.* **96** 182501 (2010)
211. Sreenivasulu G et al. *Phys. Rev. B* **86** 214405 (2012)
212. Martins P, Martins P, Lanceros-méndez S *Adv. Funct. Mater.* **23** 3371 (2013)
213. Kulkarni A et al. *Appl. Phys. Lett.* **22904** 022904 (2014)
214. Kirchhof C et al. *Appl. Phys. Lett.* **102** 232905 (2013)
215. Li M et al. *Appl. Phys. Lett.* **100** 132904 (2012)
216. Lou J et al. *Appl. Phys. Lett.* **100** 102907 (2012)
217. Burdin D A et al. *J. Magn. Magn. Mater.* **358 – 359** 98 (2014)
218. Bichurin M I et al. *Phys. Rev. B* **68** 132408 (2003)

219. Filippov D A, Laletsin U, Srinivasan G *J. Appl. Phys.* **102** 93901 (2007)
220. Kamentsev K E, Fetisov Y K *Appl. Phys. Lett.* **89** 142510 (2006)
221. Burdin D A et al. *J. Appl. Phys.* **113** 33902 (2013)
222. Fetisov Y K, Fetisov L Y, Srinivasan G *Appl. Phys. Lett.* **94** 132507 (2009)
223. Lou J et al. *Adv. Mater.* **21** 4711 (2009)
224. Sun N X, Srinivasan G *Spin* **2** 1240004 (2012)
225. Tellegen B D H *Philips Res. Rep.* **3** 81 (1948)
226. Zvezdin A K, Logginov A S, Meshkov G A, Pyatakov A P *Bull. Russ. Acad. Sci. Phys.* **71** 1561 (2007); *Izv. Ross. Akad. Nauk. Fiz.* **71** 1604 (2007)
227. Catalan G, Scott J F *Adv. Mater.* **21** 2463 (2009)
228. Vopson M M *Crit. Rev. Solid State Mater. Sci.* **40** 223 (2015)
229. Palneedi H et al. *Actuators* **5** 9 (2016)
230. Srinivasan G, Priya S, Sun N *Composite Magnetoelectrics: Materials, Structures, and Applications* (Boston, MA: Elsevier, 2015)
231. Morosov A I *Phys. Solid State* **56** 865 (2014); *Fiz. Tverd. Tela* **56** 833 (2014)
232. Amelichev V, Belyakov P, Vasilyev D *Int. J. Environ. Sci. Educ.* **11** 10923 (2016)
233. Chen A T, Zhao Y G *APL Mater.* **4** 032303 (2016)
234. Li P et al. *Adv. Mater.* **26** 4320 (2014)
235. Manasi S D et al. *IEEE Trans. Electron Dev.* **64** 2842 (2017)
236. Tiercelin N et al. *Appl. Phys. Lett.* **99** 192507 (2011)
237. Hockel J L et al. *Appl. Phys. Lett.* **100** 022401 (2012)
238. Fashami M S et al. *Nanotechnology* **22** 155201 (2011)
239. Amiri P K, Wang K L *Spin* **02** 1240002 (2012)
240. Liu L et al. *Science* **336** 555 (2012)
241. Bhowmik D, You L, Salahuddin S *Nature Nanotechnol.* **9** 59 (2014)
242. Roy K *Sci. Rep.* **5** 10822 (2015)
243. Parkin S S P et al. *Nature Mater.* **3** 862 (2004)
244. Dusch Y et al. *J. Appl. Phys.* **113** 17C719 (2013)
245. Preobrazhensky V et al. *J. Magn. Magn. Mater.* **459** 66 (2018)
246. Shi Z, Wang C, Liu X, Nan C *Chinese Sci. Bull.* **53** 2135 (2008)
247. Zhao Z et al. *Appl. Phys. Lett.* **109** 092403 (2016)
248. Biswas A K, Atulasimha J, Bandyopadhyay S *Sci. Rep.* **4** 7553 (2014)
249. Munira K et al. *Nanotechnology* **26** 245202 (2015)
250. Fashami M S et al. *IEEE Trans. Nanotechnol.* **12** 1206 (2013)
251. Bennet C H *Int. J. Theor. Phys.* **21** 905 (1982)
252. Abeed M A et al. *IEEE Trans. Electron Dev.* **64** 2417 (2017)
253. Scott J F *J. Mater. Chem.* **22** 4567 (2012)
254. Wang Y, Li J, Viehland D *Mater. Today* **17** 269 (2014)
255. Priya S et al. *Sensors* **9** 6362 (2009)
256. Yarar E et al. *Appl. Phys. Lett.* **109** 022901 (2016)
257. Zhang Y et al. *Appl. Phys. Lett.* **92** 152510 (2008)
258. Nan T et al. *Nature Commun.* **8** 296 (2017)
259. Petrie J et al. *J. Appl. Phys.* **110** 124506 (2011)
260. Gillette S M et al. *IEEE Magn. Lett.* **2** 2500104 (2011)
261. Jahns R et al. *Sensors Actuators A* **183** 16 (2012)
262. Fetisov Y K et al. *IEEE Sens. J.* **14** 2252 (2014)
263. Kamentsev K E, Fetisov Y K, Srinivasan G *Tech. Phys.* **52** 727 (2007); *Zh. Tekh. Fiz.* **77** 50 (2007)
264. Burdin D et al. *J. Phys. D* **49** 375002 (2016)
265. Serov V N, Fetisov Y K, Shestakov E I *Ross. Tekhnol. Zh.* **4** (5) 24 (2016)
266. Gojdka B et al. *Appl. Phys. Lett.* **99** 223502 (2011)
267. Nan T et al. *Sci. Rep.* **3** 1985 (2013)
268. Sukhorukov Yu P et al. *JETP Lett.* **104** 384 (2016); *Pis'ma Zh. Eksp. Teor. Fiz.* **104** 398 (2016)
269. Dong S et al. *Appl. Phys. Lett.* **85** 3534 (2004)
270. Bayrashev A et al. *Sensors Actuators* **114** 244 (2004)
271. Dong S et al. *Appl. Phys. Lett.* **93** 103511 (2008)
272. Ryu J et al. *Energy Environ. Sci.* **8** 2402 (2015)
273. Hockel J L, PhD Thesis (Los Angeles, Calif.: Univ. of California, 2013)
274. Srinivasan G, Fetisov Y K *Ferroelectrics* **342** 65 (2006)
275. Fetisov Y K, Srinivasan G *Appl. Phys. Lett.* **88** 143503 (2006)
276. Fetisov Y K, Srinivasan G *Appl. Phys. Lett.* **87** 103502 (2005)
277. Fetisov Y K, Srinivasan G *Electron. Lett.* **41** 1066 (2005)
278. Sadovnikov A V et al. *Phys. Rev. Lett.* **120** 257203 (2018)
279. Sadovnikov A V et al. *JETP Lett.* **106** 465 (2017); *Pis'ma Zh. Eksp. Teor. Fiz.* **106** 445 (2017)
280. Zhai J et al. *Eur. Phys. J. B* **71** 383 (2009)
281. Zhai J et al. *J. Appl. Phys.* **100** 124509 (2006)
282. Zhuang X et al. *Appl. Phys. Lett.* **111** 163902 (2017)
283. Chua L *IEEE Trans. Circuit Theory* **18** 507 (1971)
284. Strukov D B et al. *Nature* **453** 80 (2008)
285. Maksymovych P et al. *Nano Lett.* **11** 1906 (2011)
286. Il'ina M V et al. *Carbon* **123** 514 (2017)
287. Shang D-S et al. *Chinese Phys. B* **24** 68402 (2015)
288. Jo S H et al. *Nano Lett.* **10** 1297 (2010)
289. Kalashnikova A M, Kimel' A V, Pisarev R V *Phys. Usp.* **58** 969 (2015); *Usp. Fiz. Nauk* **185** 1064 (2015)
290. Zvezdin A K, Davydova M D, Zvezdin K A *Phys. Usp.* **61** 1127 (2018); *Usp. Fiz. Nauk* **188** 1238 (2018)